October 2021

Dynamical System and Parameter Identification for Power Systems

Abdullah Abdulrahman Alassaf
University of South Florida

Dynamical System and Parameter Identification for Power Systems

by

Abdullah Abdulrahman Alassaf

A dissertation submitted in partial fulfillment
of the requirements for the degree of
Doctor of Philosophy
Department of Electrical Engineering
College of Engineering
University of South Florida

Major Professor: Lingling Fan, Ph.D.
Zhixin Miao, Ph.D.
Nasir Ghani, Ph.D.
Fangxing Li, Ph.D.
Qiong Zhang, Ph.D.

Date of Approval:
October 11, 2021

Keywords: Dynamic mode decomposition, synchronous generator, inverter, oscillation,
eigenvalues analysis

Dedication

To my parents, Watfa and Abdulrahman.

To my wife and daughter, Ruqaiyah and Elaf.

To my sisters and brothers.

Acknowledgments

I would like to express my deep gratitude to my advisor Dr. Lingling Fan. Her passion for knowledge and research has taught me to strive for solutions. I am very grateful for her guidance and dedication.

I would like to thank my doctoral committee, Dr. Zhixin Miao, Dr. Nasir Ghani, Dr. Fangxing Li, and Dr. Qiong Zhang for their encouragement and insightful comments.

I gratefully acknowledge the University of Hail for the scholarship that is organized by Saudi Arabian Cultural Mission (SACM).

I am thankful for the friendship and advice of current and former colleagues at the smart grid power system laboratory. In particular, I would like to thank Dr. Ibrahim Alsaleh, Dr. Anas Almunif, Dr. Ahmad Tazay, Dr. Sulaiman Almutairi, Dr. Minyue Ma, Dr. Yin Li, Dr. Yangkun Xu, Rabi Kar, Miao Zhang, Zhengyu Wang, Abdulhakim Alsaif, Abdullah Alburidy, Dr. Mohammed Alqahtani, Li Bao, and Ratik Mittal.

Special thanks go to my missing friend, Ayman Homoud Aldhamadi. I am honored to be one of his friends. May Allah forgive him and have mercy on him.

I can never thank my parents and grandparents enough for the support, love, and prayers. I am forever indebted to my mother, Watfa Alkhalid, and my father, Abdulrahman Alassaf. I am also thankful to my sisters and brothers for their encouragement and support. I greatly appreciate the kindness and support of my wife, Ruqaiyah Alsuwena. Her patience and care have been helping a lot during my studies. Finally, I am thankful to my daughter Elaf for bringing joy and happiness to my life.

Table of Contents

List of Tables

List of Figures

Abstract

The complexity of dynamical analysis has been growing to suffice the understanding and modeling of dynamical systems. Besides its nonlinearity and high-dimensionality, the dynamics of power systems contain uncertainty that complicates its analysis. Recently, dynamical modeling has been categorized into three types: white-box, black-box, and gray-box. White-box modeling has the accessibility of all system components. Black-box modeling has the observability of the system measurements without knowing the actual system. Gray-box modeling has the observability of the system measurements with the reachability to some of the system components. The scope of this dissertation focuses on black-box and gray-box models to achieve practical system and parameter identification of power system applications.

Dynamic Mode Decomposition (DMD) is a black-box method that has been proposed by the fluid community. It is a free-equation model identification technique and it has proven its practicality in various fields including brain modeling, fluid experiments, video separation, flows around a train, and financial trading strategies. Our work reviews the DMD algorithm and implements it for mode identification and signal reconstruction in three power system-related applications: RLC circuit dynamics, phasor measurement unit (PMU) measurements of an unknown system, and AC voltage waveform polluted by harmonics. In the first two applications, we compare DMD with Eigensystem Realization Algorithm (ERA) and present that the two methods have the same accuracy level. The last application shows that DMD can also work as fast Fourier transformation (FFT), which can identify harmonics and their magnitudes in the analyzed system.

The standard DMD is unable to identify real-world measurement data captured by phasor measurement units (PMUs) because they are noisy. In our research, we enhance DMD performance by data stacking that increases the rank of the data matrix. Correspondingly,

DMD accurately identifies the system eigenvalues and eigenvectors. The eigensystem components reveal the details of the dynamics and reconstruct the signals in the time-evolving format. While data stacking raises the computation cost, we further implement a randomization technique for DMD to radically reduce the size of the data matrix. The randomized DMD (rDMD) has high accuracy and efficiency. Our work shows that the identified mode shapes (eigenvectors) of the DMD/rDMD can recognize the oscillation mode type whether it is local or interarea. PMU data from three real-world oscillation events are used for demonstration. Also, we compare both DMD and rDMD with the classical identification methods including Prony, Matrix Pencil, and Eigensystem Realization Algorithm.

The second part of this dissertation focuses on gray-box dynamical modeling for parameter identification. The two classical parameter identification methods are the prediction error method (PEM) and the similarity matrix technique. These methods are nonlinear and require a good initial guess of parameters that must be in the domain of convergence. Recently, two new methods have been developed by the system identification community. These methods start from the two conventional methods, make computing improvement by taking into consideration the low-rank characteristic of data, and formulate the estimation problems as rank-constraint optimization problems. Furthermore, the rank-constraint optimization problems are converted to difference of convex programming (DCP) problems and solved by convex iteration. The new convexification technique leads to more accurate parameter estimation. Our work presents the four methods and implements the problem formulations and solving algorithms for synchronous generator and inverter-based resource (IBR) dynamic model parameter estimation.

Chapter 1: Introduction

1.1 Background

Power system oscillation is an electromechanical behavior that exists in any interconnection system that contains more than a synchronous generator. In 2018, the total number of US electrical energy sources reached 22,118 units [1]. With this considerably large number of electric units, oscillations must be taken under consideration. Even with regular operation, oscillations are found in the electric grid due to mundane actions such as load change. Generally, oscillations grow, sustain, or decay, as shown in Fig. 1.1. Growing oscillations could result in catastrophic outcomes: instability, vulnerability, and damage. Oscillations are categorized into System and Forced [2]. The system oscillations tend to have low magnitudes; they are broken down into local, intraplant, inter-area, and torsional. The Forced oscillations are initiated by external sources like equipment failures, control interaction, or abnormal operation.

With the help of PMUs, different types of oscillation have been observed across the U.S. grid. While the system oscillations can be caused by several event types, they may lead to catastrophic events. One of the major oscillation events in the U.S. electrical system is WSCC August 10, 1996 disturbance. Sequence actions initiated the event:

- Because of a fault, a 230 kV transmission line and a generator unit were removed from the system.

- 13 of the McNary hydro units increased their reactive power output by 14 MVAr.

- Due to some error in the operation, an unbalance relay tripped all 13 units.
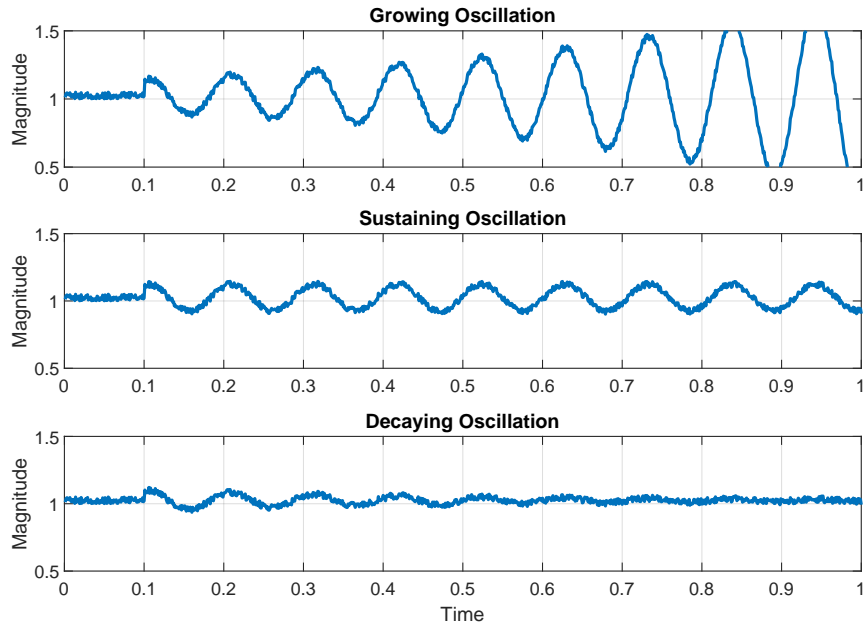
Figure 1.1: Oscillation types. The top plot shows a growing oscillation, the middle plot shows a sustaining oscillation, and the bottom plot shows a decaying oscillation.

- After disconnecting the McNary units, a poorly damped interarea oscillation initiated in the system. The oscillations grew to about 1,000 MW and 60 kV peak-to-peak.

- The system voltage collapsed. The system was separated into four electrical islands.

- 28,000 MW of the system load was dropped; 7,500,000 customers were affected by this event.

By analyzing this event, the main reason behind collapsing the system is the oscillations, which were initiated by the cascaded protection actions. Reference [3] gives a detailed analysis of this event, and it conducts oscillation analysis that shows the oscillation frequency is 0.712 Hz with damping of -7.62%.

Oscillation analysis mainly focuses on oscillations detection to determine their source and mitigate them. The oscillation is characterized by its frequency, damping ratio, mode shape, and participation factor. While mode frequency describes the oscillating degree, the damping ratio indicates whether the oscillation is growing or decaying. Mode shape is mathematically the eigenvector associated with the oscillation mode: it shows the system

state direction for the mode. The participation factor specifies the effect degree between the states and the analyzed mode. These characteristics reveal rich aspects of the dynamical system; they can be carried out by either model-based or data-driven approaches [4]. The latter is more practical for analyzing large-scale systems.

The government incentives and technology development have accelerated the growth of renewables. Currently, the most effective players of renewables are wind-turbine generators (WTGs) and photovoltaic (PV) systems. A single wind-turbine unit can generate up to 4 MW, and a single rooftop panel can generate up to several kilowatts. The exploitation of the wind system is the largest due to its efficiency and practicality. In 2019, the generated power from wind power plants (WPPs) reached 300 billion kWh in the US [1]. Besides their intermittence, WPPs significantly reduce the system inertia that damps out the normal and abnormal oscillations. Integrating renewables with the existing components necessitate redesigning the system control structure.

During operation, equipment manufacturer parameters vary based on the system loading level. In power systems, parameter variation is also caused by different factors such as magnetic saturation, overloading, temperature, device aging, disturbances, and faults.

Identifying the system through measurements data can avoid not only operation interruption, but also complicated testing. Parameter estimation uses the knowledge of the known parameters to identify the unknown ones. In the literature, it is referred to as gray-box identification.

1.2 Problem Statement

Dynamical system analysis is mandatory to enrich system physical understanding that leads to advanced and practical implementations such as estimation, control, design, optimization, and future state prediction. Recently, dynamical system analysis is categorized based on our prior knowledge of the system. The dynamical analysis modeling is categorized into three types: white-box, black-box, and gray-box.

1.2.1   White-Box Modeling

This type of modeling is completely based on physical relationships. It assumes that all the analyzed system details can be reached or calculated. generally, researchers and engineers strive to bring engineering applications to this category for two reasons. First, it is desired to mathematically interpret and describe the system behavior so that we are enabled to handle and predict its response. In addition, we will be able to figure out how any change in the system impacts its behavior. Second, this category improves the engineering sense in a way that helps to enhance its performance.

Engineering applications are constructed in accordance with white-box modeling. For example, if we have a simple RLC circuit, and we know the value of each component as well as the supply voltage source, we can simply not only calculate the circuit current but also compute the power each component consumes. Another example, for a given relatively small power system, it is possible to implement the power system analysis such as load flow, optimal power flow, continuation power flow, or fault analysis.

State-space model expresses the system's dynamical behavior. For a nth-order system with m input and p outputs, the continuous-time state-space model is expressed as follows.

$$
\begin{aligned}
x(t) &= A_c x(t) + B_c u(t), \\
y(t) &= C_c x(t) + D_c u(t),
\end{aligned}
\tag{1.1}
$$

where $A_c \in \mathbb{R}^{n \times n}$, $B_c \in \mathbb{R}^{n \times m}$, $C_c \in \mathbb{R}^{p \times n}$, and $D_c \in \mathbb{R}^{p \times m}$ are the dynamical system matrix, the input matrix, the output matrix, and the feedthrough matrix, respectively. The system state variable is x, the system input is u, and the system observable component is y.

Many engineering applications adopt discrete-time state-space because it is more practical for several reasons such as discrete measurement and efficient computation. The discrete-time state space is as follows. With all the great advantages that can be achieved from white-box modeling, it can be obstructed because of the unknown dynamics, uncertainty, nonlinearity, and high-dimensionality.

$$x_{k+1} = A_d x_k + B_d u_k,$$

$$(1.2)$$

$$y_k = C_d x_k + D_d u_k,$$

where k is the sample number with respect to the time sampling period Δt. The state-space modeling is shown in Fig. 1.2.
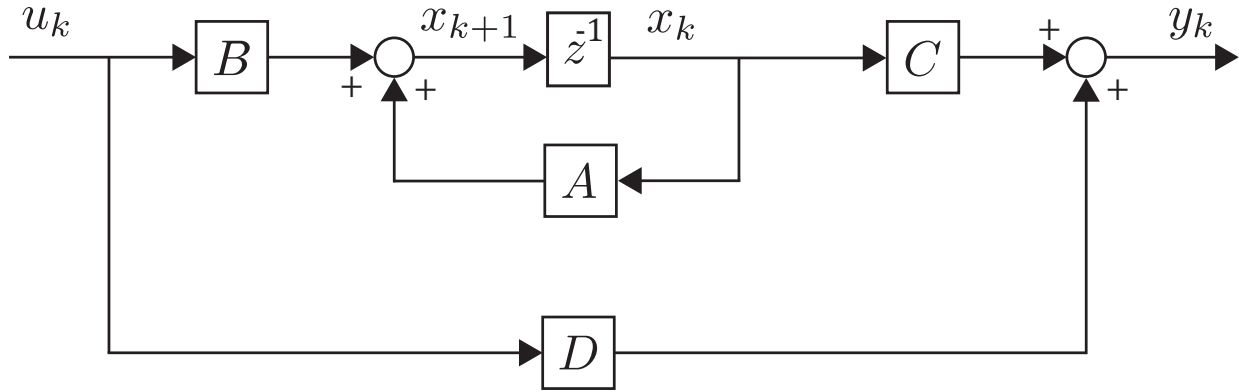
Figure 1.2: The state-space modeling.

1.2.2 Black-Box Modeling

In the literature, this category is also called response modeling. Black-box algorithms aim to reveal the system's characteristics from only the input and output measurements. Without prior knowledge of the system, the black-box modeling describes the system behavior, as shown in Fig. 1.3.

Figure 1.3: Black-box modeling scheme. It takes only the system input and output measurement to identify the system characteristics.

As dynamical systems are conveniently linearized and approached with state-space form, the black-box model seeks to identify the state matrix A that expresses the system response, as illustrated in Fig. 1.4.
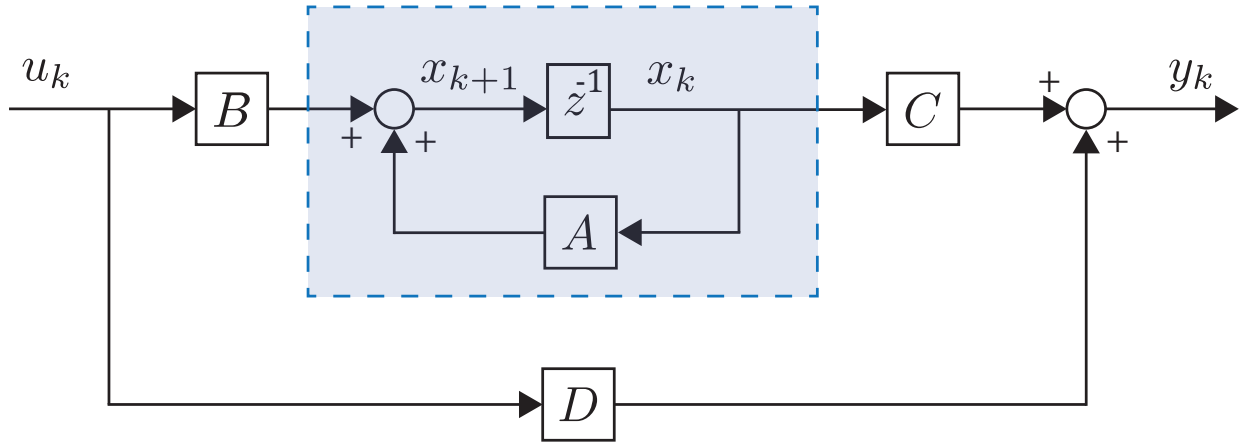
Figure 1.4: General implementation of black-box modeling on state-space form.

Owing to its practicality, black-box modeling has served in diverse engineering applications for decades. It has been developing for decades and it can be approached with many mature algorithms. Some of the algorithms take the input and output measurements, and some take only the output measurement with the assumption that the system input is an impulse or step response. While the output-based algorithms take into account only the state matrix A, the input-output-based algorithms consider all the state space components: A, B, C, and D. In general, all the black-box algorithms identify the state-space matrices up to a similarity matrix. Although the identified system has the characteristics of the original system, the similarity matrix hides the actual system parameters.

1.2.3   Gray-Box Modeling

Gray-box modeling is a combination of the white-box (Physical modeling) and the black-box (Response modeling). The concept of gray-box modeling is to utilize the input-output

measurement with the known parameters to identify the unknown parameters; its scheme is shown in Fig. 1.5.
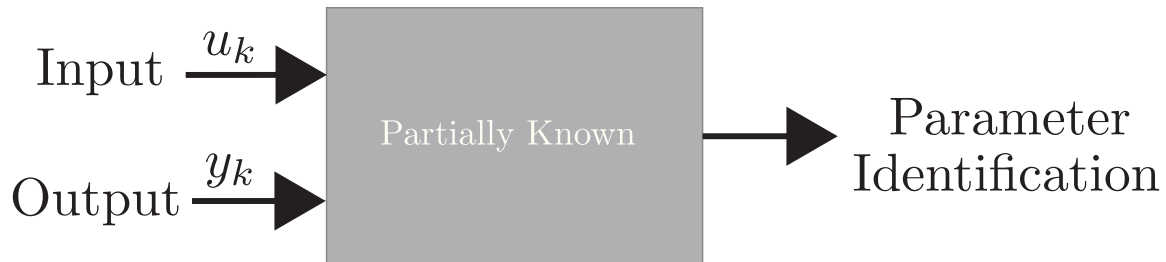
Figure 1.5: Gray-box scheme. It consolidates the known system parameters with the system input and output measurement to identify the unknown parameters.

The gray-box model can be reflected in state-space form as shown in Fig. 1.6. It seeks to identify the actual dynamical system matrix A, the input matrix B, the output matrix C, and the feedthrough matrix D.
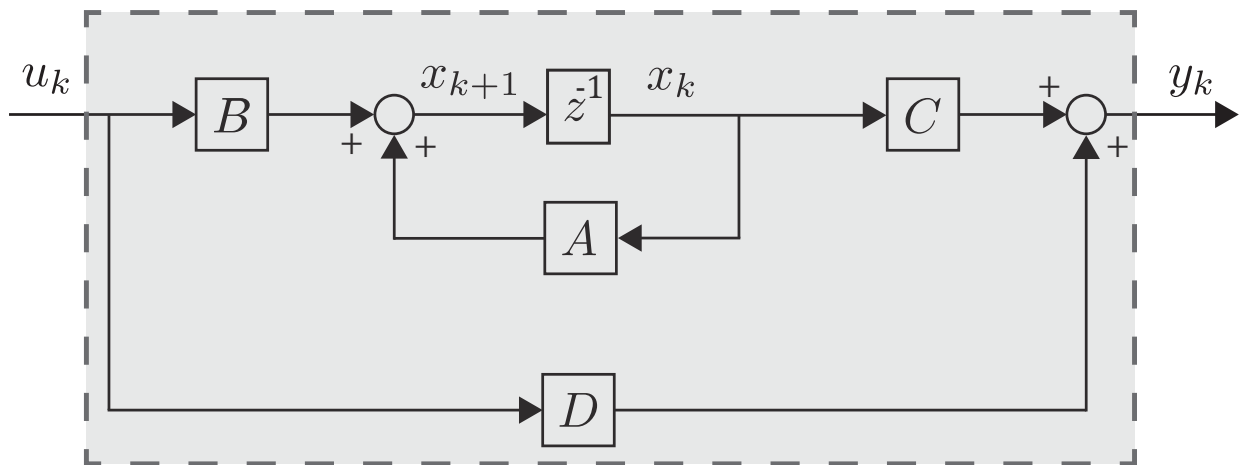
Figure 1.6: The implementation of gray-box modeling on state-space form.

Parameter identification plays a critical role in understanding as well as designing dynamic systems. In real-world application even if the system structure is known under steady-state operation, the whole system or part of it changes during abnormal conditions. For

example, generator parameters change under transient and sub-transient conditions. We stand in need to identify the system under online operation so that the service will not be interrupted. Since it is impractical or impossible to manually measure each system component, we rely on our knowledge of the system structure and utilize the input/output to identify missing parts. Gray-box methods can lead to precious information of a system that is partially known. The main challenges of gray-box implementations:

- It needs prior knowledge of the system.

- It is less reliable due to nonlinearity and nonconvexity.

- It is not applicable to all systems because not all systems are identifiable.

1.3 Research Objectives and Achievements

This dissertation breaks down into the following parts:

1.3.1 Dynamic Mode Decomposition in Power Systems

The importance of describing a system through its measurements encourages researchers to develop system identification algorithms. Dynamic Mode Decomposition is one of the newest algorithms that has been proposed by the fluid community. It has served in different applications such as brain modeling, video separation, flows around a high-speed train, and financial trading strategies. We explore the DMD's ability in power system applications. DMD is applied to identify the dynamics matrix for an RLC circuit using measurement data and identify a signal's frequency components and magnitudes. The latter application achieves the same function as fast Fourier transformation (FFT). DMD and ERA are compared to show that they achieve similar levels of accuracy.

1.3.2 Randomized DMD for Oscillations

Real-world inter-area oscillation events are approached with only sturdy system identification algorithms. Besides their large-scale difficulty, the real-world PMU measurements contain noise that complicates the analysis. The standard DMD algorithm is unable to deal with real-world inter-area oscillation events for that reason. We change the standard data input and apply the data stacking technique. This increases the rank of the data input, thus enabling the user to absorb more information from the data. The main drawback of data stacking is that it adds a computational burden to the process of solving the problem. Employing randomized linear algebra techniques considerably reduces the computation cost. We implement modified DMD and randomized DMD on three real-world oscillation events that occurred in ISO New England, a North-East part of the U.S. Eastern Interconnection. The proposed method has been compared with the prominent methods: Prony, Matrix Pencil, and ERA. Besides the accuracy and efficiency, our approach provides the user the ability to differentiate whether the oscillation is local or inter-area. Correspondingly, the grid operator can easily locate the event source and take the proper action.

1.3.3 Gray-Box Modeling for Generators and Inverters

To govern a system, all the system parameters must be known. The parameters of dynamical systems likely change with time or due to disturbances. The existing parameter identification methods are nonlinear and exposed to settle in a local point, which is unrelated to the actual system parameters. Thanks to convexification improvement, the control and system identification communities have developed new convex methods that have a higher chance of reaching the global solution point, which reflects the actual system parameters. We employ and formulate two of the powerful convexified methods to identify a synchronous generator and a reduced-order wind system connected to a weak grid. Those convex identification methods take the advantage of the rank constraint to be solved efficiently with the

difference of convex programming. We compare and discuss the two convexified methods with two classical nonlinear methods to examine their performance.

1.4 List of Publication

- Journal Papers

1. Alassaf, Abdullah, and Lingling Fan. "Randomized dynamic mode decomposition for oscillation modal analysis." IEEE Transactions on Power Systems 36.2 (2020): 1399-1408.

2. Alassaf, Abdullah, and Lingling Fan. "Review of Dynamic Model Parameter Estimation Methods and Two Application Examples," submitted to International Transactions on Electrical Energy Systems.

- Conference Papers

1. Alassaf, Abdullah, and Lingling Fan. "Economic dispatch with heavy loading and maximum loading identification using convex relaxation of AC OPF." 2017 North American Power Symposium (NAPS). IEEE, 2017.

2. Alassaf, Abdullah, and Lingling Fan. "Bilevel programming-based unit commitment for locational marginal price computation." 2018 North American Power Symposium (NAPS). IEEE, 2018.

3. Alassaf, Abdullah, Lingling Fan, and Ibrahim Alsaleh. "Day-Ahead Distribution Market Analysis Via Convex Bilevel Programming." 2019 North American Power Symposium (NAPS). IEEE, 2019.

4. Alassaf, Abdullah, and Lingling Fan. "Dynamic Mode Decomposition in Various Power System Applications." 2019 North American Power Symposium (NAPS). IEEE, 2019.

1.5 Outline of the Dissertation

The dissertation is organized as follows:

Chapter 2 presents the dynamic mode decomposition background and data-stacking technique. The DMD algorithm is implemented in power system applications: RLC circuit, PMU measurements, and distorted signal. In these applications, we compare DMD with ERA and FFT.

Chapter 3 provides a data randomization technique based on linear algebra. Then, the randomization technique is applied to the DMD algorithm to have Randomized Dynamic Mode Decomposition (rDMD). Afterward, the DMD and rDMD are implemented on real-world event data analysis. This chapter also compares DMD and rDMD with the existing methods that are Prony, Matrix Pencil, and Eigensystem Realization Algorithm.

Chapter 4 overviews the gray-box model identification problem formulation and presents two classical methods: Prediction Error Method and Similarity Matrix Technique. Then, it introduces the convexification of the similarity matrix technique and the convex Ho-Kalman method. The four identification techniques are applied to two case studies: a second-order dynamic model and a reduced-order grid-integrated IBR model.

Chapter 5 concludes our work and plans future work.

Chapter 2: Dynamic Mode Decomposition in Power System Applications

2.1 Introduction

The oscillation modes injected to the power grid can be identified by several black-box (data-driven) methods: Prony [5], [4], Matrix Pencil [6], [7], Eigensystem Realization Algorithm (ERA) [8], Koopman Analysis [9], and Variable Projection Method [10].

In the 2012 IEEE PES taskforce report on electromechanical mode identification [11], three methods for ringdown signals: Prony, Matrix Pencil, and ERA methods, were presented. Reference [12] further compares the three methods on their similarity, including data matrix formulation and noise handling relying on singular value decomposition (SVD). Case studies on two real-world events taken from [13] show that ERA has the best performance in eigenvalue identification accuracy.

A more recent method called dynamic mode decomposition (DMD) has been proposed and applied in fluid community [14] in 2010. The DMD algorithm has been used in diverse applications such as brain modeling, fluid experiments, foreground/background video separation, flows around a high-speed train, and financial trading strategies [15]. Reference [16] applies DMD under the consideration of setting the given data in pairs of n-dimensional vectors, rather than the time-sequential series. In the same reference, the authors compare the DMD with two other system identification techniques that are ERA and linear inverse modeling (LIM).

DMD is applied in power systems for oscillation analysis in [17]. The authors show that DMD is more efficient than both Koopman and Prony in identifying dynamical modes and their spatial and temporal characteristics. Reference [18] visualizes the identified modes to approach more intuitive dynamical attributes. In decentralized WAMS structure, [19]

successfully circumvents high-dimensional data processing using DMD Compressed Sensing that selects the most observable PMUs. The DMD extracts distortion harmonic components of microgrids [20]. Reference [21] enhances the performance of the extended DMD under noisy measurements.

For practical interest, besides eigenvalue identification, the distinction of the oscillation mode as local or inter-area is desired. If the definition of the state variables is known, mode shape or eigenvector can lead to more information regarding who is contributing to the oscillation.

Compared to several other methods that rely on Hankel matrices, e.g., Prony analysis, Matrix Pencil, and ERA, DMD has a unique advantage: state variables have a clear physical definition. Thus the mode shape information from the system matrix A leads to the physical interpretation of how measurement influences an oscillation mode. Matrix Pencil and Prony analysis do not lead to system matrix A. Though ERA leads to a state matrix, the state variables are unknown.

DMD decomposes high-dimensional data into spatial and temporal structures. Essentially, DMD carries out eigendecomposition for a data matrix. Hence, a data matrix can be factorized into two components: spatial and temporal. The dynamic system model can be found by keeping the dominant spatiotemporal structures which are identified using dominant singular values. This feature also helps to obtain a reduced-order model which keeps only dominant eigenvalues. The future state may be predicted using the identified eigenvalues and initial states.

This chapter provides a concise review of the DMD algorithm and further demonstrates DMD implementation in power system applications[1]. The first case study applies DMD on a series RLC circuit to identify its modes using sample measurements of the capacitor voltage and the inductor current. Further, random distortions are injected into the voltage and current measurements so that we examine the DMD capability noisy measurement. In

---

[1]This chapter was published in IEEE North American Power Symposium [22]. Permission is included in Appendix A.

the second case study, we test the DMD algorithm with PMU power measurements. In these two case studies, the DMD is compared with ERA. The third case study implements DMD with voltage measurements that contain undesired real-world harmonic components. DMD can accurately identify the model and decompose all the existing components.

2.2 DMD General Concept

The general dynamical continuous-time structure

$$\frac{d\mathbf{x}}{dt} = \mathbf{f}(\mathbf{x}, t; \mu), \tag{2.1}$$

where $\mathbf{f}(\cdot)$ is the dynamical continuous-time function. $\mathbf{x}$ is the system state vector, $\mathbf{x} \in \mathbb{R}^n$, at time t, whereas μ denotes the system parameters. In free-equation modeling, the measurements of the unknown system take the place of the dynamical function $\mathbf{f}(\cdot)$. In practice, the measurements are collected in discrete-time; thus, we initially conduct the DMD in discrete-time dynamics

$$\mathbf{x}_{k+1} = \mathbf{F}\left(\mathbf{x}_k\right), \tag{2.2}$$

where $\mathbf{F}(\cdot)$ expresses the equally-spaced discrete form. The discrete state is $\mathbf{x}_k = \mathbf{x}(k\Delta t)$ for $k = 1, 2, \ldots, m$. Δt is the system sampling period, and m is the total number of measurements. In linear or linearized dynamic system, the dynamics matrix, $\mathbf{A} \in \mathbb{R}^{n \times n}$, maps the snapshot $\mathbf{x}_k$ to the subsequent snapshot $\mathbf{x}_{k+1}$ as

$$\mathbf{x}_{k+1} = \mathbf{A}\mathbf{x}_k. \tag{2.3}$$

Applying eigen-decomposition to matrix $\mathbf{A} = \mathbf{\Phi}\mathbf{\Lambda}\mathbf{\Phi}^{-1}$ leads to

$$\mathbf{x}_{k+1} = \mathbf{\Phi}\mathbf{\Lambda}\mathbf{\Phi}^{-1}\mathbf{x}_k = \mathbf{\Phi}\mathbf{\Lambda^2}\mathbf{\Phi}^{-1}\mathbf{x}_{k-1} = \cdots = \mathbf{\Phi}\mathbf{\Lambda}^k \underbrace{\mathbf{\Phi}^{-1}\mathbf{x}_1}_{\mathbf{b}}, \tag{2.4}$$

where $\mathbf{b} \in \mathbb{C}^{n \times 1}$, $\mathbf{\Phi} \in \mathbb{C}^{n \times n}$ is the right eigenvector matrix of $\mathbf{A}$, and $\mathbf{\Lambda}$ is a diagonal matrix with elements as $\lambda_i, i = 1, \cdots, n$. The DMD enables spatio-temporal decomposition of high-dimensional data from which we can analyze how the system modes evolve in time. The decomposition structure is defined:

$$\mathbf{x}_{k+1} = \sum_{j=1}^{r} \phi_j \lambda_j^k b_j = \mathbf{\Phi} \mathbf{\Lambda}^k \mathbf{b}, \tag{2.5}$$

where the columns of $\mathbf{\Phi}$ are the DMD modes, the diagonal entries of $\mathbf{\Lambda}$ are the discrete-eigenvalues, λ_k, and $\mathbf{b}$ is the coordinates of $\mathbf{x}(0)$ in the eigenvetor basis. All the measurement snapshots can be expressed using DMD components as follows

$$\mathbf{X} = \mathbf{\Phi} \begin{bmatrix} \mathbf{b} & \Lambda \mathbf{b} & \cdots & \Lambda^m \mathbf{b} \end{bmatrix}, \tag{2.6}$$

which can be simplified as

$$\mathbf{X} = \begin{bmatrix} | & | & \\ \phi_1 & \phi_2 & \cdots \\ | & | & \end{bmatrix} \mathrm{diag}(\mathbf{b}) \begin{bmatrix} 1 & \lambda_1 & \cdots & \lambda_1^m \\ 1 & \lambda_2 & \cdots & \lambda_2^m \\ \vdots & \vdots & \ddots & \vdots \end{bmatrix}. \tag{2.7}$$

The time-domain expression of $\mathbf{x}(t)$ can be constructed after identifying the eigenvalues and eigenvectors of $\mathbf{A}$

$$\mathbf{x}(t) = \sum_{k=1}^{n} \phi_k \exp\left(\omega_k t\right) b_k = \mathbf{\Phi} \exp(\mathbf{\Omega} t) \mathbf{b}, \tag{2.8}$$

where $\mathbf{\Omega}$ is a diagonal matrix that contains the continuous-eigenvalues, ω_k. The relationship between the discrete and continuous eigenvalue is $\omega_k = \ln\left(\lambda_k\right) / \Delta t$. These components, which reflect the system dynamic behavior, are identified from the system measurements with the help of DMD.

15

As DMD input, the collected snapshots of the unknown system are gathered in two sequential overlapping sets that one of them is time-shifted, as follows

$$\mathbf{X}_1^{m-1} = \begin{bmatrix} | & | & & | \\ \mathbf{x}_1 & \mathbf{x}_2 & \cdots & \mathbf{x}_{m-1} \\ | & | & & | \end{bmatrix}, \tag{2.9a}$$

$$\mathbf{X}_2^{m} = \begin{bmatrix} | & | & & | \\ \mathbf{x}_2 & \mathbf{x}_3 & \cdots & \mathbf{x}_{m} \\ | & | & & | \end{bmatrix}, \tag{2.9b}$$

where $\mathbf{X}_1^{m-1}$, $\mathbf{X}_2^m \in n \times (m-1)$. The subscript and superscript refer to the first and last measurement snapshots in set, respectively. The logic behind this is to generate Krylov subspace; therefore, substituting (2.3) in (2.9) yields

$$\mathbf{X}_1^{m-1} \approx \begin{bmatrix} | & | & & | \\ \mathbf{x}_1 & \mathbf{A}\mathbf{x}_1 & \cdots & \mathbf{A}^{m-1}\mathbf{x}_1 \\ | & | & & | \end{bmatrix}, \tag{2.10a}$$

$$\mathbf{X}_2^{m} \approx \begin{bmatrix} | & | & & | \\ \mathbf{A}\mathbf{x}_1 & \mathbf{A}^2\mathbf{x}_1 & \cdots & \mathbf{A}^{m}\mathbf{x}_1 \\ | & | & & | \end{bmatrix}. \tag{2.10b}$$

Consequently, the best-fit dynamics matrix, $\mathbf{A}$, is derived as

$$\mathbf{A} = \arg\min_{\mathbf{A}} \left\| \mathbf{X}_2^m - \mathbf{A}\mathbf{X}_1^{m-1} \right\|_F = \mathbf{X}_2^m (\mathbf{X}_1^{m-1})^\dagger, \tag{2.11}$$

where $\| \cdot \|_F$ is the Frobenius norm, and the superscript $\dagger$ notates Moore-Penrose pseudo inverse that is mathematically evaluated as $\mathbf{X}^\dagger = (\mathbf{X}^T\mathbf{X})^{-1}\mathbf{X}^T$, where the superscript T refers to the transpose. To avoid dealing with inverse of a large-size matrix, Singular Value Decomposition (SVD) is adopted for $\mathbf{X}_1^{m-1}$. In addition, a rank r will be chosen for rank

reduction. Hence,

$$\mathbf{X}_1^{m-1} \approx \mathbf{U}\mathbf{\Sigma}\mathbf{V}^*, \tag{2.12}$$

where $\mathbf{U} \in \mathbb{R}^{n \times r}, \mathbf{\Sigma} \in \mathbb{R}^{r \times r}$, and $\mathbf{V} \in \mathbb{R}^{(m-1) \times r}$, and $*$ denotes the complex conjugate transpose. $\mathbf{U}$ and $\mathbf{V}$ are unitary matrices, they satisfy $\mathbf{U}^*\mathbf{U} = \mathbf{I}$ and $\mathbf{V}^*\mathbf{V} = \mathbf{I}$.

It can be found from (2.12) that the pseudo-inverse of $\mathbf{X}_1^{m-1}$ can be expressed as:

$$(\mathbf{X}_1^{m-1})^\dagger \approx \mathbf{V}\mathbf{\Sigma}^{-1}\mathbf{U}^*. \tag{2.13}$$

Hence, according to (2.11), $\mathbf{A}$ can be expressed as follows.

$$\mathbf{A} = \mathbf{X}_2^m \mathbf{V}\mathbf{\Sigma}^{-1}\mathbf{U}^*. \tag{2.14}$$

A low-dimensional dynamics matrix $\tilde{\mathbf{A}}$ is realized by projecting $\mathbf{A}$ onto $\mathbf{U}$ basis:

$$\tilde{\mathbf{A}} = \mathbf{U}^*\mathbf{A}\mathbf{U} = \mathbf{U}^*\mathbf{X}_2^m \mathbf{V}\mathbf{\Sigma}^{-1}, \tag{2.15}$$

where $\tilde{\mathbf{A}} \in \mathbb{R}^{r \times r}$. The low-rank dynamical model becomes:

$$\tilde{\mathbf{x}}_{k+1} = \tilde{\mathbf{A}}\tilde{\mathbf{x}}_k, \tag{2.16}$$

where $\tilde{\mathbf{x}} = \mathbf{U}^*\mathbf{x}$ and $\tilde{\mathbf{x}} \in \mathbb{R}^r$.

The full-rank state vector can be recovered by $\mathbf{x}_k = \mathbf{U}\tilde{\mathbf{x}}_k$. Next, the eigendecomposition of the low-dimensional dynamics matrix $\tilde{\mathbf{A}}$ is carried out.

$$\tilde{\mathbf{A}}\mathbf{W} = \mathbf{W}\mathbf{\Lambda}, \tag{2.17}$$

where $\mathbf{\Lambda} \in \mathbb{C}^{r \times r}$, and $\mathbf{W} \in \mathbb{C}^{r \times r}$. The diagonal entries of $\mathbf{\Lambda}$ are the eigenvalues, and the columns of $\mathbf{W}$ are the eigenvectors. While $\mathbf{\Lambda}$ is associated to both $\tilde{\mathbf{A}}$ and $\mathbf{A}$, $\mathbf{W}$ is associated

Algorithm 2.1 Dynamic Mode Decomposition

Input: $\mathbf{X} = [\,\mathbf{x_1}\,\mathbf{x_2}\,\mathbf{x_3} \ldots \mathbf{x_m}\,] \in \mathbb{R}^{n \times m}$.
Output: $\mathbf{\Phi} \in \mathbb{C}^{n \times r}$, $\mathbf{\Lambda} \in \mathbb{C}^{r \times r}$, $\mathbf{W} \in \mathbb{C}^{r \times r}$, $\mathbf{b} \in \mathbb{C}^{r \times 1}$.
 1: $\mathbf{X_1} \leftarrow [\,\mathbf{x_1}\,\mathbf{x_2}\,\mathbf{x_3} \ldots \mathbf{x_{m-1}}]$, $\mathbf{X_1} \in \mathbb{R}^{n \times (m-1)}$,
    $\mathbf{X_2} \leftarrow [\,\mathbf{x_2}\,\mathbf{x_3}\,\mathbf{x_4} \ldots \mathbf{x_m}]$, $\mathbf{X_2} \in \mathbb{R}^{n \times (m-1)}$.
 2: $[\mathbf{U}, \mathbf{\Sigma}, \mathbf{V}] = \texttt{svd}\,(\,\mathbf{X_1})$,
    $\mathbf{U} \in \mathbb{R}^{n \times r}, \mathbf{\Sigma} \in \mathbb{R}^{r \times r}, \mathbf{V} \in \mathbb{R}^{(m-1) \times r}$.
 3: $\mathbf{\tilde{A}} \leftarrow \mathbf{U}^* \mathbf{X_2} \mathbf{V} \mathbf{\Sigma}^{-1}$, $\mathbf{\tilde{A}} \in \mathbb{R}^{r \times r}$
 4: $[\mathbf{W}, \mathbf{\Lambda}] = \texttt{eig}(\mathbf{\tilde{A}})$.
 5: $\mathbf{\Phi} \leftarrow \mathbf{UW}$.
 6: $\mathbf{b} \leftarrow \mathbf{\Phi}^{\dagger} \mathbf{x_1}$.

---

to only $\mathbf{\tilde{A}}$. The eigenvectors of the high-dimensional dynamics matrix $\mathbf{A}$ are recovered as follows

$$\mathbf{\Phi} = \mathbf{UW}, \tag{2.18}$$

where $\mathbf{\Phi} \in \mathbb{C}^{n \times r}$. Finally, $\mathbf{b}$, is computed as

$$\mathbf{b} = \mathbf{\Phi}^{\dagger} \mathbf{x_1}, \tag{2.19}$$

where $\mathbf{b} \in \mathbb{C}^{r \times 1}$. The standard DMD procedure is summarized in Algorithm 2.1.

2.2.1 Data Stacking

Suppose that there is one measurement channel. The data matrix $\mathbf{X}$ will be a row vector, which certainly makes estimation difficult. To construct a data matrix, the stacking technique is used to obtain a data matrix $\mathbf{X}$ with a higher row dimension. Augmenting the data in shift-stacking and time-delay matrix ensures a more accurate solution [15]. Moreover, data stacking increases the dimension of the measurement matrix that helps capture more information from the data. The general data multi-channel form is set as follows.

$$\mathbf{X_{aug}} = \begin{bmatrix} \mathbf{X}_1^{m-(s-1)} \\ \mathbf{X}_2^{m-(s-2)} \\ \vdots \\ \mathbf{X}_s^m \end{bmatrix}$$

$$= \begin{bmatrix} \mathbf{x}_1 & \mathbf{x}_2 & \cdots & \mathbf{x}_{m-(s-1)} \\ \mathbf{x}_2 & \mathbf{x}_3 & \cdots & \mathbf{x}_{m-(s-2)} \\ \vdots & \vdots & \ddots & \vdots \\ \mathbf{x}_s & \mathbf{x}_{s+1} & \cdots & \mathbf{x}_m \end{bmatrix}$$

$$(2.20)$$

where $\mathbf{X_{aug}} \in \mathbb{R}^{s \cdot n \times (m-s+1)}$, and s is the stacking number. The DMD algorithm splits the augmented data into two overlapping sets:

$$\mathbf{X_{aug,1}} = \mathbf{X_{aug}}(:, 1 : m - s) \tag{2.21a}$$

$$\mathbf{X_{aug,2}} = \mathbf{X_{aug}}(:, 2 : m - s + 1) \tag{2.21b}$$

where $\mathbf{X_{aug,1}}, \mathbf{X_{aug,2}} \in \mathbb{R}^{s \cdot n \times (m-s)}$. It can be seen that

$$\mathbf{X_{aug,2}} = \mathrm{diag}([\mathbf{A}, \cdots, \mathbf{A}])\mathbf{X_{aug,1}}.$$

With the two new data matrices, the same DMD procedure can be carried out for modal analysis.

2.3 The DMD Applications in Power Systems

2.3.1 RLC Circuit

2.3.1.1 RLC Base-Case Measurements

In this case study, the DMD is implemented on a series RLC circuit that is shown in Fig. 2.1. It carries out the capacitor voltage and the inductor current measurement samples, as a result, the circuit model is identified, and the future states are predicted. The circuit parameters: V= 1 volt, Δt= 0.001 s, R= 1 Ω, L= 0.01 H, and C= 0.001 μ. The dynamics matrix, $\mathbf{A}$, is defined as follows

$$\mathbf{A} = \begin{bmatrix} \frac{-R}{L} & \frac{-1}{L} \\ \frac{1}{C} & 0 \end{bmatrix} = \begin{bmatrix} -100 & -100 \\ 1000 & 0 \end{bmatrix}.$$

Since the RLC circuit is a second-order system, it has two eigenvalues, $\lambda_{1,2}$, that are $-50.00 \pm j312.25$. Initially, the problem is solved through MATLAB function ode45 [23]. The RLC solution for 0.1 s, taking into account the sampling rate of 0.001 s, consists of 100 signal points. Only the first 20 points of the solution are employed as DMD input. The measurement time shift, s, is chosen to be 10. The size of both $\mathbf{X_{aug,1}}$ and $\mathbf{X_{aug,2}}$ is (20×10). It should be noted that the rows of the data matrices are 20, twice s, bearing in mind that the DMD input is comprised of two signals. Even though $\mathbf{X_{aug,1}}$ rank is 10, the rank-reduction is primarily based on the effective singular values, from the diagonal matrix Σ. This case has three powerful singular values that have most of the data information. The rest of the ineffective singular value can be disregarded. The normalized singular values are plotted in Fig. 2.2. Therefore, the DMD rank, r, is 3. Consequently, the rank-reduction of this case helps to circumvent 70 % of unnecessary computation.

The DMD solution is compared with the ERA method as well as the original model. The model identification is shown in Fig. 2.3, whereas the eigenvalues are plotted in Fig. 2.4. It can be seen that both methods exactly match the original system.
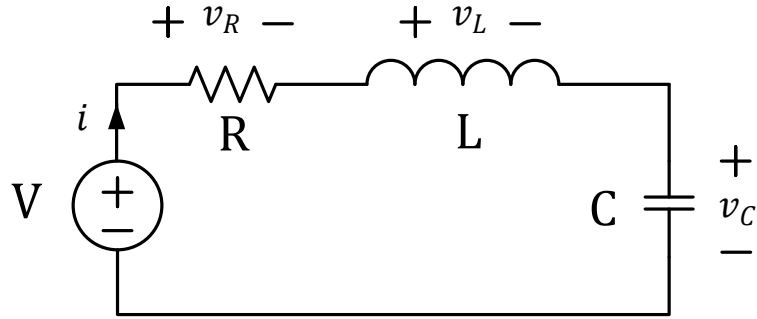
Figure 2.1: Series RLC circuit.
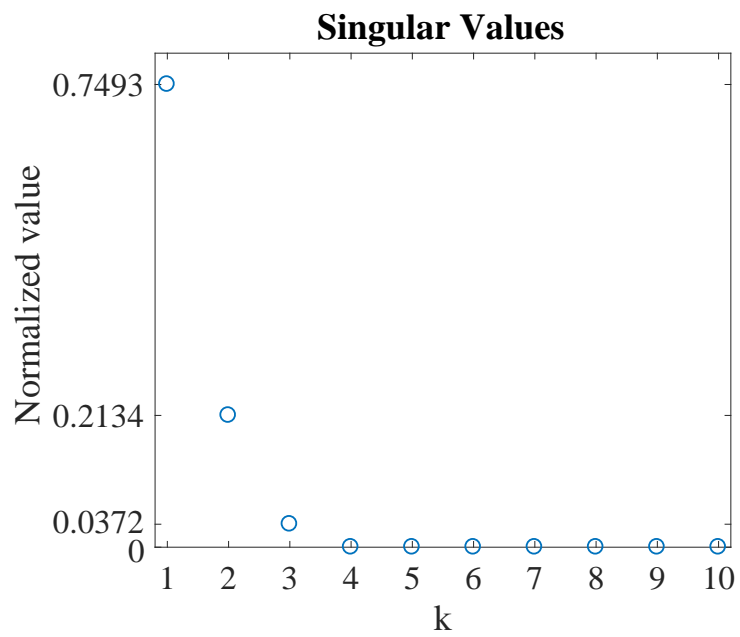
Figure 2.2: RLC case study singular values.
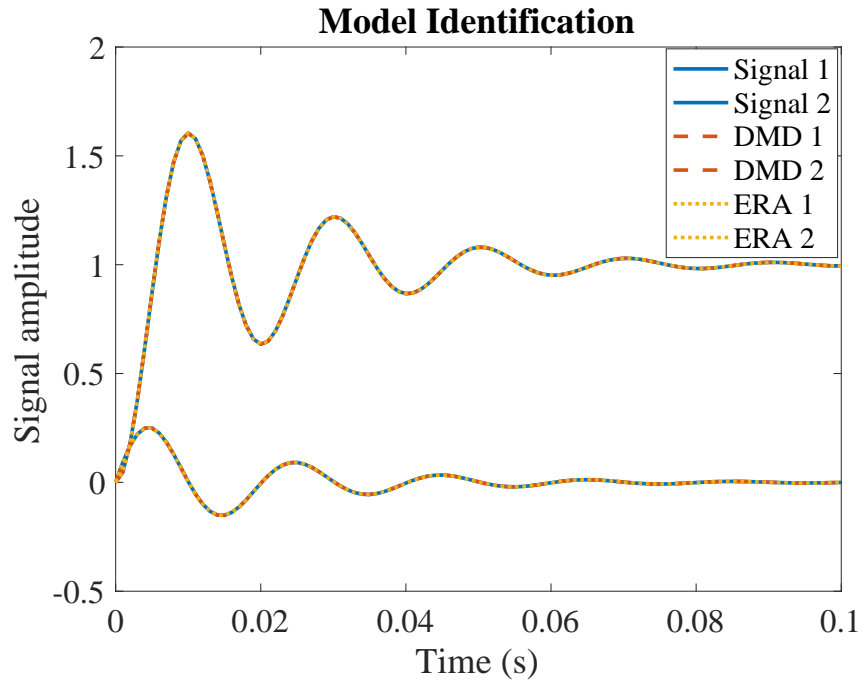
Figure 2.3: Base-case model along with DMD and ERA model identifications.
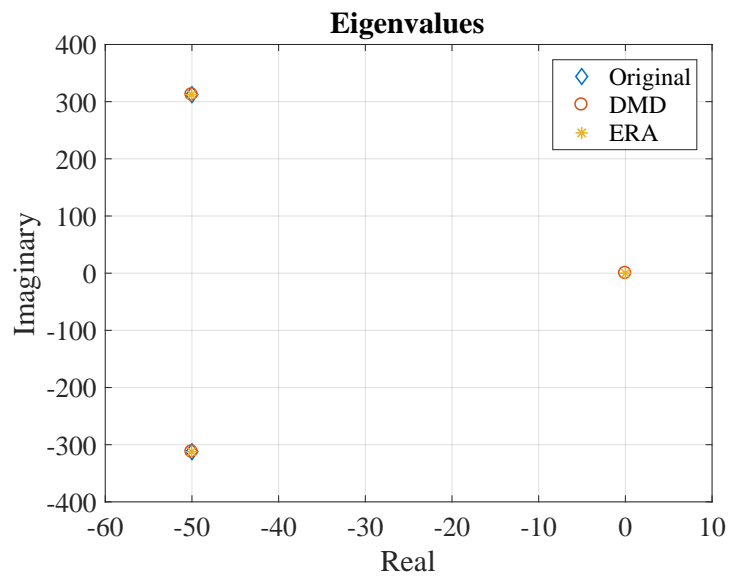
Figure 2.4: Base-case model, DMD, and ERA eigenvalues.

2.3.1.2   RLC Measurements with 10% Noises

Since the measurements of the real world inherently contain noises, 10% random noises are added to the measurement signals. The purpose of this case study is to inspect both DMD and ERA methods with noises. The DMD setting, data matrices size and the DMD rank, are in accordance with the base case. The DMD and ERA model identification solutions are shown in Fig. 2.5. Because the model eigenvalues with 10% noises are not known, we compare the DMD and ERA eigenvalues with each other and with the base case model eigenvalues. They are found in Fig. 2.6. It can be seen that while the ERA eigenvalues slightly change, the DMD eigenvalues standstill and match the original model.
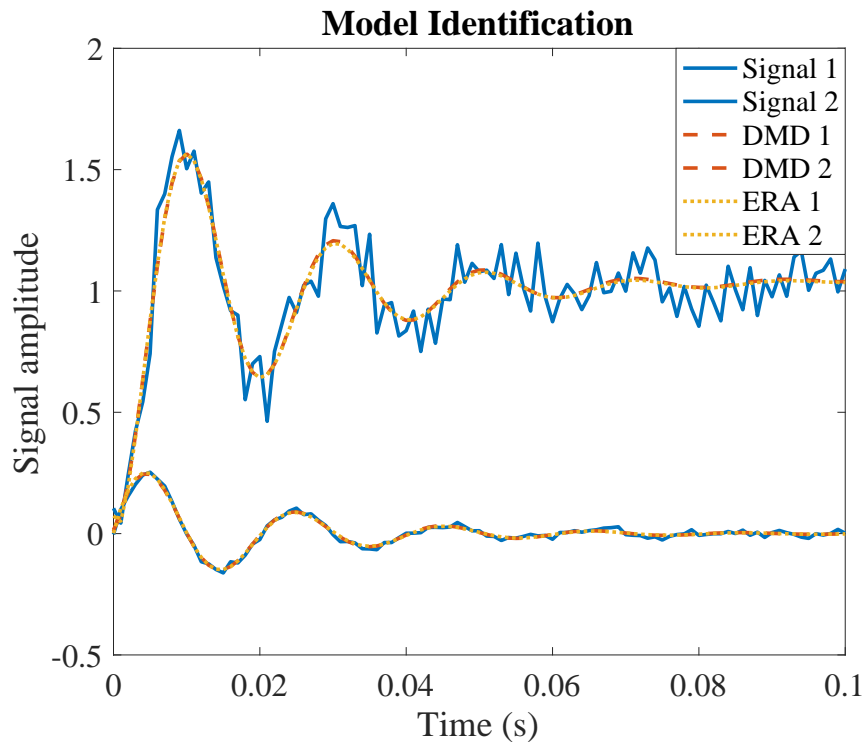
Figure 2.5: RLC with 10% noisy measurements. DMD and ERA can reconstruct the signal.
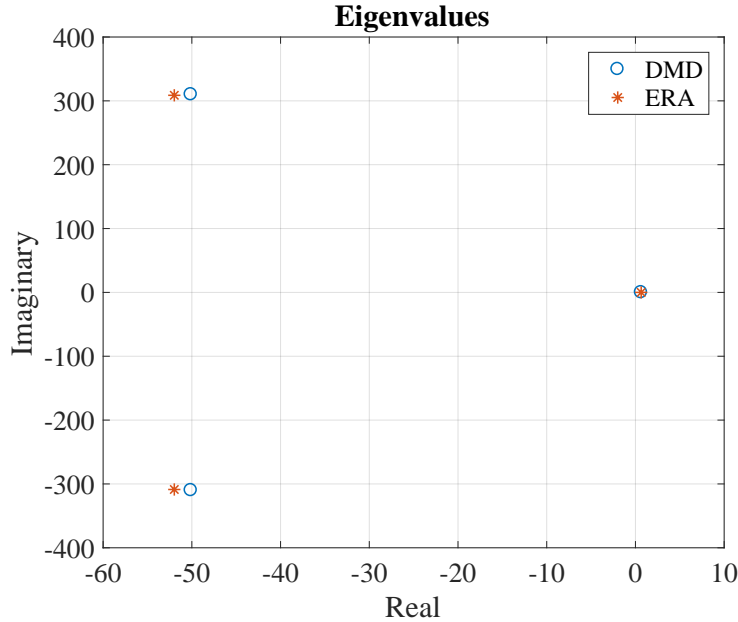
Figure 2.6: The DMD and ERA eigenvalues of 10% noisy measurements.

2.3.2 PMU Measurements

The DMD and ERA algorithms are implemented on PMU data of power measurements during an oscillatory event, taken from [24]. The data-set records 15 s, with a sampling rate of 0.05 s, after the event occurred in the grid. The measured signal points are 301, and they are plugged in the DMD. s, the time shift, is selected to be 150, so the size of $\mathbf{X_{aug,1}}$ and $\mathbf{X_{aug,2}}$ is (150×151). Due to the lack of information on the measured system, the system order can be estimated by considering the most effective singular values. The normalized singular values for this case are drawn in Fig. 2.7. Since the measurement contains noises, and our goal is to express the system without noises, the DMD rank is chosen to be the number of the most dominant singular values, which is 5. The DMD rank can be higher, but this adds ripples and meaningless eigenvalues to the identified model. Furthermore, if rank-reduction is not performed, all the singular values are included, the DMD fails to identify the model. The original measurements along with the DMD and the ERA identification are shown in Fig. 2.8. The DMD and ERA eigenvalues are found in Fig. 2.9. Although

the magnitude of the ERA eigenvalues tends to be slightly higher than the DMD's, both solutions are comparable.
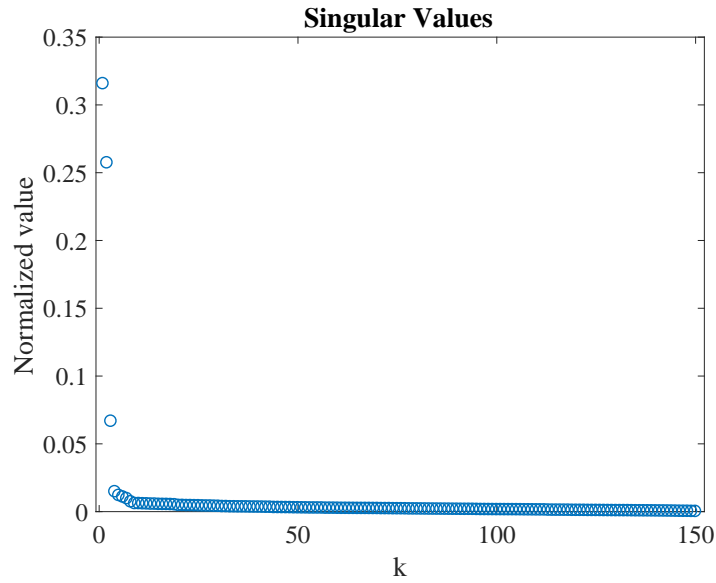
Figure 2.7: PMU measurement case study singular values.
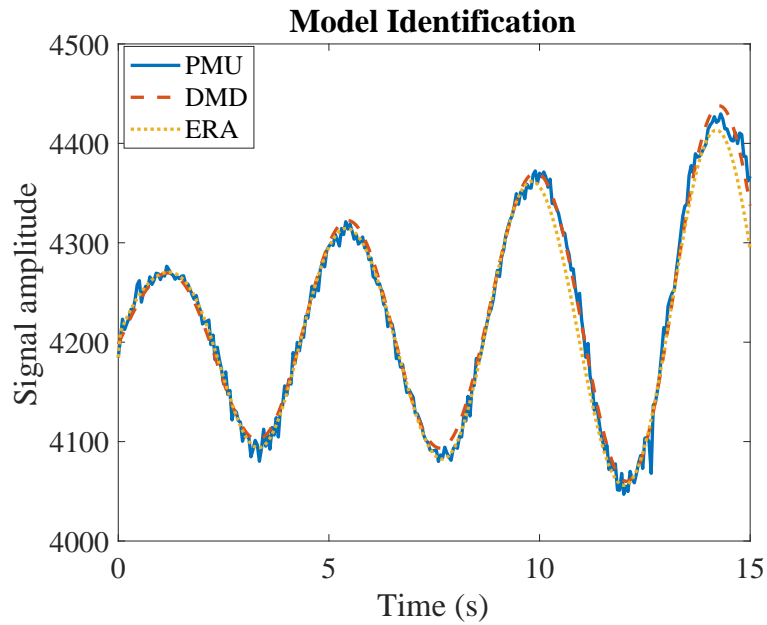
Figure 2.8: PMU measurements with DMD and ERA reconstructed signals.
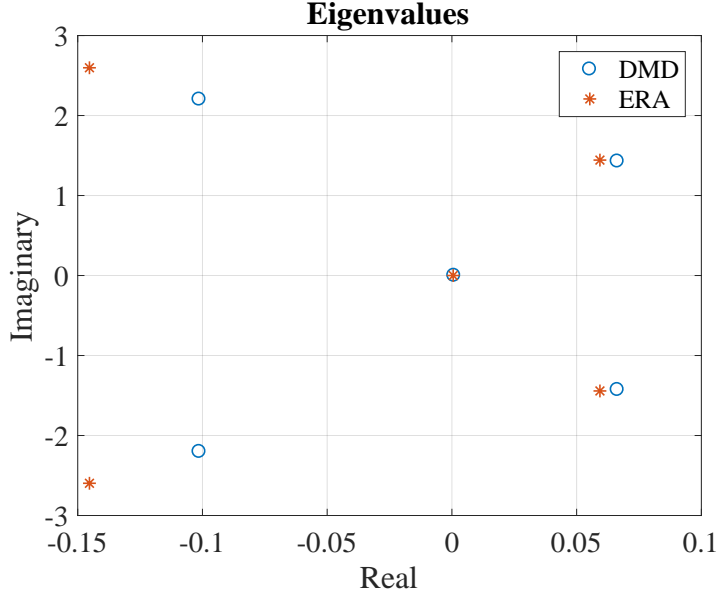
Figure 2.9: The DMD and ERA eigenvalues of the PMU measurements.

2.3.3 Abnormal Operation Analysis

The distribution-level system typically has unbalanced and harmonic frequency components. Moreover, faults and sudden disturbances add tremendous distortions to the network. Since these undesired electrical components greatly harm both the grid and the consumers' devices, a detailed analysis must be performed to track the disturbance issues. As an example, if the voltage has unbalanced and fifth-order harmonic components, the phase "a" voltage is represented as follows [25]

$$V_{sa}(t) = \widehat{V}_s \cos\left(\omega_0 t\right) + k_1 \widehat{V}_s \cos\left(\omega_0 t\right) + k_5 \widehat{V}_s \cos\left(5\omega_0 t\right), \tag{2.22}$$

where $\widehat{V}_s$ is the voltage peak magnitude. The negative and fifth-order harmonic components are k_1 and k_5, respectively. t represents time, whereas the system radian frequency is ω_0.

In this case study, (2.22) is used to mimic the real-world voltage measurement data, as it is taken through PMU. Then, the DMD algorithm is applied to the given data as if we do not know the original system. This reverse engineering technique demonstrates DMD ingenuity.

26

The values of this example are $\widehat{V}_s = 1$, $k_1 = 0.1$, $k_5 = 0.25$, and $\omega_0 = 2 * \pi * 60$. The voltage data and also the DMD identification are drawn Fig. 2.10, which appear distorted.

The voltage data-set duration is 0.1 s with a sampling rate of 0.001 s. So, the input signal is constructed of 101 samples. s is selected to be 50, that is, the size of $\mathbf{X_{aug,1}}$ and $\mathbf{X_{aug,2}}$ is (50×51). The singular values of this case are shown in Fig. 2.11. The effective singular values are 6, as expected since each cosine has two eigenvalues. Thus, the DMD rank is 6. DMD builds the system of which its eigenvalues are plotted Fig. 2.12. The DMD gives the ability to decompose the given signal, the modes are found in Fig. 2.13. Mode 1, mode 2, and mode 3 are associated with fundamental, fifth-harmonic, and negative components, respectively. The DMD arranges the signal modes in dominance order. Each mode has a participation factor to the original signal, as shown in Fig. 2.14.
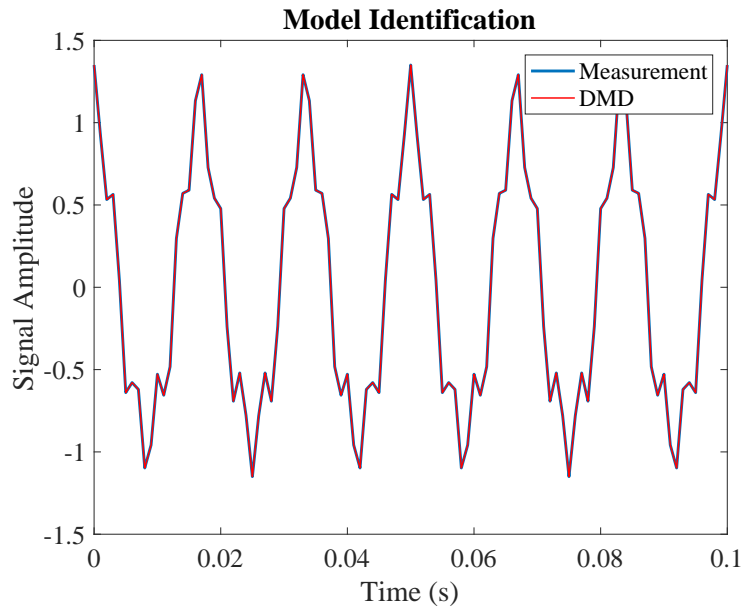
Figure 2.10: $V_{sa}(t)$ original data and the DMD identification.
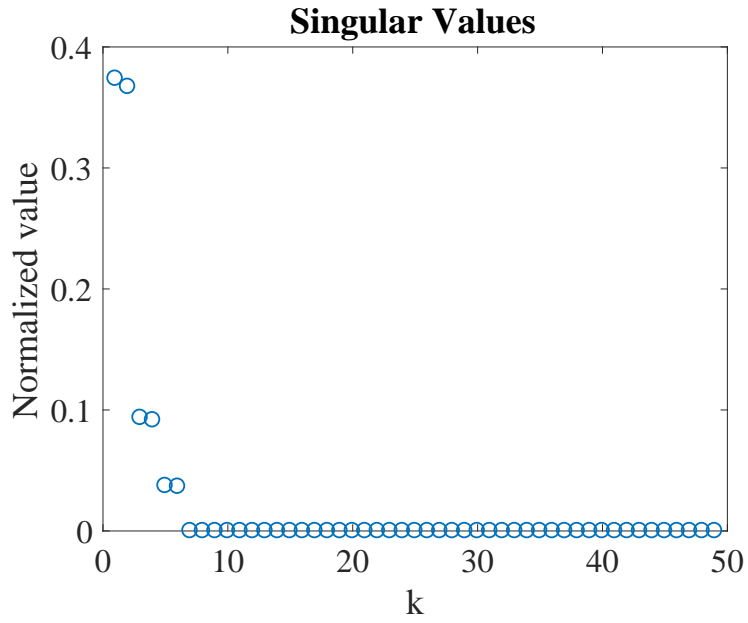
Figure 2.11: Voltage measurement singular values.
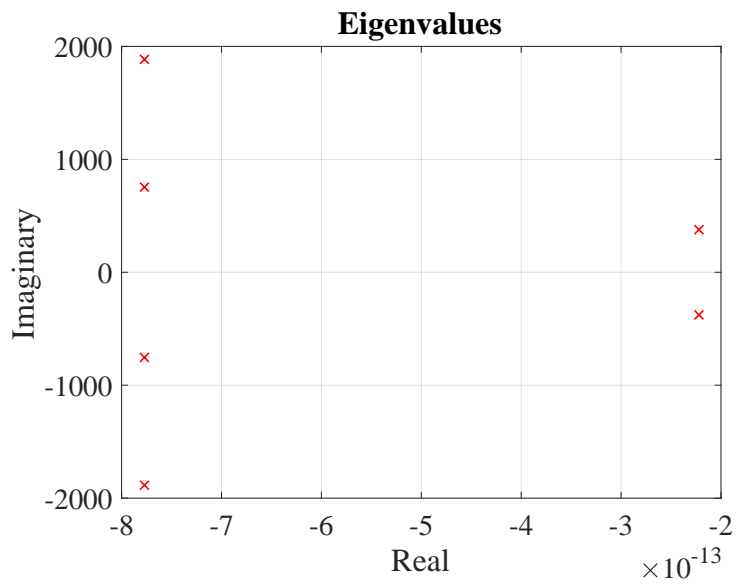
Figure 2.12: $V_{sa}(t)$ data eigenvalues from DMD.
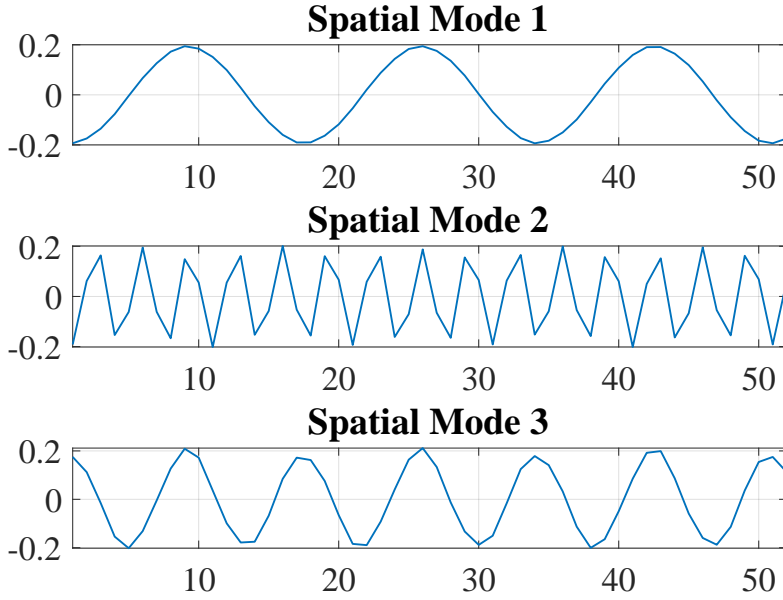
Figure 2.13: $V_{sa}(t)$ modes.
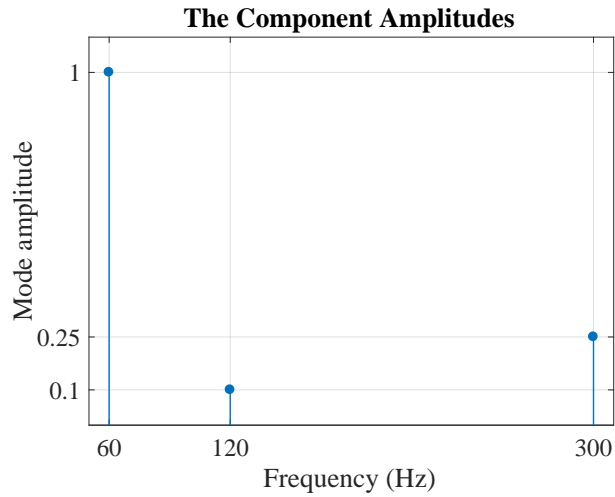
Figure 2.14: $V_{sa}(t)$ mode factors.

From this analysis, operational engineers have a closer look at the measured signal from which they can easily know all the system details and fix it. For instance, the given case study is found to contain second and fifth-order harmonic components, as engineers, we should directly investigate their cause.

Chapter 3: Randomized Dynamic Mode Decomposition for Oscillations

Power system measurement data tend to be high-dimensional and to have a low-ranked structure due to measurement redundancy and states correlation. Thanks to the recent randomized numerical methods, dealing with a large data matrix can be circumvented by a much smaller one with high accuracy. This research includes a randomization technique in computing the DMD algorithm as in [26]. This chapter[2] focuses on implementing the DMD on real-world PMU data to identify oscillation modes and distinct their nature using mode shape. The contribution of this chapter is three-fold.

- Compared to the major reference on DMD application in power system oscillation analysis [17], this research improves DMD implementation in signal reconstruction and DMD's performance in accuracy. (i) We not only implemented DMD to identify eigenvalues from PMU measurements but also reconstructed signals and can predict signals at any time t. This is realized by carrying out one more step to represent a data matrix's time-evolving characteristics. (ii) DMD's performance is improved by the data stacking technique. Accuracy in eigenvalue identification and measurement signal reconstruction has been greatly improved. Comparison of without and with data stacking technique is presented in this chapter.

- With the data stacking technique, the row dimension of the data matrix increases significantly. This causes more computing cost. We implement the randomization technique into DMD [26] and radically reduce the matrix dimension. In turn, the

---

[2]This chapter was published in IEEE Transactions on Power Systems [27]. Permission is included in Appendix A.

computing efficiency of DMD-based oscillation modal identification has been greatly improved.

- Relying on synchrophasor measurements collected by a region from scattered locations, the distinction between system wide-spread oscillation mode and regional oscillation mode can be made based on identified mode shapes associated with the measurements at different locations. PMU measurements from real-world oscillation events were used for this research. The analysis results match the knowledge of those real-world oscillations. The proposed method has been compared with the existing methods that are Prony, Matrix Pencil, and ERA in case studies.

3.1 Randomization Method

Our research on real-world event data shows that to achieve accuracy, the number s for data stacking is selected to be 30 - 40% of the measurement snapshots number. This number may be greater than 200. This results in large data matrices. Data handling requires more computing time. For computing efficiency, in this research, randomized DMD will be implemented. The objective is to replace the large-scale data matrix $\mathbf{X_{aug}} \in \mathbb{R}^{(s \cdot n) \times (m-s+1)}$ by a matrix with a smaller row dimension.

The process of the presented randomization method is to build a new small data matrix that reflects the original data matrix with adequate quality. The randomization technique that we employ was proposed by Halko et al. [28]. It consists of two stages: stage A and stage B. Moreover, two additional approaches (oversampling and power iteration scheme) are implemented to ensure the reduced data set has high quality.

3.1.1 Stage A

For the given data matrix, $\mathbf{X} \in \mathbb{R}^{n \times m}$, and the target rank $k \ll \min(m, n)$, we seek to find the optimal orthonormal basis $\mathbf{Q} \in \mathbb{R}^{n \times k}$ that holds:

$$\mathbf{X} \approx \mathbf{Q} \underbrace{\mathbf{Q}^* \mathbf{X}}_{\mathbf{H}}. \tag{3.1}$$

$\mathbf{H} \in \mathbb{R}^{k \times m}$ will be used to represent $\mathbf{X}$.

First, the column space of $\mathbf{X}$ is sampled. The sampling proceeds by projecting the original high-dimensional data onto a random matrix:

$$\mathbf{Y} = \mathbf{X}\boldsymbol{\Psi}, \tag{3.2}$$

where $\boldsymbol{\Psi} \in \mathbb{R}^{m \times k}$ is a normal Gaussian distribution matrix. $\mathbf{Y}$ is a set of linearly independent vectors that span in the range of $\mathbf{X}$. Consequently, the optimal basis $\mathbf{Q}$ can be efficiently achieved by means of QR-decomposition such that

$$\mathbf{Y} = \mathbf{Q}\mathbf{R}. \tag{3.3}$$

3.1.2 Stage B

Given the optimal basis $\mathbf{Q}$, the small data matrix $\mathbf{H} \in \mathbb{R}^{k \times m}$ is obtained by projecting the original matrix, $\mathbf{X}$, onto the computed basis $\mathbf{Q}$

$$\mathbf{H} = \mathbf{Q}^* \mathbf{X}. \tag{3.4}$$

It is worth mentioning that the original data matrix, $\mathbf{X}$, is preserved; it can be recovered as follows

$$\mathbf{X} \approx \mathbf{Q}\mathbf{H}. \tag{3.5}$$

The relationship of the original and reduced matrices is described in Fig. 3.1
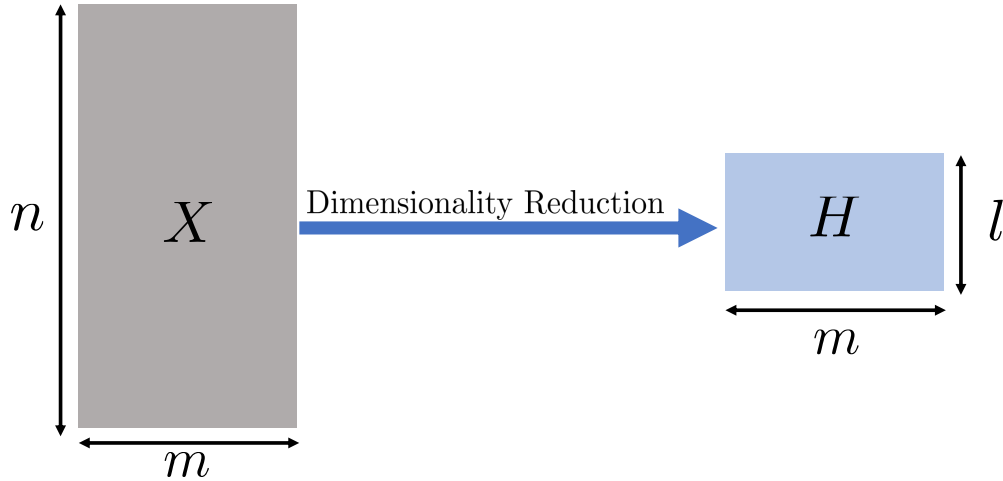
Figure 3.1: The dimensions of the original and reduced data matrices.

3.1.3 Oversampling

To ensure the column space of $\mathbf{Q}$ spans in $\mathbf{X}$ with high probability, extra samples are added from the measurements via the random matrix. Therefore, we have $\boldsymbol{\Psi} \in \mathbb{R}^{m \times l}$, where $l = k + p$. The parameter k is the rank of $\mathbf{X}$ and p denotes the extra samples. Reference [28] suggests setting p to 5 or 10 is sufficient to achieve correct results. In our case studies, we set $p = 10$.

3.1.4 Power Iteration Scheme

In case the data matrix, $\mathbf{X}$, has a slowly decaying singular value spectrum, the quality of the basis $\mathbf{Q}$ declines. The power iteration scheme dramatically fastens the singular value spectrum decaying [26]. Power iteration scheme is implemented as follows.

$$\mathbf{Y} = ((\mathbf{XX}^*)^q \, \mathbf{X}) \, \boldsymbol{\Psi}, \tag{3.6}$$

where q is an integer number that represents the power iterations. Although the cases in this research have high noises, setting $q = 2$ leads a sufficiently fast singular value spectrum.

Higher value of q conveys a more accurate solution, but at the cost of extra computation. If $\mathbf{X}$ is factorized using SVD and $\mathbf{X} = \mathbf{U}\boldsymbol{\Sigma}\mathbf{V}^*$, then (3.6) becomes the following: $\mathbf{Y} = ((\mathbf{XX}^*)^q\,\mathbf{X})\,\boldsymbol{\Psi} = \mathbf{U}\boldsymbol{\Sigma}^{2q+1}\mathbf{V}^*\boldsymbol{\Psi}$. The randomized technique is demonstrated in Algorithm 3.1.

Algorithm 3.1 Randomized technique [26]

Input: $\mathbf{X} \in \mathbb{R}^{n\times m}$, $k \ll \min(m, n)$, p, q

Output: $\mathbf{H} \in \mathbb{R}^{l\times m}$, $\mathbf{Q} \in \mathbb{R}^{n\times l}$

  1: $l \leftarrow k + p$

  2: $\boldsymbol{\Psi} \leftarrow \texttt{rand}(m, l)$

  3: $\mathbf{Y} \leftarrow \mathbf{X}\boldsymbol{\Psi}$, $\mathbf{Y} \in \mathbb{R}^{n\times l}$

  4: **for** $k = 1, \ldots, q$ **do**

  5:    $[\mathbf{Q}, \sim] = \texttt{qr}(\mathbf{Y})$

  6:    $[\mathbf{Z}, \sim] = \texttt{qr}(\mathbf{X}^*\mathbf{Q})$

  7:    $\mathbf{Y} = \mathbf{X}\mathbf{Z}$

  8: **end for**

  9: $[\mathbf{Q}, \sim] = \texttt{qr}(\mathbf{Y})$

10: $\mathbf{H} \leftarrow \mathbf{Q}^*\mathbf{X}$

3.2 Randomized DMD

While data stacking improves DMD performance, it increases the computation cost. This section provides computation enhancement to the algorithm process. The methodology relies on including the randomization technique in the DMD steps. This method is proposed by Erichson et al. [26]. The result of the rDMD matches standard DMD. The rDMD is implemented after computing the optimal orthonormal basis $\mathbf{Q}$ from Algorithm 3.1. The high-dimensional measurement snapshots are projected onto $\mathbf{Q}$ as follows.

$$\mathbf{h}_1, \mathbf{h}_2, \ldots, \mathbf{h}_m := \mathbf{Q}^*\mathbf{x}_1, \mathbf{Q}^*\mathbf{x}_2, \ldots, \mathbf{Q}^*\mathbf{x}_m \in \mathbb{R}^l. \tag{3.7}$$

The new low-dimensional snapshots are gathered into two overlapping matrices just as in (2.9)

$$\mathbf{H}_1^{m-1} = \begin{bmatrix} | & | & & | \\ \mathbf{h}_1 & \mathbf{h}_2 & \cdots & \mathbf{h}_{m-1} \\ | & | & & | \end{bmatrix}, \tag{3.8a}$$

$$\mathbf{H}_2^{m} = \begin{bmatrix} | & | & & | \\ \mathbf{h}_2 & \mathbf{h}_3 & \cdots & \mathbf{h}_{m} \\ | & | & & | \end{bmatrix}, \tag{3.8b}$$

where $\mathbf{H}_1^{m-1}$, $\mathbf{H}_2^{m} \in l \times (m-1)$. Then, the dynamics matrix that maps the two low-dimensional sets is computed using least-squares estimation:

$$\begin{aligned} \mathbf{A_h} &= \mathbf{H}_2^{m}(\mathbf{H}_1^{m-1})^{\dagger} \\ &= \mathbf{H}_2^{m}\mathbf{V}\boldsymbol{\Sigma}^{-1}\mathbf{U}^*, \end{aligned} \tag{3.9}$$

where $\mathbf{A_h} \in \mathbb{R}^{l \times l}$, $\mathbf{U} \in \mathbb{R}^{l \times k}, \boldsymbol{\Sigma} \in \mathbb{R}^{k \times k}$, and $\mathbf{V} \in \mathbb{R}^{(m-1) \times k}$. $\mathbf{U}, \boldsymbol{\Sigma}$, and $\mathbf{V}$ are the truncated SVD components of $\mathbf{H_1}^{(m-1)}$. $\mathbf{A_h}$ is projected onto $\mathbf{U}$ basis to make it even smaller:

$$\tilde{\mathbf{A}}_h = \mathbf{U}^*\mathbf{A_h}\mathbf{U} = \mathbf{U}^*\mathbf{H}_2^{m}\mathbf{V}\boldsymbol{\Sigma}^{-1}, \tag{3.10}$$

where $\tilde{\mathbf{A}}_h \in \mathbb{R}^{k \times k}$. Next, the eigendecomposition is implemented to obtain the system eigenvalues and eigenvectors:

$$\tilde{\mathbf{A}}_h\mathbf{W_h} = \mathbf{W_h}\boldsymbol{\Lambda_h}, \tag{3.11}$$

where $\boldsymbol{\Lambda_h} \in \mathbb{C}^{k \times k}$, and $\mathbf{W_h} \in \mathbb{C}^{k \times k}$. The DMD modes are recovered as

$$\boldsymbol{\Phi_h} = \mathbf{QUW_h}, \tag{3.12}$$

Algorithm 3.2 Randomized Dynamic Mode Decomposition

Input: $\mathbf{H} = [\,\mathbf{h_1}\ \mathbf{h_2}\ \mathbf{h_3} \ldots \mathbf{h_m}\,] \in \mathbb{R}^{l \times m}$, $\mathbf{Q} \in \mathbb{R}^{n \times l}$

Output: $\boldsymbol{\Phi_h} \in \mathbb{C}^{n \times k}$, $\boldsymbol{\Lambda_h} \in \mathbb{C}^{k \times k}$, $\mathbf{W_h} \in \mathbb{C}^{k \times k}$, $\mathbf{b_h} \in \mathbb{C}^{k \times 1}$.

1: $\mathbf{H_1} \leftarrow [\,\mathbf{h_1}\ \mathbf{h_2}\ \mathbf{h_3} \ldots \mathbf{h_{m-1}}\,]$, $\mathbf{H_1} \in \mathbb{R}^{l \times m-1}$,
   $\mathbf{H_2} \leftarrow [\,\mathbf{h_2}\ \mathbf{h_3}\ \mathbf{h_4} \ldots \mathbf{h_h}\,]$, $\mathbf{H_2} \in \mathbb{R}^{l \times m-1}$.

2: $[\mathbf{U}, \boldsymbol{\Sigma}, \mathbf{V}] = \mathtt{svd}\,(\,\mathbf{H_1}\,)$,
   $\mathbf{U} \in \mathbb{R}^{l \times k}, \boldsymbol{\Sigma} \in \mathbb{R}^{k \times k}, \mathbf{V} \in \mathbb{R}^{m-1 \times k}$.

3: $\tilde{\mathbf{A}}_h \leftarrow \mathbf{U}^* \mathbf{H_2} \mathbf{V} \boldsymbol{\Sigma}^{-1}$, $\tilde{\mathbf{A}}_h \in \mathbb{R}^{k \times k}$

4: $[\mathbf{W_h}, \boldsymbol{\Lambda_h}] = \mathtt{eig}(\tilde{\mathbf{A}}_h)$.

5: $\boldsymbol{\Phi_h} \leftarrow \mathbf{Q} \mathbf{U} \mathbf{W_h}$.

6: $\mathbf{b_h} \leftarrow \boldsymbol{\Phi_h}^{\dagger} \mathbf{Q} \mathbf{h_1}$.

---

where $\boldsymbol{\Phi_h} \in \mathbb{C}^{n \times k}$. The vector mode amplitudes, $\mathbf{b_h}$, is evaluated as

$$\mathbf{b_h} = \boldsymbol{\Phi_h}^{\dagger} \mathbf{Q} \mathbf{h_1}, \tag{3.13}$$

where $\mathbf{b_h} \in \mathbb{C}^{k \times 1}$. The randomized dynamic mode decomposition is outlined in Algorithm 3.2.

In the following section, DMD and rDMD will be demonstrated on real-world event data analysis. All calculations were performed in MATLAB on a laptop with an Intel Core i7 CPU and 16Gb of memory.

3.3 An Illustrative Example: Oscillation Event in Two-Area System

In this case study, we implement our analysis on the classic two-area four-machine system for inter-area oscillation study [29]. This system has an order of 8, with each generator represented by 2nd order swing dynamics. The two-area system was made for a research report commissioned from Ontario Hydro by the Canadian Electrical Association [29], shown in Fig. 3.2. The case study we carry out was introduced in [29] that is a sudden disturbance occurs in area 1. A step change of the mechanical torque of +0.1 p.u. is applied on G1 and of −0.1 p.u. is applied on G2. This kind of event creates both inter-area and local modes. While [29] analyzes the system response using a model-based method, we do it

Table 3.1: Two-area system event computation details.

Voltage Data	DMD	rDMD
Matrix Dimension	39×997	18×997
Computation Time (s)	0.0063	0.0038
Phase Angle Data	**DMD**	**rDMD**
Matrix Dimension	39×997	19×997
Computation Time (s)	0.0111	0.0049
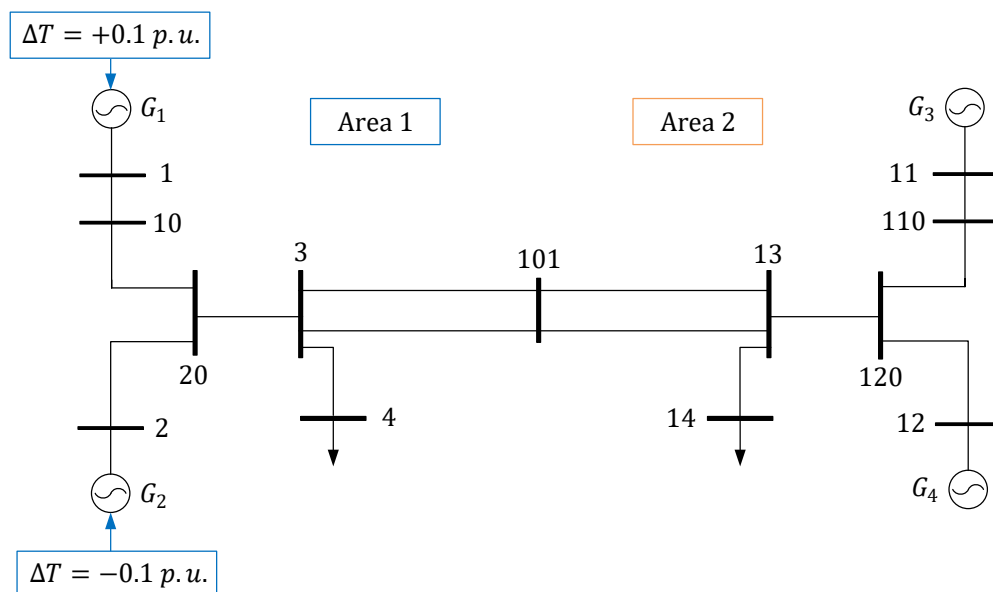
Figure 3.2: Two-area system with mechanical torque disturbance.

using a measurement-based method, DMD and rDMD. The measurements used in this case study are simulation data from Power System Toolbox[30]. Sampling time (Δt) is 0.01 s. The randomized decomposition computation time for voltage magnitude data as an input is 0.0031 s and for phase angle data as an input is 0.0043 s. The DMD and rDMD computation details are shown in Table 3.1.

3.3.1 Model Identification

The simulated measurements of the disturbance event are used as a DMD input; DMD will be applied for the set of the voltage magnitude (or phase angle) data from 13 buses.

The signals will be reconstructed by DMD, as in (2.8). The DMD signals are compared with the original signals to examine accuracy. In case the original measurement signals have noises, the DMD rank is adjusted. In this case study, we use all the bus voltage magnitude and phase angle measurements as an input to both DMD and rDMD. The DMD reconstructed signals for the voltage magnitudes and phase angles are compared with the original voltage magnitude and phase angle signals in Fig. 3.3a and Fig. 3.3b, respectively. Excellent matching is demonstrated.

Although it is possible to implement the DMD with the voltage magnitudes and phase angles are lumped together in a set as an input, we implement them separately to investigate the details of the analyzed data. With the voltage magnitudes or phase angles as an input, it is only possible to achieve a good match between the measurement and the reconstructed signals when the shift-stacking, s, is ≥ 3. For this, we set $s = 3$ and that makes the DMD input matrix size change from (13×999) to (39×997).

The shift-stacking scheme enlarges the number of subspaces that define the analyzed nonlinear system. Shift-stacking the measurement data for the voltage magnitudes does not affect the system order.

The rank of the estimated system is set as 8 with voltage magnitudes as measurement. The 8 eigenvalues match the model-based eigenvalues.

With the phase angles as measurement, the DMD and rDMD eigenvalues are shown in Fig. 3.4a. The model reduction, in this case, is set according to the system order, since we already know it. This also can be confirmed by examining the energy of the singular values, shown Fig. 3.4b, which are the diagonal entries of the matrix Σ.
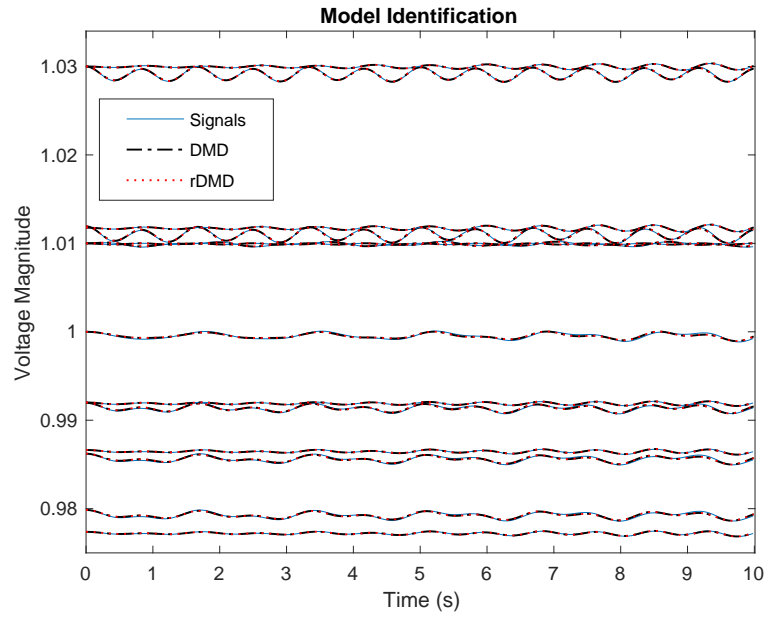
(a)
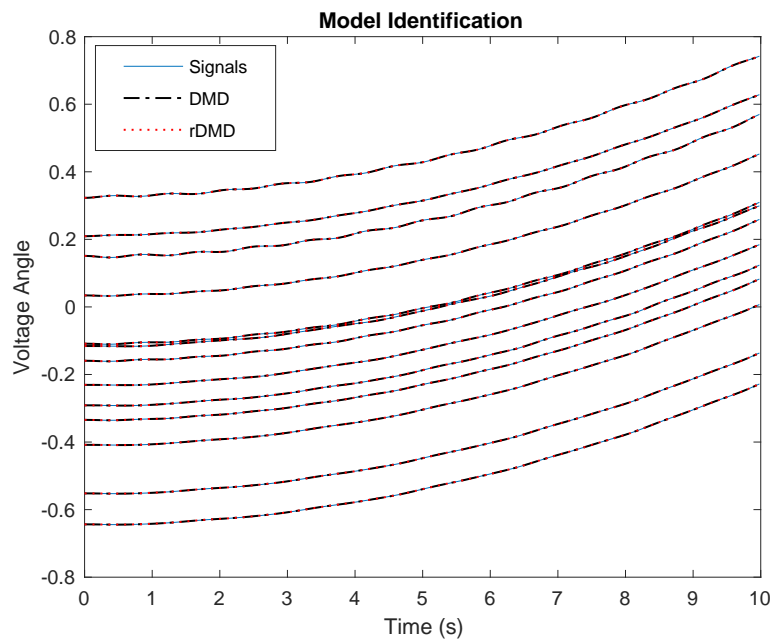
(b)

Figure 3.3: DMD reconstructed signals of the two-area system event. (a) bus voltage magnitudes, (b) bus phase angles. Excellent match is observed.
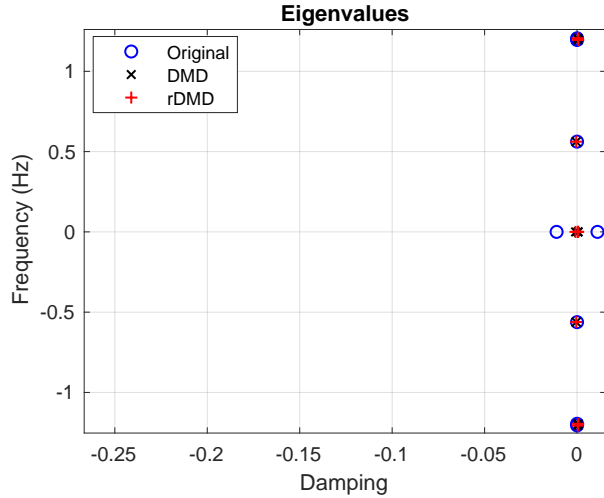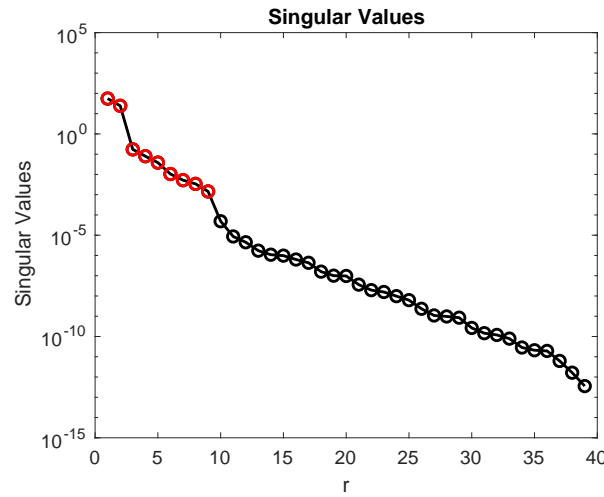
Figure 3.4: Two-area event: (a) eigenvalues, and (b) singular value energies.

3.3.2 Mode Shapes Analysis

Mode shapes are the eigenvectors associated with the system eigenvalues; they portray how the system evolves in time. In DMD, with taking the bus phase angles under consideration, the mode shapes are the column vectors of the DMD mode, $\mathbf{\Phi}$. The DMD mode of rDMD matches the standard DMD. For the given case study after the applied disturbance, the mode shapes for the dominant modes are shown in Fig. 3.5 for the generators.
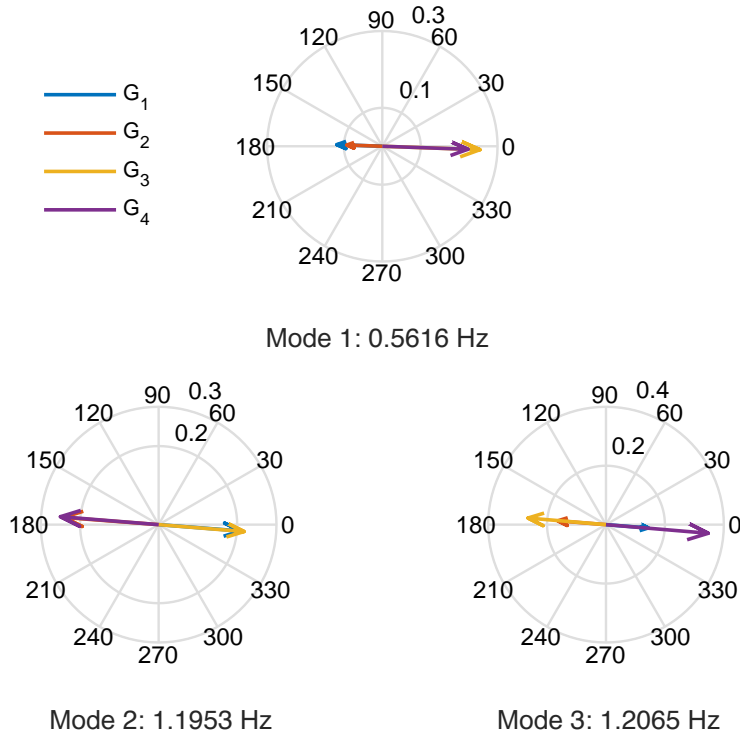
Figure 3.5: The mode shape of the dominant mode of the two-area event.

The first mode is the only inter-area component in the system, and its associated mode shapes appear on top of Fig. 3.5. The mode shapes of the inter-area mode show that Area 1 oscillates against Area 2. In other words, the disturbance of Area 1 initiates an oscillation that spreads to Area 2 causing the two areas to oscillate against each other. It can be seen that this mode primarily affects the generator buses of the undisturbed area. Another interpretation of the mode shapes is that the inter-area oscillation mode can be observed and controlled the best at the buses that have higher magnitudes. For instance, for this mode, bus 11, which contains G_3, is the optimal place for PMU and stabilizer; the PMU observes the modes, and the stabilizer controls it. The second and third modes, shown at the bottom of Fig. 3.5, are related to local oscillations in which the generators of the same area oscillate against each other.

3.4 Real-World Oscillation Event Case Studies

This section presents the implementation of DMD and rDMD on three real-world oscillation events. These events occurred in ISO New England, a North-East part of the Eastern Interconnection in the united states. The ISO New England has peak load of 26,000 MW. Data and brief descriptions of the three events are from Test Cases Library of Power System Sustained Oscillations [31]. The sampling period, Δt, is 0.033 second. Table 3.2 presents the three events descriptions from [31].

Table 3.2: Real-world event descriptions.

Case #	Date	PMU	Type	Frequency (Hz)
1	June 17, 2016	ISO-NE	System-wide mode	0.27
2	Oct 3, 2017	ISO-NE	Wide-spread	0.08, 0.15 0.31
3	Jul. 20, 2017	ISO-NE	Regional	1.13

3.4.1 Oscillation Event 1

On June 17, 2016, an emergency shutdown due to control failure of a nuclear reactor occurred in the Grand Gulf Nuclear Station that is in Area 2. The cause of the failure was hydraulic control valve malfunctioning. As a result, 65 percent of the power load was dropped from the system, and a forced oscillation frequency around 0.28 Hz was imposed in the system for about 45 minutes [2]. We analyze the 32 voltage magnitude signals that are shown Fig. 3.6.

Data from 40 to 60 seconds are used for analysis. Without shift-stacking, the DMD is unable to identify the system and reconstruct the signals, as shown in Fig. 3.7a. Shift-stacking the event data enables the DMD to accurately identify the system modes and reconstruct the signals from the DMD's components, as shown in Fig. 3.7b. For this case, excellent matching of reconstructed and original signals is achieved with the shift-stacking number s at 250. The data matrix's dimension changes from (32×705) to (8000×456) that

is from $(n \times m)$ to $(n \cdot s \times m - s + 1)$. The proposed rDMD reduces the size to (26×456), which is $(k + p \times m - s + 1)$, while analysis accuracy is preserved.
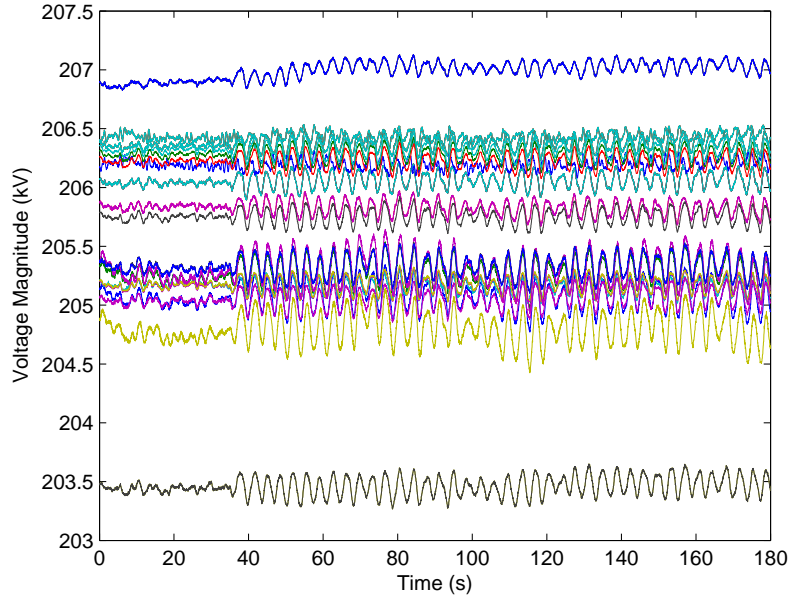
Figure 3.6: Phase-to-ground voltage magnitude of event 1.

The randomized decomposition computation time is 0.0165 s. The DMD and rDMD computation details are shown in Table 3.3.

Table 3.3: Real-world event 1: computation details.

Event 1: Voltage Magnitudes	DMD	rDMD
Matrix Dimension	8000×456	26×456
Computation Time (s)	0.2282	0.0079
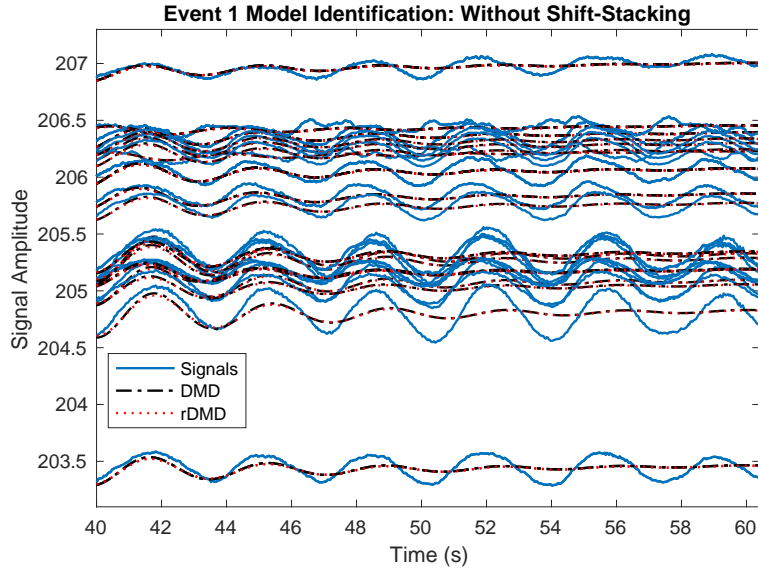
(a)
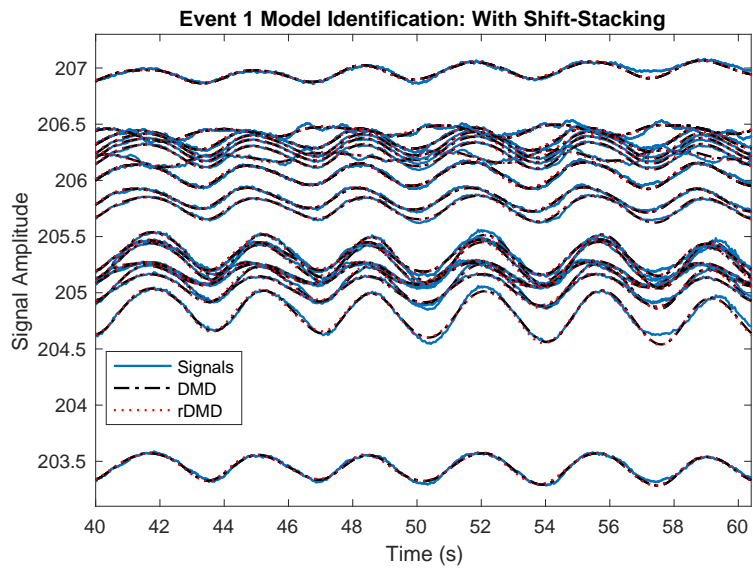
(b)

Figure 3.7: Comparison of data stacking for event 1.

Since the measurement data are expected to be corrupted by noises, we examine the singular value energies before we truncate the model through the SVD elements. Fig. 3.8 shows the Event 1 singular value energies and cumulative energies. Setting the DMD rank to 16 holds 99.95% of the data information. Consequently, both the DMD and rDMD identify 16 eigenvalues that are shown Fig. 3.9.
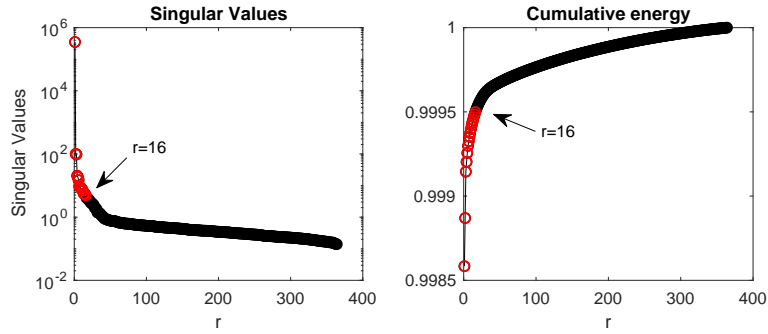
Figure 3.8: The singular value energies and cumulative energy of event 1.
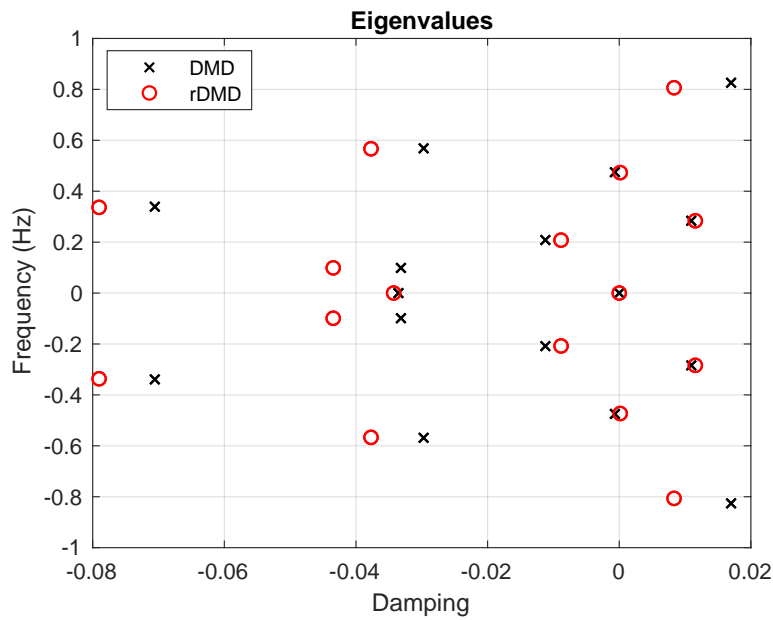
Figure 3.9: The DMD and rDMD identified eigenvalues for event 1.

The DMD spectrum determines the dominant modes in the analyzed system; for this case, the DMD spectrum is shown in Fig. 3.10. The dominant oscillation mode is at 0.28 Hz, which matches NERC report[2].
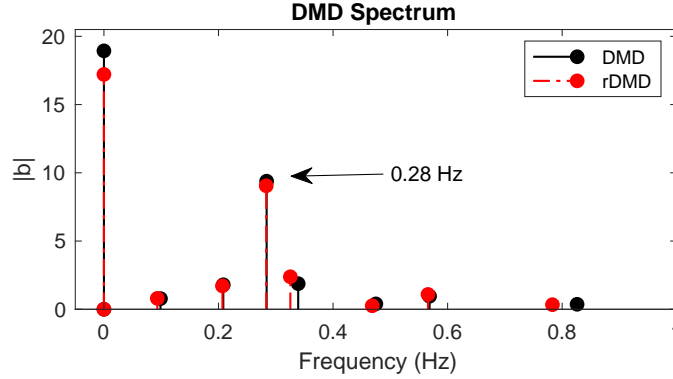
Figure 3.10: DMD spectrum of event 1.

It can be concluded from the mode shape that Substation 9 is most related to this mode as the mode shape's magnitude at Substation 9 is the largest. It is worth mentioning that measurements from substations in ISO NE show similar angles for this mode. This indicates that the entire ISO NE oscillates as a whole for this mode. This information can be used to judge that 0.28 Hz mode is an inter-area oscillation mode.

3.4.2 Oscillation Event 2

On October 3, 2017 inter-area oscillations of 0.08 Hz, 0.15 Hz, and 0.31 Hz were initiated and dispersed in the New England power system. The oscillations source was at an external area (Area 3), where an issue had occurred on a large generator governor. The oscillations lasted in the network for about 5 minutes. Our goal is to identify oscillation modes and judge their nature from the New England event voltage measurements that are shown in Fig. 3.11.

Both DMD and rDMD are implemented on a time window from 250 to 280 s for all the given PMU voltage magnitude signals. The DMD without shift-stacking the data is incapable to identify the event and reconstruct the signals, as appeared in Fig. 3.12a. On the other hand, the DMD with shift-stacking the data has the ability to identify and reconstruct the signals, as shown in Fig. 3.12b. The analyzed data size is (22×910). The DMD reconstructed signals match the original signals with a stack number $s = 350$. The randomized

decomposition computation time is 0.0358 s. The DMD and rDMD computation details are shown in Table 3.4.
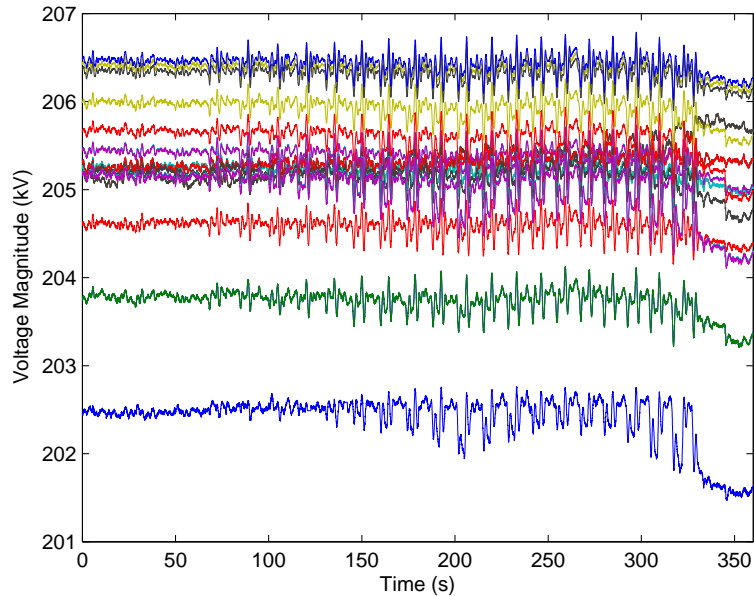
Figure 3.11: Phase-to-ground voltage magnitudes of event 2.

Table 3.4: Real-world event 2: computation details.

Event 2: Voltage Magnitudes	DMD	rDMD
Matrix Dimension	7700×561	40×561
Computation Time (s)	0.3008	0.0107

For this case, the cumulative energy of the first 30 of the singular values is 99.94%. By comparison with Event 1 case in which the first 16 of the singular values have cumulative energy of 99.95%, one can conclude that Event 2 includes more dynamics and noises than Event 1. According to the singular values, the DMD rank is set to 30. Therefore, the DMD and rDMD identify 30 eigenvalues that are shown in Fig. 3.13. They show a close match.

The Event 2 DMD spectrum, shown in Fig. 3.14, indicates that the event dominant modes are 0.0833 Hz, 0.1489 Hz, and 0.3056 Hz. The identified modes have frequencies agreeing

with the info in Table 3.2. Finally, the mode shapes based on voltage phase angles are shown in Fig. 3.15. The plots indicate all three modes are inter-area oscillation modes.
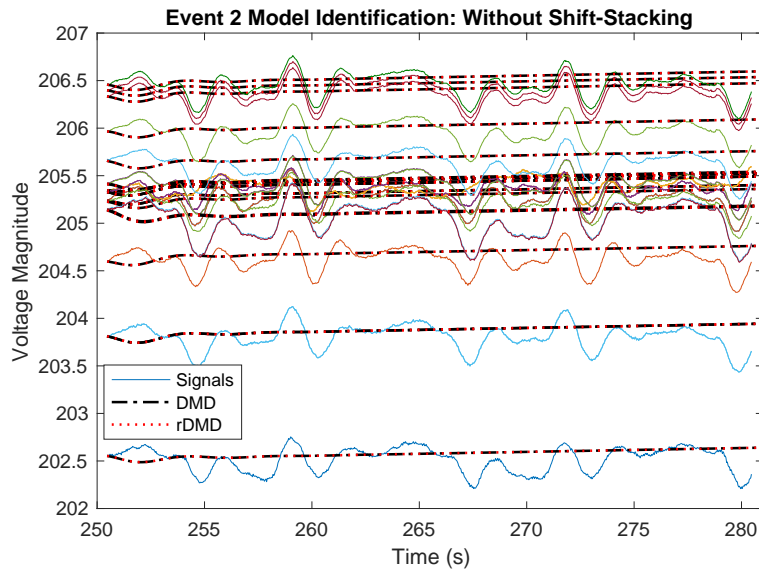
(a)
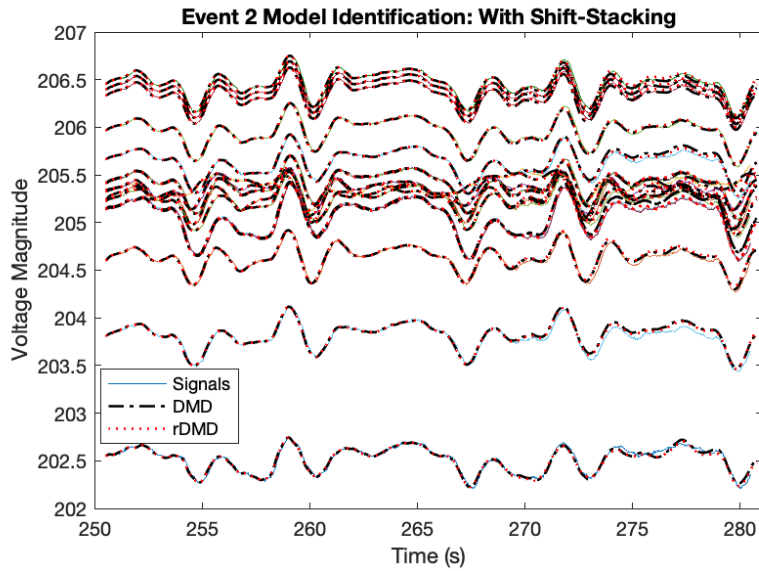
(b)

Figure 3.12: Comparison of signal reconstruction for event 2. (a) without stacking. (b) with data stacking.
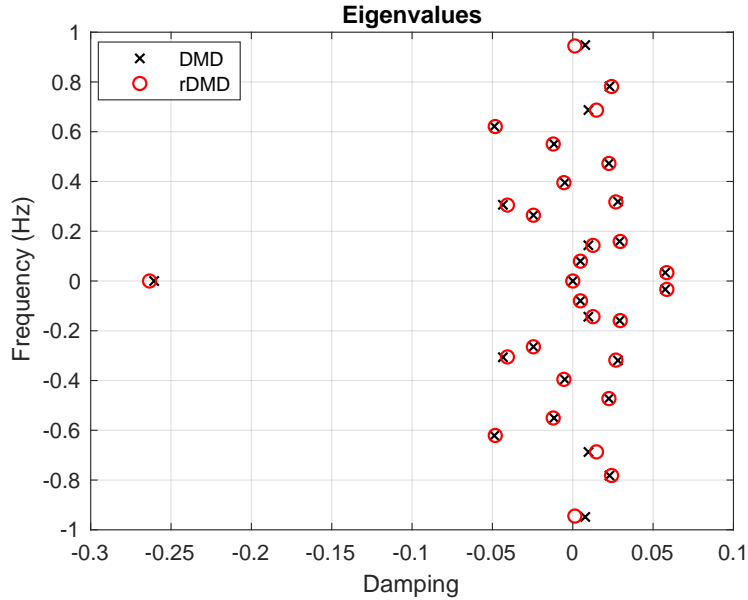
Figure 3.13: Event 2: eigenvalues identified by DMD and rDMD.
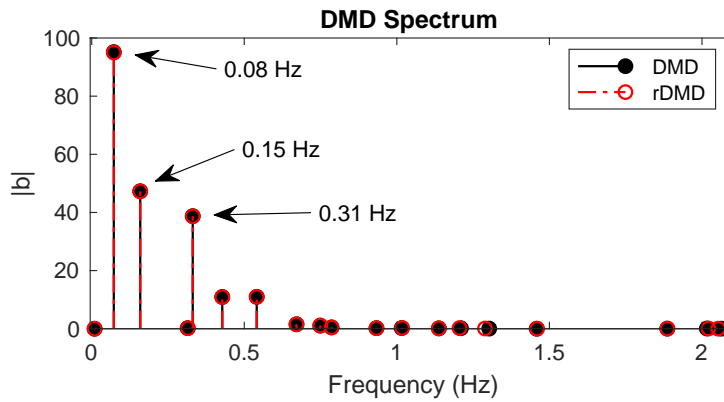
Figure 3.14: DMD spectrum of event 2.

3.4.3 Oscillation Event 3: Comparison with Classical Methods

On July 20, 2017, a disturbance in a large generator initiated growing regional oscillations in Area 1. The number of the PMUs that recorded the event is 35, the voltage magnitude measurements are shown in Fig. 3.16. In this case study, we show a comparison between the DMD/rDMD and the classical identification methods that are Prony, Matrix Pencil (MP), and ERA. The analyzed ringdown response is the voltage magnitude from 51 to 65 second.
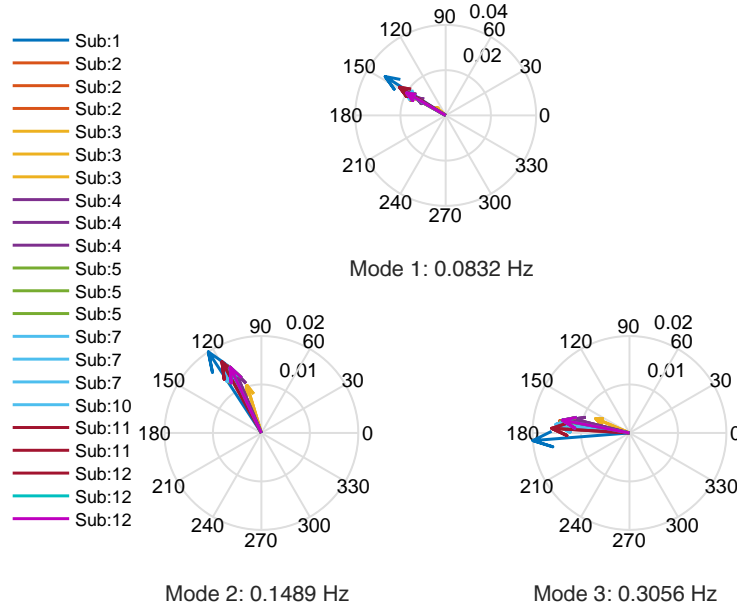
Figure 3.15: The dominant mode shapes of event 2.

The signal reconstruction of the tested methods is compared with PMU voltage in Fig. 3.17. The data matrix has 20 effective singular values and correspondingly the rank of all the tested methods is 20. The mismatching error of all of the algorithms are shown in Fig. 3.18, and their computation times are in Table 3.5. It can be seen that the mismatching errors of DMD and rDMD are the lowest, which indicates DMD and rDMD lead to the most accurate reconstructed signals.

3.4.4   Mode Shape Analysis for The Dominant Mode

Mode shape analysis based on frequency measurements has been used in the industry to distinct oscillation types, e.g., [2]. In this subsection, frequency measurements will be used for DMD analysis, and further mode shape (ϕ_i of the ith mode) of the dominant modes will be plotted for oscillation type analysis. Fig. 3.19a and Fig. 3.19b present the frequency

Table 3.5: Real-world event 3: algorithm computation time.

Algorithm	rDMD	DMD	MP	Prony	ERA
Time (s)	0.0769	0.1467	0.7310	1.8357	2.3675
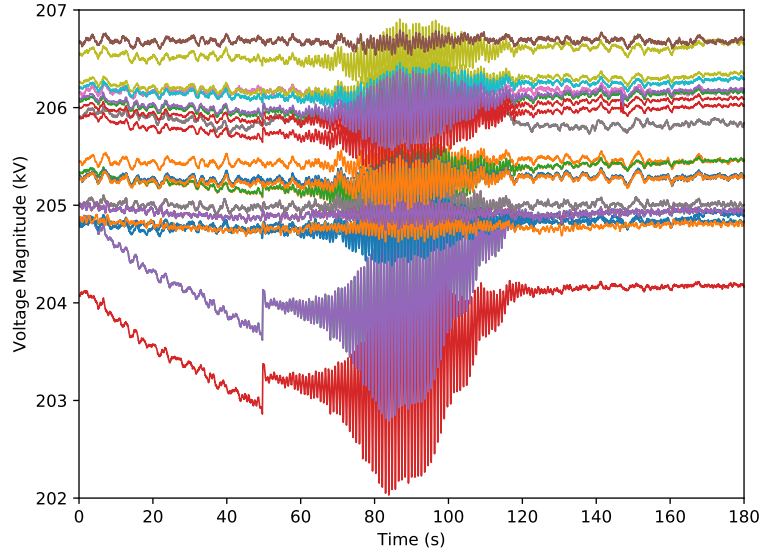
Figure 3.16: Phase-to-ground voltage magnitudes of event 3.

measurements of the two events used for DMD analysis. For Event 1, 20 seconds data are used while, for Event 3, 40 seconds data are used. Randomized DMD successfully identifies eigenvalues and the reconstructed signals are also shown in Fig. 3.19a and Fig. 3.19b. The dominant mode of Event 1 is the 0.28 Hz mode which has been also identified using the voltage magnitude data while the dominant mode of Event 3 is a 1.14 Hz mode. A complete s-domain eigenvalue location plot based on Event 3 data is shown in Fig. 3.20. The dominant mode is the 1.14 Hz mode.

Mode shapes corresponding to the dominant mode for each event are plotted in Fig. 3.21. It can be seen that for Event 1 for the 0.28 Hz mode, mode shapes corresponding to the substations at New England have almost the same angles. That is, for this mode, the entire New England can be treated as a single generator. This mode is indeed an inter-area oscillation mode. On the other hand, mode shape plot of the 1.14 Hz mode of Event 3 indicates that the mode shape vectors of New England substations are not contained in a cone with a small angle. Rather, the angles are quite different. [31] identified the dominant mode of Event 3 as a regional mode. This feature is also confirmed by Fig. 3.21b.
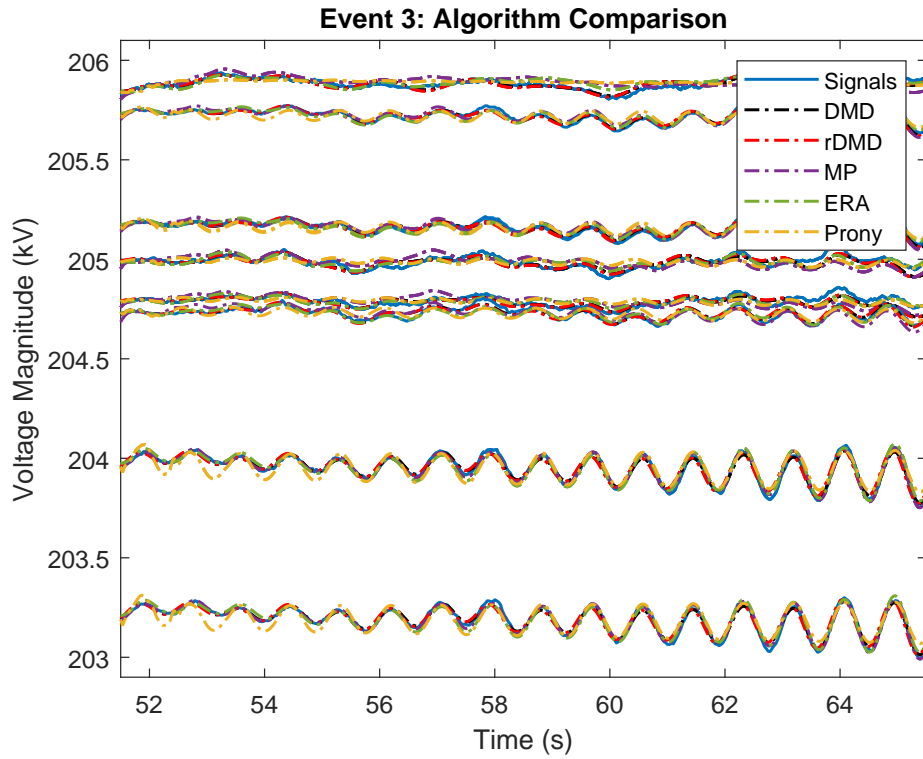
Figure 3.17: Algorithms comparison on event 3.
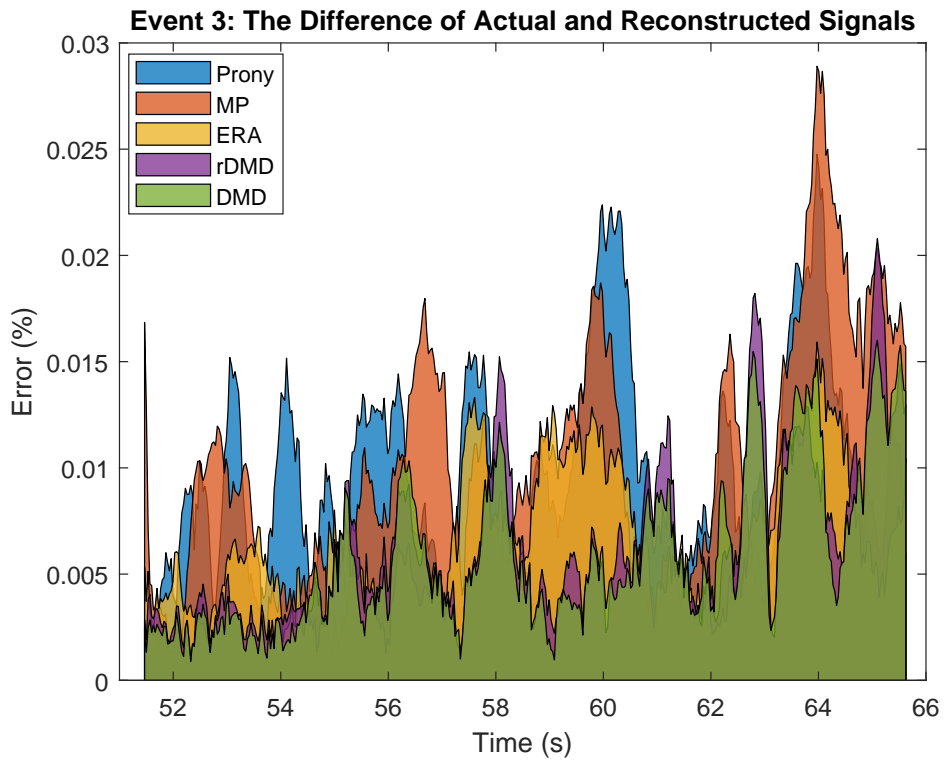
Figure 3.18: The reconstruction signal error of the algorithms on event 3.
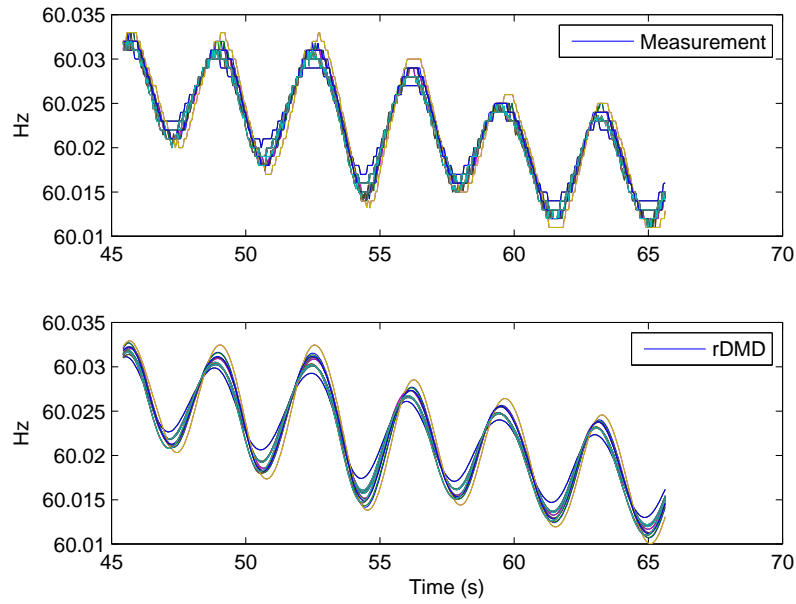
(a)
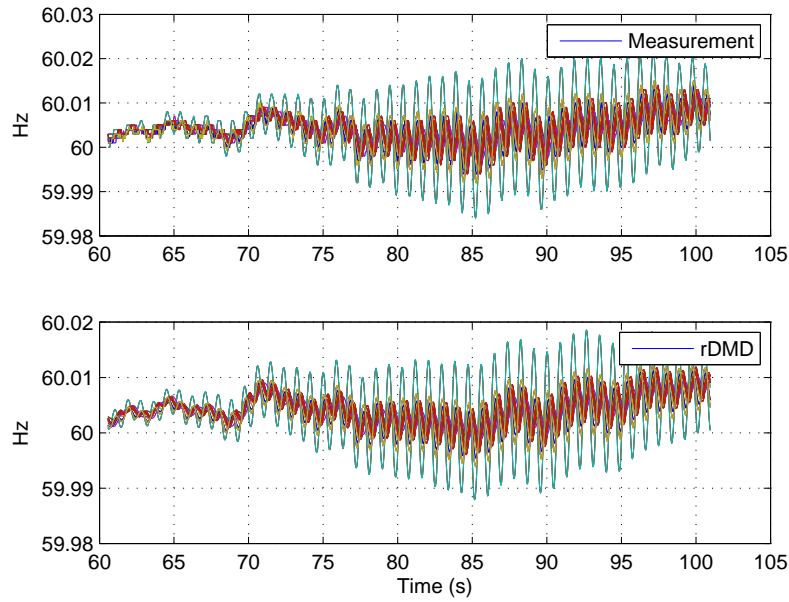
(b)

Figure 3.19: Frequency signals reconstruction of event 1 and event 3. (a) Event 1 frequency measurement and reconstructed signals. Rank is assumed as 16. Data stacking number is 350. (b) Event 3 frequency measurement and reconstructed signals. Rank is assumed as 20 and data stacking number is 550.
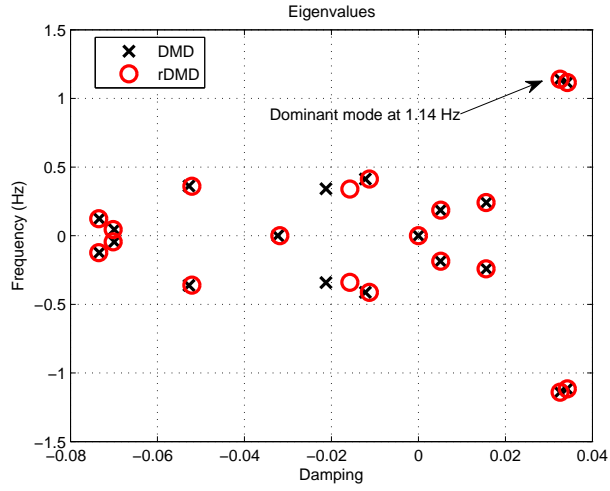
Figure 3.20: Identified eigenvalues of event 3.

(a)

(b)
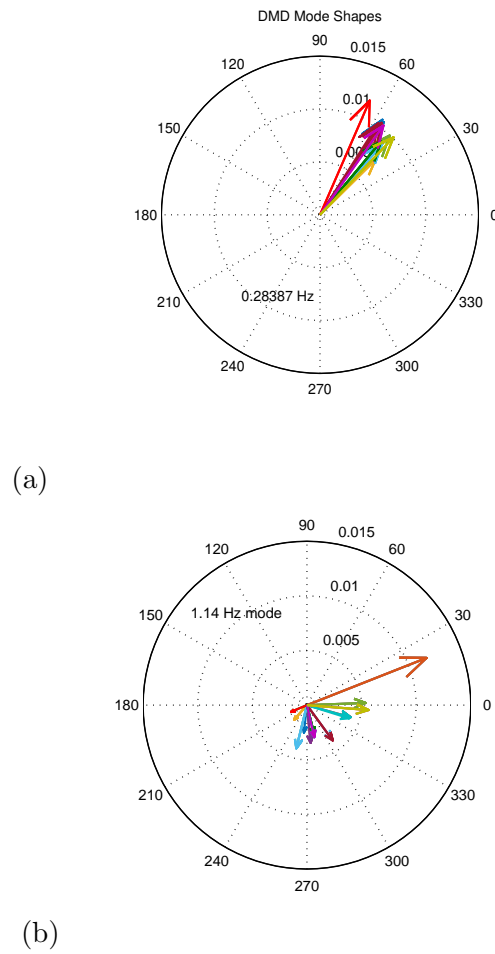
Figure 3.21: Mode shapes of event 1 and 3. (a) Event 1 0.28 Hz mode's mode shape. (b) Event 3 1.14 Hz mode's mode shape.

54

Chapter 4: Gray-Box Modeling for Synchronous Generators and Inverters

4.1 Introduction

Synchronous generators and inverter-based resources (IBRs) are the main energy resources in the power grid. Governing the grid control structures leans on the system parameters, which are exposed to variation for different reasons such as aging and events. In the current industrial practice, generic dynamic models with assumed model structures are used for dynamic assessment, e.g., [32, 33]. Due to the fact that most power system applications rely on model-based analysis, parameter estimation plays a critical role to minimize the discrepancy between the simulation and reality. How to fit the model parameters using field measurement data is of practical importance. The goal of this chapter is to design a method to come up with the model parameters based on time-domain measurement data.

Parameter estimation ameliorates the performance of diverse power system applications as it reliably helps interpret the dynamical behavior. The system aggregated load can be estimated [34]. The internal synchronous generator components can be approached [35],[36]. Reference [37] proposes a technique that utilizes the system mode to estimate the system inertia using least-squares. The method is improved in [38] by including the mode shapes with the system modes to estimate the system damping with the system inertia. The latter method is sensitive in estimating the system damping. With the Unscented and Extended Kalman Filters, the authors of [39] are able to estimate direct axis transient reactance, quadrature axis voltage, and generator inertia. Reference [40] provides two models to identify the parameters of the dynamic synchronous generator using autoregression exogenous (ARX)-based least squares estimation (LSE). The first model identifies the system while taking the frequency as input and the power as output. In the second model, with the as-

sumption of a single machine infinite bus system, the parameters are identified considering the measurements as output.

The application scope of this research is two-fold. First, we model a single-machine infinite-bus to identify the inertia, damping and synchronizing torque coefficients. Second, we parameterize a reduced-order grid-integrated IBR model to identify five parameters that are of paramount importance to the inverter control structure.

Estimating dynamic model parameters for a model with a known structure is termed gray-box model identification and the most popular method is PEM [41]. For a given model structure, gray-box model identification leads to unknown parameters relying on measurement data. Although the prior knowledge of gray-box is more than black-box, solving gray-box is less reliable. This is due to the nonconvexity that is caused by the inherited bilinearity in the gray-box. As a result, the global solution that leads to the exact parameter values is not guaranteed because it may settle at a local point. PEM directly uses the input-output time-domain data to identify the parameters[41]. While it acquires acceptable asymptotic accuracy, PEM requires a good initial guess of parameters that should be in the domain of convergence.

Another approach to handle gray-box is a two-step way: (i) conduct a black-box method (such as MOESP or N4SID) to identify the system up to a similarity transformation matrix, and (ii) solve an optimization problem that involves the parametrized structure and the similarity transformation matrix to find the unknown parameters. This procedure is also exposed to local solutions as the problem in the second step is nonlinear[42].

Recently, the system identification community has made significant progress in improving gray-box methodology. Reference [43] exploits the low-rank structure of the two-step approach to convert the bilinear problem to a rank constrained problem; then, the problem can be solved using difference-of-convex programming (DCP). In [44], PEM is reformulated as a rank constraint optimization problem with a matrix decision variable to be as close as the data Hankel matrix formed from the measurement data. The data Hankel matrix is
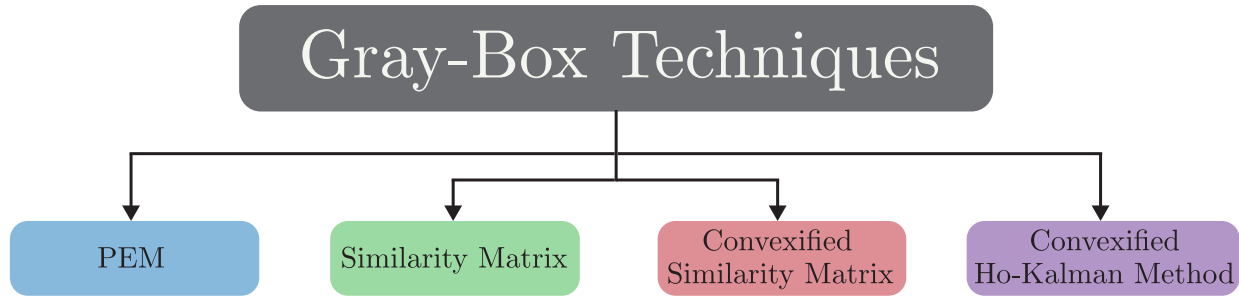
Figure 4.1: Dynamical model parameter estimation techniques.

low-rank and can be factorized into an observability matrix and a controllability matrix, as shown in the seminal paper by Ho and Kalman in 1966 [45]. This problem can be further formulated as a DCP problem with an objective function to minimize the nuclear norm of the matrix decision variable and the sum of its first n singular values (where n is the model order).

This chapter investigates four different gray-box methods that are shown in Fig. 4.1; two of the methods are classical and nonlinear, and the other two are state-of-the-art and convex. We formulate and apply the identification methods on the following case studies:

- A second-order dynamic model to represent a single-machine infinite-bus system. This case allows grid operators to find generator parameters through measurement data. We formulate the methods in a way to estimate the damping coefficient, the machine inertia, and the synchronizing torque coefficient. While the convex methods accurately identify the parameters, the nonlinear methods estimate the parameters with an error.

- A reduced-order grid-integrated IBR model: the methods are adopted to identify five parameters of the inverter control model. For the nonlinear methods, PEM has a small error, however, it is highly more accurate than the similarity matrix technique. All the convexified methods are more accurate than the nonlinear methods.

4.2 Dynamical Model Parameter Identification

A nth-order system with m input and p outputs, the continuous-time state-space model is expressed as follows.

$$\dot{x}(t) = Ax(t) + Bu(t),$$
$$y(t) = Cx(t) + Du(t), \tag{4.1}$$

where $A \in \mathbb{R}^{n \times n}$, $B \in \mathbb{R}^{n \times m}$, $C \in \mathbb{R}^{p \times n}$, and $D \in \mathbb{R}^{p \times m}$ are the dynamical system matrix, the input matrix, the output matrix, and the feedthrough matrix, respectively. In many engineering applications, adopting discrete-time state space is more practical for several reasons such as discrete measurement and efficient computation. The discrete-time state space is as follows.

$$x[k\Delta t + \Delta t] = A_d x[k\Delta t] + B_d u[k\Delta t],$$
$$y[k\Delta t] = C_d x[k\Delta t] + D_d u[k\Delta t], \tag{4.2}$$

where Δt is the sampling period and k is the sample number. Many methods accurately convert continuous-time state-space form to discrete-time state-space form [23, Chapter 2]. Among the numerical integration methods, Forward-Euler approximation is convenient in parameter identification because it retains the system original structure, as follows:

$$A_d = A\Delta t + I,$$
$$B_d = B\Delta t,$$
$$C_d = C, \tag{4.3}$$
$$D_d = D,$$

where I is the identity matrix. The conversion accuracy increases with decreasing the sampling period, Δt.

The system is constructed based on the physical mechanisms so that each parameter is related to a physical component. The model is built in an affine parameterized form to utilize

the prior knowledge of the system and to identify the missing parameters. The parameterized system structure can be set up as follows. Assume that the feedthrough matrix $D = 0$ and the system matrices are affine towards the parameter vector $\theta \in \mathbb{R}^l$.

$$
\begin{aligned}
A(\theta) &= A_0 + \sum_{i=1}^{l} A_i \theta_i, \\
B(\theta) &= B_0 + \sum_{i=1}^{l} B_i \theta_i, \\
C(\theta) &= C_0 + \sum_{i=1}^{l} C_i \theta_i,
\end{aligned}
\tag{4.4}
$$

where $\theta \in \mathbb{R}^l$ represents the unknown system parameters. Herein, we present two classical nonlinear identification ways that are Prediction Error Method and Similarity Matrix Technique. In general, the solution accuracy of nonlinear algorithms is primarily based on the provided initial values. Reference [46] proposed in 2003 an initialization method that is based on convex sum-of-squares method. While this initialization method helps lead to global solution, it is still restricted to small-scale systems.

Afterward, in the following sections, we demonstrate two convexified methods.

4.2.1 Prediction Error Method (PEM)

It utilizes the system input and output data for identifying its parameters. With N number of system measurements, the method is realized by solving the following optimization problem:

$$
\begin{aligned}
\min_{\theta} \quad & \frac{1}{N} \sum_{k=0}^{N-1} \| y(k\Delta t) - \hat{y}(k\Delta t | \theta) \|^2 \\
\text{s.t.} \quad & \hat{x}(k\Delta t + \Delta t) = A_d(\theta)\hat{x}(k\Delta t) + B_d(\theta)u(k\Delta t), \\
& \hat{y}(k\Delta t | \theta) = C_d(\theta)\hat{x}(k\Delta t), \quad \text{for } k = 0, \dots, N-1,
\end{aligned}
\tag{4.5}
$$

where $\hat{x}$ and $\hat{y}$ refer to the estimated state and output measurement, respectively. PEM can be approached using classical techniques such as the Gauss–Newton method [41] and the gradient projection method [47].

4.2.2 The Similarity Matrix Technique

This technique reaches the system parameters in two steps: implementing black-box on the system and utilizing prior knowledge of the system.

4.2.2.1 Implementing Black-Box

Black-box identification is mature and has many methods in the literature such as Multivariable Output Error State sPace (MOESP)[47], Eigensystem Realization Algorithm (ERA)[8], and Numerical algorithm For Subspace IDentification (N4SID) [41]. Black-box modeling can accurately identify the system characteristics. However, because the system is identified up to the similarity transformation matrix, the system parameters cannot be determined. With considering the similarity transformation matrix T in the system, equation (4.2) becomes as follows

$$\tilde{x}[k+1] = \underbrace{T^{-1}AT}_{\hat{A}}\tilde{x}[k] + \underbrace{T^{-1}B}_{\hat{B}}u[k],$$
$$y[k] = \underbrace{CT}_{\hat{C}}\tilde{x}[k],$$

(4.6)

where $\hat{A}$, $\hat{B}$ and $\hat{C}$ represent the state space of the estimated system from a black-box method.

4.2.2.2 Utilizing Prior Knowledge

After identifying the system using any of the input-output black-box methods, the user constructs the relationship of the estimated the parameterized matrices:

$$T\hat{A} = A(\theta)T,$$
$$T\hat{B} = B(\theta),$$
$$\hat{C} = C(\theta)T.$$

(4.7)

The unknown parameters θ and similarity transformation matrix T can be estimated by solving the following least-squares problem

$$\min_{\theta,T} \quad \|T\hat{A} - A(\theta)T\|_F^2 + \|T\hat{B} - B(\theta)\|_F^2 + \|\hat{C} - C(\theta)T\|_F^2, \tag{4.8}$$

where $\|\cdot\|_F^2$ is the Frobenius norm. This problem is nonlinear because of the multiplication between parametrized matrices and the similarity matrix. In the following sections, we provide two techniques that convexify this problem so that the user has a higher chance to attain the global solution.

4.3 The Convexified Similarity Matrix Technique

As the similarity matrix technique is bilinear, it has many local solution points. The actual system parameters are only achieved by realizing the global solution point. Reference [43] convexifies the similarity matrix technique problem to ensure reaching the global point. This chapter adopts the same methodology to examine its ability and to compare it with other methods.

4.3.1 Problem Formulation

The convexification procedure aims to attain the unknown parameters θ and the similarity matrix T. By means of the Kronecker product $\otimes$ and the vectorization operator $\mathrm{vec}(\cdot)$, equation (4.7) can be reshaped as following

$$\underbrace{\begin{bmatrix} \hat{A}^T \otimes I - I \otimes A(\theta) \\ \hat{B}^T \otimes I \\ I \otimes C(\theta) \end{bmatrix}}_{M(\theta)} \mathrm{vec}(T) = \underbrace{\begin{bmatrix} 0 \\ \mathrm{vec}(B(\theta)) \\ \mathrm{vec}(\hat{C}) \end{bmatrix}}_{N(\theta)}, \tag{4.9}$$

where $M(\theta) \in \mathbb{R}^{(n^2+mn+pn) \times n^2}$ and $N(\theta) \in \mathbb{R}^{(n^2+mn+pn)}$. $M(\theta)$ and $N(\theta)$ inherit the affinity of the unknown variables θ from the parameterized structure $A(\theta), B(\theta)$ and $C(\theta)$. Therefore, they can be expressed as follows

$$
\begin{aligned}
M(\theta) &= M_0 + M_1\theta_1 + \cdots + M_l\theta_l, \\
N(\theta) &= N_0 + N_1\theta_1 + \cdots + N_l\theta_l,
\end{aligned}
\tag{4.10}
$$

where $\{M_i\}_{i=0}^{l}$ and $\{N_i\}_{i=0}^{l}$ contain the coefficients of $M(\theta)$ and $N(\theta)$. With $\tau = \mathrm{vec}(T)$ and the affine form in equation (4.10), equation (4.9) becomes:

$$
M_0\tau + M_1\tau\theta_1 + \cdots + M_l\tau\theta_l = N_0 + N_1\theta_1 + \cdots + N_l\theta_l,
\tag{4.11}
$$

It can be seen that the problem is still bilinear — due to the multiplication of θ and τ. This issue can be circumvented by involving an auxiliary variable as following

$$
\begin{aligned}
\vartheta_1 &= \tau\theta_1 \\
&\;\;\vdots \\
\vartheta_l &= \tau\theta_l
\end{aligned}
\tag{4.12}
$$

where $\vartheta_i \in \mathbb{R}^{n^2}$ for $i = 1, \cdots, l$. Consequently, we have:

$$
M_0\tau + M_1\vartheta_1 + \cdots + M_l\vartheta_l = N_0 + N_1\theta_1 + \cdots + N_l\theta_l,
\tag{4.13}
$$

where $\{\vartheta_i\}_{i=0}^{l}$ and $\{\theta_i\}_{i=0}^{l}$ are the problem variables. Although the equation is transformed into linear form, it is under-determined as it incorporates more variables than equations. The under-determinedness is handled by making use of the unknown variable relation, in equation (4.12). The two variable sets construct a rank one matrix:

$$
H(\vartheta, \theta) = \begin{bmatrix} \tau & \vartheta_1 & \cdots & \vartheta_l \\ 1 & \theta_1 & \cdots & \theta_l \end{bmatrix}
\tag{4.14}
$$

where $\vartheta = \begin{bmatrix} \vartheta_0 & \cdots & \vartheta_l \end{bmatrix} \in \mathbb{R}^{n^2 \times l}$. As a result, the problem is solved with respect to the rank constraint, $\text{rank}[H(\vartheta, \theta)] = 1$. Thus, applying Singular Value Decomposition (SVD) on $H(\vartheta, \theta)$ leads to $\text{svd}[H(\vartheta, \theta)] = uv^T$, where $u \in \mathbb{R}^{n^2+1}$ and $v \in \mathbb{R}^{l+1}$. Correspondingly, the unknown variables in equation (4.11) are achieved by solving the following estimation problem

$$\min_{\vartheta, \theta} \quad \| \sum_{i=0}^{l} M_i \vartheta_i - N_0 - \sum_{i=1}^{l} N_i \theta_i \|_2^2$$
$$\text{s.t.} \quad \text{rank}[H(\vartheta, \theta)] = 1. \tag{4.15}$$

While solving the above optimization problem leads to the global solution that reflects the exact unknown parameters, the rank constraint computationally hinders the solving process. To efficiently solve the problem, the following subsection transforms the problem into the difference of convex programming form.

4.3.2 Difference of Convex Programming

The rank-constraint optimization problem, equation (4.15), is converted to a nuclear norm regularized optimization problem as follows

$$\min_{\vartheta, \theta} \quad \| \sum_{i=0}^{l} M_i \vartheta_i - N_0 - \sum_{i=1}^{l} N_i \theta_i \|_2^2 + \lambda \| H(\vartheta, \theta) \|_* \tag{4.16}$$

where $\| \cdot \|_*$ denotes the nuclear norm and λ is the regularization factor. Then, the nuclear truncation is implemented to replace the rank constraint:

$$\| H(\vartheta, \theta)) \|_* = f_n(H(\vartheta, \theta)) = \sum_{i=1}^{l+1} \sigma_i(H(\vartheta, \theta)), \tag{4.17}$$

where f_n is the sum of the largest n singular values, σ. Because the constraint is rank 1, the following relation can be deduced:

$$\sum_{i=2}^{l+1} \sigma_i(H(\vartheta, \theta)) = f_{l+1}(H(\vartheta, \theta)) - f_1(H(\vartheta, \theta)) = 0, \qquad (4.18)$$

where

$$f_{l+1}(H(\vartheta, \theta)) = \|H(\vartheta, \theta)\|_*,$$

$$f_1(H(\vartheta, \theta)) = \|H(\vartheta, \theta)\|_2.$$

Accordingly, the nuclear norm regularized optimization problem is equivalent to

$$\min_{\vartheta, \theta} \quad \|\sum_{i=0}^{l} M_i \vartheta_i - N_0 - \sum_{i=1}^{l} N_i \theta_i\|_2^2$$
$$+ \lambda(\|H(\vartheta, \theta)\|_* - \|H(\vartheta, \theta)\|_2). \qquad (4.19)$$

The above derivation mainly depends on the norms that are convex and can be approached using Difference of Convex Programming (DCP). The sequential convex programming method is efficient for solving a DCP problem, and it is adopted for this formulation. For every k iteration, $(\hat{\vartheta}^k, \hat{\theta}^k)$ is the estimated solution of the problem variables (ϑ, θ). $\hat{u}^k$ and $\hat{v}^k$ are respectively the left and right singular value vectors of the largest singular value of the matrix $H(\hat{\vartheta}^k, \hat{\theta}^k)$. Therefore, the convexified problem that estimates $(\hat{\vartheta}^{k+1}, \hat{\theta}^{k+1})$ is

$$\min_{\vartheta, \theta} \quad \|\sum_{i=0}^{l} M_i \vartheta_i - N_0 - \sum_{i=1}^{l} N_i \theta_i\|_2^2$$
$$+ \lambda(\|H(\vartheta, \theta)\|_* - (\hat{u}^k)^T H(\vartheta, \theta) \hat{v}^k). \qquad (4.20)$$

Iteratively solving the above problem has a higher chance to achieve the exact values of the unknown parameters. As the sequential convex programming method requires proper initialization to reach the global optimal solution, employing the solution of (4.16) as initialization most likely takes care of it.

4.4 Hankel Data Matrix-Based Gray-Box Model Identification

With the assumption that impulse response data are available, the gray-box model identification utilizes the low-rank property of the data Hankel matrix formed by impulse response data and formulates a rank constraint problem to be solved via DCP.

4.4.1 Problem Formulation

The algorithm aims to identify the model parameters by matching the measured impulse response with the impulse response of the parameterized model. The system impulse response measurements, also called Markov parameters, are equivalent to $M_i = C_d(A_d)^i B_d$ for $i = 0, 1, \ldots, R$, where R is the number of the total impulse samples.

The Markov parameters are aggregated in a block Hankel matrix:

$$
H_{v,h}^* =
\begin{bmatrix}
M_0 & M_1 & \cdots & M_{h-1} \\
M_1 & M_2 & \cdots & M_h \\
\vdots & \vdots & \ddots & \vdots \\
M_{v-1} & M_v & \cdots & M_{v+h-2}
\end{bmatrix},
\tag{4.21}
$$

where the subscripts v and h represent the number of block rows and columns, respectively. Each of them has to be greater than or equal to the system order, n. The parameterized system, which contains the unknown parameters, is also collected in a block Hankel matrix that matches the shape of the measurement Hankel matrix. Solving the following optimization

problem identifies the unknown parameters

$$\min_{\theta} \left\| H_{v,h}^* - H_{v,h}(\theta) \right\|_F^2$$

s.t.

$$H_{v,h}(\theta) =$$
$$\begin{bmatrix} C_d(\theta)B_d(\theta) & \cdots & C_d(\theta)A_d^{h-1}(\theta)B_d(\theta) \\ \vdots & \ddots & \vdots \\ C_d(\theta)A_d^{v-1}(\theta)B_d(\theta) & \cdots & C_d(\theta)A_d^{v+h-2}(\theta)B_d(\theta) \end{bmatrix}.$$
(4.22)

This is a nonlinear programming problem and it is difficult to find the global solution.

4.4.2 Rank-Constraint Reformulation

The matrix $H_{v,h}(\theta)$ is low-rank, and it can be factorized as follows

$$H_{v,h}(\theta) = \underbrace{\begin{bmatrix} C_d(\theta) \\ C_d(\theta)A_d(\theta) \\ \vdots \\ C_d(\theta)A_d^{v-1}(\theta) \end{bmatrix}}_{\mathcal{O}_v(\theta)}$$
$$\times \underbrace{\begin{bmatrix} B_d(\theta) & A_d(\theta)B_d(\theta) & \cdots & A_d^{h-1}(\theta)B_d(\theta) \end{bmatrix}}_{\mathcal{C}_h(\theta)},$$
(4.23)

where $\mathcal{O}_v(\theta)$ and $\mathcal{C}_h(\theta)$ are the extended observability and controllability matrices, respectively. To differentiate between the $H_{v,h}(\theta)$ original and low-rank structures, the low-rank structure is denoted as Γ so that $\Gamma = \mathcal{O}\mathcal{C}$. Next, two variable matrices are introduced to

represent the shift property of $\mathcal{O}_v(\theta)$ and $\mathcal{C}_h(\theta)$, respectively.

$$\overline{\mathcal{O}}_v(\theta) = \begin{bmatrix} \mathcal{O}_v(p+1:vp,:) \\ C_d(\theta)A_d^v(\theta) \end{bmatrix}, \tag{4.24}$$

$$\overline{\mathcal{C}}_h(\theta) = \begin{bmatrix} \mathcal{C}_h(:,m+1:hm) & A_d^h(\theta)B_d(\theta) \end{bmatrix}.$$

$\overline{\mathcal{O}}_v(\theta)$ and $\overline{\mathcal{C}}_h(\theta)$ respectively hold the relationship of $\overline{\mathcal{O}}_v(\theta) = \mathcal{O}_v(\theta)A_d(\theta)$ and $\overline{\mathcal{C}}_h(\theta) = A_d(\theta)\mathcal{C}_h(\theta)$. The bilinearity of these variables can now be transformed into a rank constraint. As a result, the following problem is formed in [44]:

$$\min_{\theta,\mathcal{O},\mathcal{C},\overline{\mathcal{O}},\overline{\mathcal{C}},\Gamma,\bar{A}} \quad \|H_{v,h}^* - \Gamma\|_F^2$$

$$\text{s.t.} \quad \text{rank} \underbrace{\begin{bmatrix} \Gamma & \mathcal{O} & \overline{\mathcal{O}} \\ \mathcal{C} & I_n & A_d(\theta) \\ \overline{\mathcal{C}} & A_d(\theta) & \bar{A} \end{bmatrix}}_{Z} = n,$$

$$\tag{4.25}$$

$$\mathcal{O}(1:p,:) = C_d(\theta),$$
$$\overline{\mathcal{O}}(1:(v-1)p,:) = \mathcal{O}(p+1:vp,:),$$
$$\mathcal{C}(:,1:m) = B_d(\theta),$$
$$\overline{\mathcal{C}}(:,1:(h-1)m) = \mathcal{C}(:,m+1:hm),$$

where $\bar{A} = A_d^2(\theta)$. This rank-constraint problem will be solved by difference of convex programming in the following subsection.

4.4.3 Difference of Convex Programming

The truncated nuclear norm method gives the ability to replace the rank constraint in (4.25) by the following

$$\|Z\|_* - f_n(Z) = 0, \tag{4.26}$$

where $\| \cdot \|_*$ is the nuclear norm and $f_n(Z) = \sum_{i=1}^n \sigma_i(Z)$. f_n is the sum of the largest n singular values, σ. The nuclear norm and $f_n(Z)$ are all convex in the minimization variables. Hence, it is a difference of convex programming (DCP) problem. It can be solved by sequence iteration.

At every jth iteration, the Singular Value Decomposition (SVD) is implemented on Z:

$$Z^j = \begin{bmatrix} U_1^j & U_2^j \end{bmatrix} \begin{bmatrix} S_1^j & \\ & S_2^j \end{bmatrix} \begin{bmatrix} V_1^{j,T} \\ V_2^{j,T} \end{bmatrix}, \tag{4.27}$$

where U_1^j and $V_1^{j,T}$ denote the n truncated left and right singular matrices, respectively.

$$\min_{\theta, \mathcal{O}, \mathcal{C}, \overline{\mathcal{O}}, \overline{\mathcal{C}}, \Gamma, \bar{A}, Z} \quad \| H_{v,h}^* - \Gamma \|_F^2 + \lambda \left(\| Z \|_* - \mathrm{tr} \left(U_1^{j,T} Z V_1^j \right) \right)$$

$$\text{s.t.} \quad Z = \begin{bmatrix} \Gamma & \mathcal{O} & \overline{\mathcal{O}} \\ \mathcal{C} & I_n & A_d(\theta) \\ \overline{\mathcal{C}} & A_d(\theta) & \bar{A} \end{bmatrix},$$

$$\mathcal{O}(1:p,:) = C_d(\theta),$$

$$\overline{\mathcal{O}}(1:(v-1)p,:) = \mathcal{O}(p+1:vp,:),$$

$$\mathcal{C}(:,1:m) = B_d(\theta),$$

$$\overline{\mathcal{C}}(:,1:(h-1)m) = \mathcal{C}(:,m+1:hm),$$

$$\tag{4.28}$$

where $\lambda > 0$ is a penalty parameter. (4.28) is a convex programming problem. Also, at the start of the iteration process, the n truncated left and right singular matrices are assumed as zero.

4.5 Case Studies

This section presents and discusses the implementation of the gray-box algorithms on a SMIB model and an analytical model of grid-integrated IBR. For each algorithm, the accu-

racy of the K estimated parameters $\hat{\theta}$ with respect to the actual parameters θ^* is evaluated using the normalized root-mean-square errors (NRMSE):

$$\text{NRMSE} = \sqrt{\frac{1}{K}\sum_{i=1}^{K}\left(\frac{\hat{\theta}_i - \theta_i^*}{\theta_i^*}\right)^2}. \tag{4.29}$$

The simulation is computed in MATLAB using: YALMIP [48] with fmincon and IPOPT [49] solvers for nonlinear problems and CVX [50] with SDPT3 solver for convex problems. For convex case studies, the penalty parameter is set to 0.001 and increases 5% in every step that has the regularized (penalty) term of the objective function greater than 0.001.

4.5.1 Single-Machine Infinite-Bus (SMIB)

SMIB analysis is mandatory before commissioning to validate the manufactured parameters and to determine the stability critical time. The system is shown in Fig. 4.2, and its state-space model is following.

$$\begin{bmatrix} \Delta\dot{\delta} \\ \Delta\dot{\omega} \end{bmatrix} = \underbrace{\begin{bmatrix} 0 & 1 \\ -\frac{K_s\omega_o}{2H} & -\frac{D}{2H} \end{bmatrix}}_{A} \begin{bmatrix} \Delta\delta \\ \Delta\omega \end{bmatrix} + \underbrace{\begin{bmatrix} 0 \\ \frac{\omega_o}{2H} \end{bmatrix}}_{B} \Delta T_{\text{m}}, \tag{4.30}$$

where

$$K_{\text{s}} = \frac{V_T V_\infty \cos\delta}{X_{eq}}. \tag{4.31}$$

$\Delta\delta$ and $\Delta\omega$ are the deviations of the generator rotor angle in rad and speed in rad/s, respectively. The system nominal angular frequency is $\omega_o = 2\pi f$, where f is the system frequency (60 Hz). ΔT_{m} is the mechanical torque, and D is the damping coefficient that is set to 1. The machine inertia H is 3.5 sec. The equivalent system reactance is $X_{eq} = X_d' + X_T + X_L = 0.1033$ pu. K_{s} is the synchronizing torque coefficient, and it is computed at its equilibrium to be 0.7819. For more details please refer to[51].
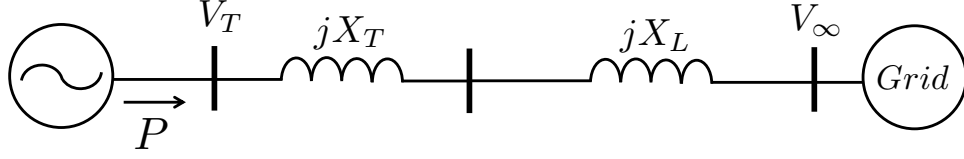
Figure 4.2: Single-machine infinite-bus system.

4.5.1.1   Model Identification

The following parameterization structure is designed to identify D, H, and K_s.

$$\begin{bmatrix} \Delta\dot\delta \\ \Delta\dot\omega \end{bmatrix} = \underbrace{\begin{bmatrix} 0 & 1 \\ \theta_1 & \theta_2 \end{bmatrix}}_{A} \begin{bmatrix} \Delta\delta \\ \Delta\omega \end{bmatrix} + \underbrace{\begin{bmatrix} 0 \\ \theta_3 \end{bmatrix}}_{B} \Delta T_\mathrm{m}. \tag{4.32}$$

where

$$\theta_1 = -\frac{K_\mathrm{s}\omega_\mathrm{o}}{2H},$$
$$\theta_2 = -\frac{D}{2H},$$
$$\theta_3 = \frac{\omega_\mathrm{o}}{2H}.$$

For comparison, all the following methods adopt this identification structure.

- Prediction Error Method (PEM)

We use input-output measurements of the *step* response; the data samples are 1200 with sampling time of 0.001, as shown Fig. 4.3. Both fmincon and IPOPT can solve this specific problem and lead to the same solution that is shown in Table 4.1; however, they are incomparable considering computation time where fmincon solves it in $1,732.4$ s and IPOPT solves it in 9.4358 s. The variable identification error is shown in Fig. 4.4. As expected, θ_2 has the highest error as its value is low. The NRMSE of this case is presented in Fig. 4.5. Using the identified parameters, the system signals are reconstructed and compared with

the original signals to examine the identification accuracy; Fig. 4.6 shows the step response reconstructed from the identified parameters matches the original step response.
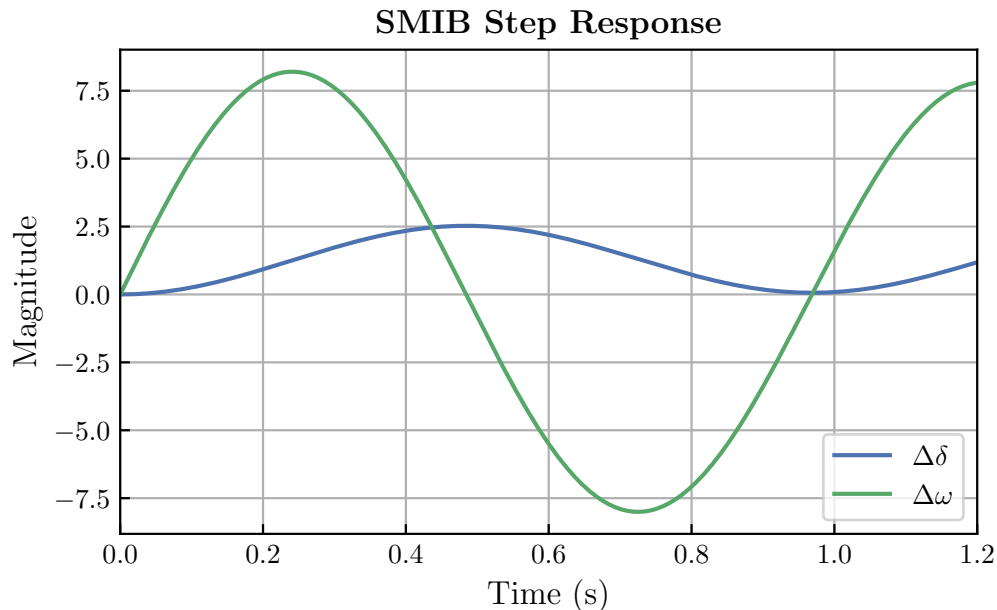
Figure 4.3: SMIB case: step response data that are used for PEM learning.

- Similarity Matrix Technique (SM)

As mentioned earlier, this technique and its convexified version are primarily based on black-box identification. In this research, we use the following estimated system that is obtained from MOESP:

$$\hat{\mathbf{A}} = \begin{bmatrix} 0.0206 & 16.7432 \\ -2.5153 & -0.1635 \end{bmatrix}$$

$$\hat{\mathbf{B}} = \begin{bmatrix} -11.1819 \\ 0.3090 \end{bmatrix} \tag{4.33}$$

$$\hat{\mathbf{C}} = \begin{bmatrix} 0.0528 & 1.9096 \\ -4.8021 & 0.5711 \end{bmatrix}$$

One of the ways to examine the estimated black-box model accuracy is to inspect its eigenvalues; they have to match the original system. Using the above-estimated model, solving

(4.8) obtains the unknown variables as well as the similarity transformation matrix. This optimization problem is highly nonlinear, and solving it is extremely sensitive to the initializations. IPOPT solver is efficient, however, surprisingly, it cannot solve this problem. Without generalization, only fmincon could solve it with a computation time of 2.2057 s. The system signals are reconstructed in Fig. 4.6; they show acceptable matching. The identification error is shown in Fig. 4.4, and θ_3 has the highest error. Fig. 4.5 shows the NRMSE, and the similarity matrix technique has the highest error because the solution settles on a local point. For this case, we set the initial values 10% around the actual values. The user might not have or reach this initialization value. For that, this identification method is not reliable to singly stand alone.

- Convex Similarity Matrix Technique (cSM)

The process of this method is conducted with the above-estimated model, (4.33). The matrices M and N are sparse with the size of (10×4) and (10×1), respectively. Since we seek to identify 3 unknown parameters for this problem, we construct 4 sets of M and N; one contains the known parts of the systems, and the rest of the sets are constructed with respect to each unknown parameter, as in (4.10):

$$
M_0 =
\begin{bmatrix}
0.0206 & -1.0000 & -2.5153 & 0 \\
0 & 0.0206 & 0 & -2.5153 \\
16.7432 & 0 & -0.1635 & -1.0000 \\
0 & 16.7432 & 0 & -0.1635 \\
-11.1819 & 0 & 0.3090 & 0 \\
0 & -11.1819 & 0 & 0.3090 \\
1.0000 & 0 & 0 & 0 \\
0 & 1.0000 & 0 & 0 \\
0 & 0 & 1.0000 & 0 \\
0 & 0 & 0 & 1.0000
\end{bmatrix},
$$

$$M_1(2, 1) = M_1(4, 3) = 1,$$

$$M_2(2, 2) = M_2(4, 4) = 1,$$

all the entries of M_3 are zero because the third identified variable only belongs to $B(\theta)$. The N matrices are defined as

$$N_0 = \begin{bmatrix} 0 \\ 0 \\ 0 \\ 0 \\ 0 \\ 0 \\ 0.0528 \\ -4.8021 \\ 1.9096 \\ 0.5711 \end{bmatrix},$$

$$N_3(6, 1) = 1,$$

because the first and second identified variables are unrelated to $B(\theta)$, N_1 and N_2 are zero vectors.

The presented solution is achieved within 83 iterations in 0.6719 s. The detailed iteration solution is shown in Fig. 4.8: the top plot demonstrates the behavior of the objective function without regularization, the middle plot shows the regularization part of the objective function decreases in each iteration, and the bottom plot presents the convergence of the parameters in each iteration. Fig. 4.4 reveals that the parameter error is negligible, accordingly, the NRMSE in Fig. 4.5 validates that the total error of all the unknown parameters is less than 0.01. Indeed, reconstructing the signals in Fig. 4.6 presents perfect matching.

- Convex Ho-Kalman method (cHK)

We use the impulse response that is shown in Fig. 4.9. With setting the sampling time to 0.01 s, the total number of samples is 100. The Hankel matrix is built with block rows and columns of $v = 10$ and $h = 90$, respectively. The solution of this algorithm is obtained in 9 iterations and 10.2031 s. The detailed iteration solution is presented in Fig. 4.10. The objective function without regularization is shown in the top plot, the regularization part of the objective function is shown in the middle plot, the convergence of the parameters is shown in the bottom plot. The solution identifies the parameters without error.
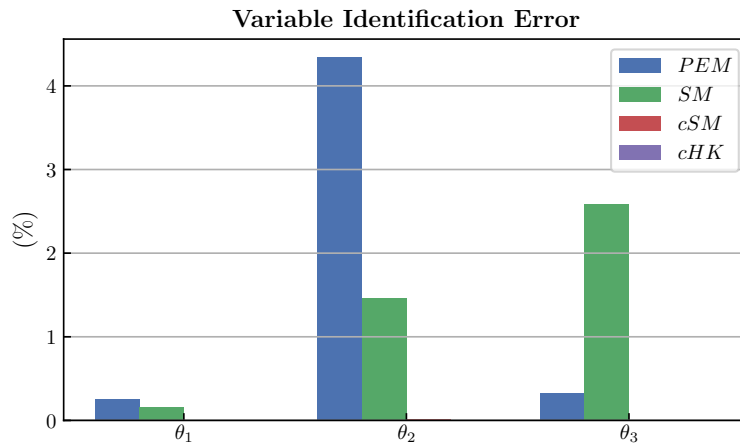
Figure 4.4: SMIB case: percentage error of each identified parameter.
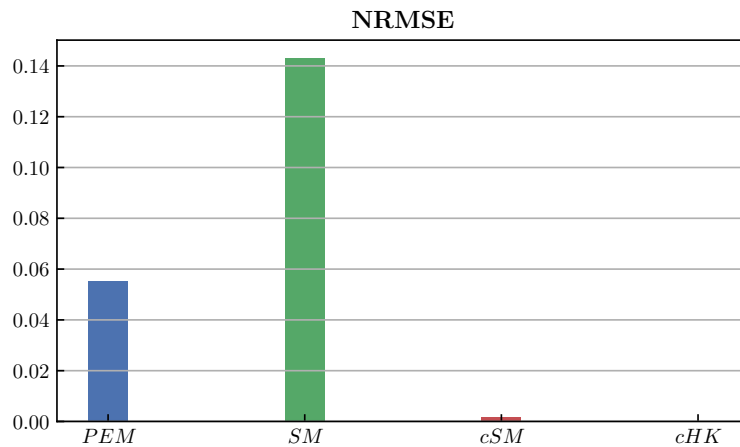
Figure 4.5: SMIB case: NRMSE.
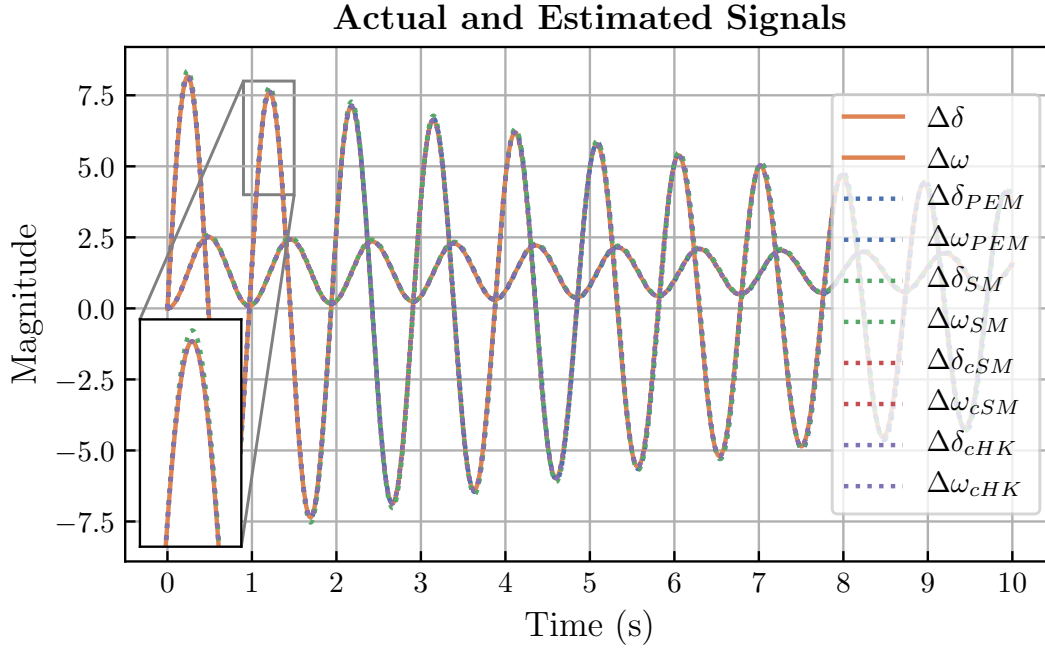
Figure 4.6: SMIB case: comparing the identified signals with the original.
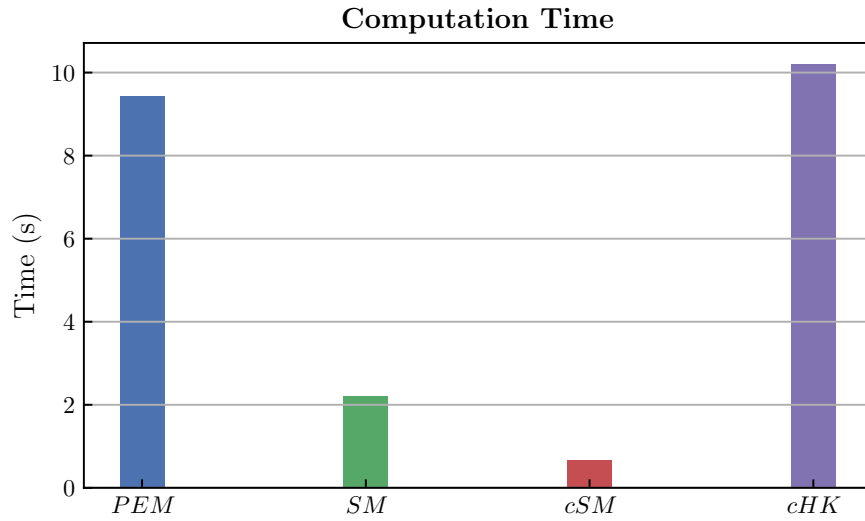
Figure 4.7: SMIB case: the computation time of each method.

Table 4.1: SMIB parameters.

Parameter	Actual	PEM	SM	cSM	cHK
θ_1	-42.1109	-42.0017	-42.043	-42.1108	-42.1109
θ_2	-0.1429	-0.1367	-0.145	-0.1429	-0.1429
θ_3	53.8733	53.6963	55.27	53.8731	53.8733
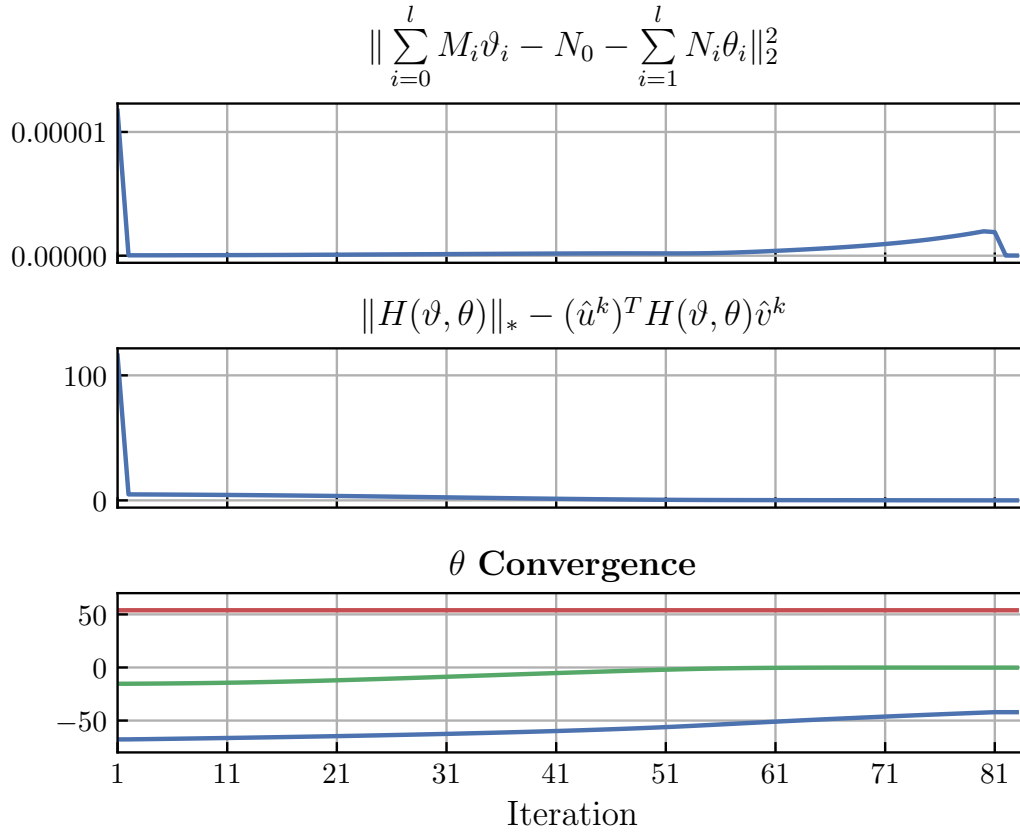
Figure 4.8: SMIB case: cSM iteration solution.
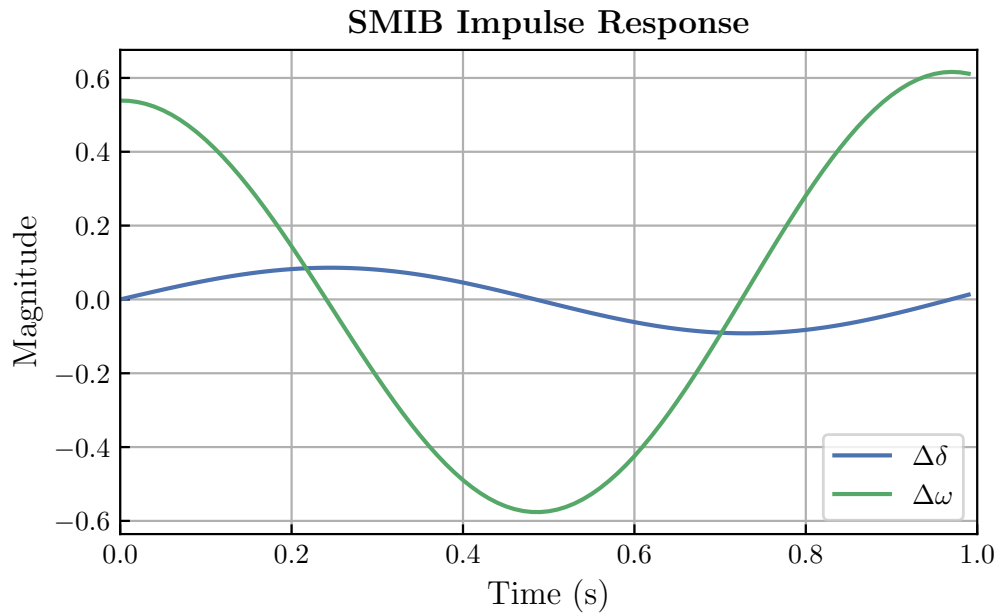
Figure 4.9: SMIB case: impulse response.
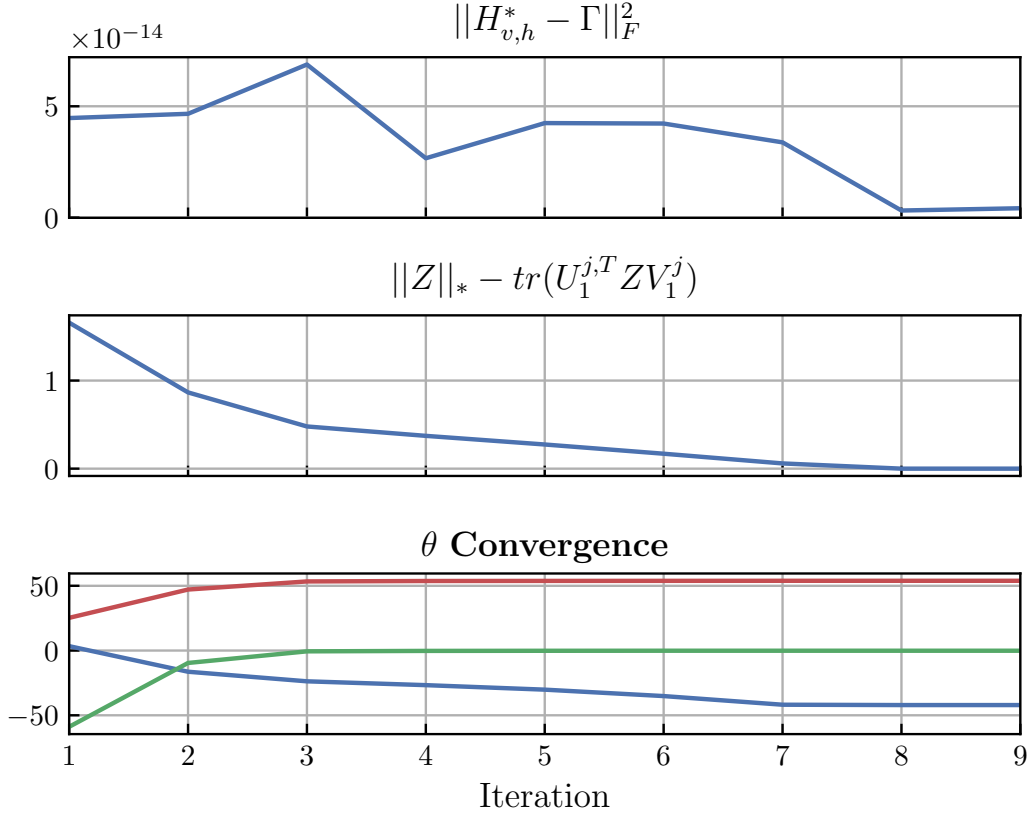
Figure 4.10: SMIB case: cHK iteration solution.

4.5.2 A Grid-integrated IBR

High penetration of wind generation exposes the system to voltage oscillation as well as temporary overvoltage. The impact of this phenomenon primarily pertains to the system strength, which is assessed based on the system Short Circuit Ratio (SCR). Thus, a system with low SCR is weak because of its vulnerability to voltage variation. The reduced-order analytical model to represent a grid-integrated IBR is from [52], which can offer an explanation of the low-frequency oscillations observed in a real-world wind power plant (WPP) in Texas[53]. In this case study, we adapt the analytical model from [52] into a parameterized structure and identify five parameters.

The analyzed system is a WPP connected to a grid through a transformer and a transmission shown Fig. 4.11. The grid is represented with constant voltage magnitude and angle. The line is assumed to be purely induction and the line reactance is notated as X. The point of common coupling (PCC) represents the converter bus that connects the WPP to the grid, where $\bar{V}$, P, and Q are the converter voltage magnitude, active power, and reactive power, respectively.
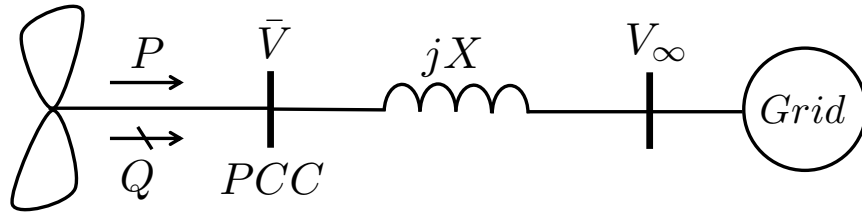
Figure 4.11: A wind power plant is connected to the grid.

The WPP is treated as a current source. The vector control technique is implemented on the WPP with its d-axis aligned with the PCC voltage space vector. The WPP output current, i_d and i_q, can be controlled by two cascaded loops, namely, outer and inner. The outer loops: one tracks the real power to generate the d-axis current reference i_d^*, and the other tracks the PCC voltage to generate the q-axis current reference i_q^*. The inner current loops track the references from the outer loops to set the converter output dq-voltages, V_{td} and V_{tq}.

The converter's inner current control is simplified by a first-order system with a time constant τ that takes the reference currents as inputs. The outputs are the dq-axic currents: i_d and i_q.

Since the converter voltage is aligned with the PCC voltage, hence $v_d = V$ and $v_q = 0$. The system's circuit relationship can be expressed as follows in the dq-frame:

$$v_d + jv_q = (jX)\,(i_d + ji_q) + \bar{V}_\infty. \tag{4.34}$$

Due to the fact that the active power flows from a higher angle to a lower one, the PCC angle, δ, is set to be leading the grid's angle. Consequently, the system KVL can be further decomposed as follows

$$
\begin{aligned}
v_d &= -Xi_q + V_\infty \cos \delta, \\
v_q &= 0 = +Xi_d - V_\infty \sin \delta.
\end{aligned}
\tag{4.35}
$$

Relying on the following trigonometric relationship

$$
V_\infty \cos \delta = \sqrt{V_\infty^2 - (V_\infty \sin \delta)^2},
\tag{4.36}
$$

equation (4.36) can be plugged in equation (4.35) to have

$$
v_d = -Xi_q + \sqrt{V_\infty^2 - (Xi_d)^2}.
\tag{4.37}
$$

The linearization of (4.37) gives the following:

$$
\Delta V = \Delta v_d = -X\Delta i_q - \underbrace{\frac{X}{\sqrt{\left(\dfrac{V_\infty}{Xi_d}\right)^2 - 1}}}_{c}\Delta i_d.
\tag{4.38}
$$

The active power feeding the grid from the PCC, and its linearized expression is:

$$
\begin{aligned}
P &= Vi_d, \\
\Delta P &= i_d\Delta V + V\Delta i_d.
\end{aligned}
\tag{4.39}
$$

The analytical model is presented in Fig. 4.12.
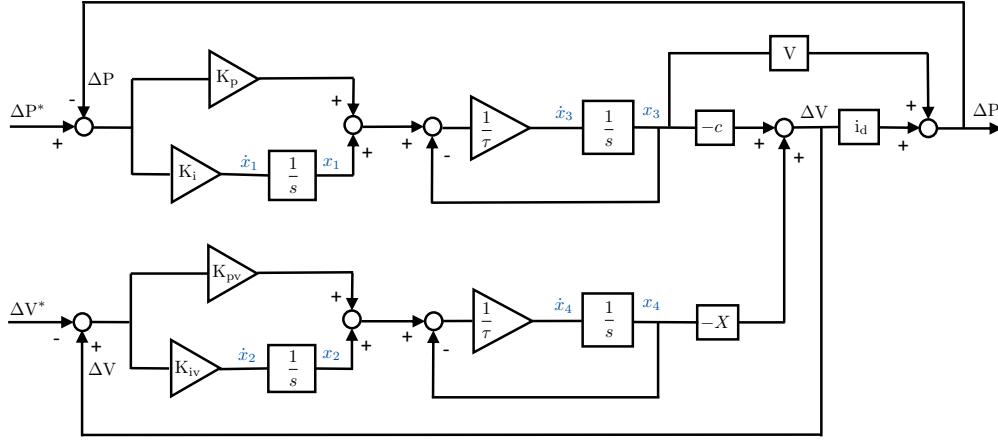
Figure 4.12: The WPP linearized analytical model. The model parameter values are $\tau = 0.05, X = 1, i_d = 0.955, K_p = 1, K_i = 1, K_{pv} = 1, K_{iv} = 10, i_{sc} = 1/X, V_d = 1$, and $V_\infty = 1$.

4.5.2.2 The Analytical Model State-Space

We derive the state-space form of the analytical model to make it compatible with the identification algorithms. The dynamical state of each integrator is indicated in Fig. 4.12. The state-space form is as follows.

$$
\begin{bmatrix} \dot{x}_1 \\ \dot{x}_2 \\ \dot{x}_3 \\ \dot{x}_4 \end{bmatrix} = \underbrace{\begin{bmatrix} 0 & 0 & -K_i\,(V_d - c\,i_d) & K_i\,X\,i_d \\ 0 & 0 & -K_{iv}\,c & -K_{iv}\,X \\ \frac{1}{\tau} & 0 & -\frac{K_p\,(V_d - c\,i_d) + 1}{\tau} & \frac{K_p\,X\,i_d}{\tau} \\ 0 & \frac{1}{\tau} & -\frac{K_{pv}\,c}{\tau} & -\frac{K_{pv}\,X + 1}{\tau} \end{bmatrix}}_{A} \begin{bmatrix} x_1 \\ x_2 \\ x_3 \\ x_4 \end{bmatrix} + \underbrace{\begin{bmatrix} K_i & 0 \\ 0 & -K_{iv} \\ \frac{K_p}{\tau} & 0 \\ 0 & -\frac{K_{pv}}{\tau} \end{bmatrix}}_{B} \begin{bmatrix} \Delta P^* \\ \Delta V^* \end{bmatrix}.
$$

$$(4.40)$$

From the above derivation, $(x_1 + K_p(\Delta P^* - \Delta P))$ and $(x_2 + K_{pv}(-\Delta V^* + \Delta V))$ are respectively Δi_d^* and Δi_q^*. These are *dq* reference current components that are generated by the outer loops. x_3 and x_4 are Δi_d and Δi_q, respectively.

4.5.2.3 Model Identification

In this case study, we aim to find five parameters: the time constant, τ, and the controller gains, K_p, K_i, K_{pv}, and K_{iv}. We parameterize the system as follows:

$$\mathbf{A}(\theta) = \begin{bmatrix} 0 & 0 & 2.07\theta_2 & 0.955\theta_2 \\ 0 & 0 & -3.22\theta_3 & -\theta_3 \\ \theta_1 & 0 & 2.07\theta_4 - \theta_1 & 0.955\theta_4 \\ 0 & \theta_1 & -3.22\theta_5 & -(\theta_5 + \theta_1) \end{bmatrix},$$

$$\mathbf{B}(\theta) = \begin{bmatrix} \theta_2 & 0 \\ 0 & -\theta_3 \\ \theta_4 & 0 \\ 0 & -\theta_5 \end{bmatrix}.$$

(4.41)

where

$$\theta_1 = \frac{1}{\tau}, \ \theta_2 = K_i, \ \theta_3 = K_{iv}$$
$$\theta_4 = \frac{K_p}{\tau}, \ \theta_5 = \frac{K_{pv}}{\tau}$$

All the following methods employ this identification structure.

- Prediction Error Method (PEM)

This method can identify the parameters using 800 samples of the input-output measurements with a sampling time of 0.001 s. With step response, the system output measurements, used for this method, are shown in Fig. 4.13. Both IPOPT and fmincon solvers are able to solve this problem during 3.3098 s and 2.7936 s, respectively. The NRMSE value of IPOPT and fmincon are respectively 0.0924 and 0.2076. Since IPOPT gives a more accurate solution, we advocate this method. The identified parameters are presented in Table. 4.2, each parameter is identified with an error that is less than 2%. The signals of the identified system match the original as shown Fig. 4.15.

- Similarity Matrix Technique (SM)
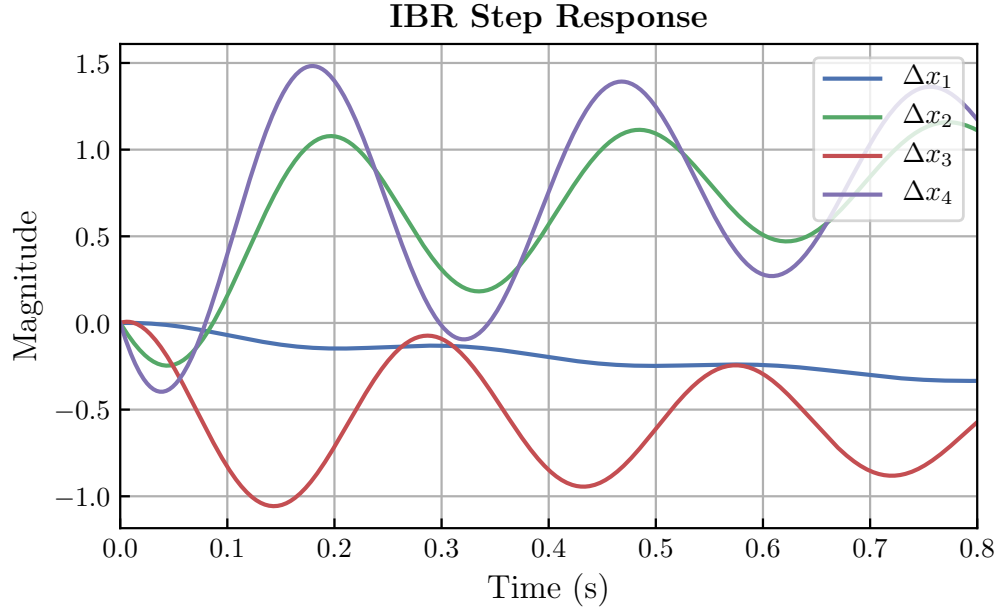
Figure 4.13: PV-mode IBR case: step response data that are used for PEM learning.

With the help of MOESP, the following estimated model is used for SM and cSM.

$$
\hat{\mathbf{A}} = \begin{bmatrix} -0.2425 & 29.4277 & 19.2790 & 7.7312 \\ -10.8380 & -0.3868 & 13.2615 & -1.6242 \\ -4.2309 & -7.9152 & -4.4144 & -8.2186 \\ -1.7001 & -1.3392 & -7.1351 & -13.4590 \end{bmatrix},
$$

$$
\hat{\mathbf{B}} = \begin{bmatrix} -10.6536 \\ 4.6308 \\ 8.3075 \\ 7.4087 \end{bmatrix}, \tag{4.42}
$$

$$
\hat{\mathbf{C}} = \begin{bmatrix} -0.1737 & 0.1594 & -0.4780 & 0.2000 \\ 0.8714 & -0.6566 & 0.1363 & 0.1609 \\ -0.5752 & -0.6914 & -0.0530 & -0.0656 \\ 1.2464 & -0.2343 & -0.4637 & -0.2407 \end{bmatrix}.
$$

The solution of this method is obtained using fmincon solver in 3.1796 s. IPOPT solver is not able to solve it. SM technique has a high error percentage for all the variables comparing to the other techniques as presented in Table. 4.2. The error of θ_2 is unacceptably high that reached around 150%. Even though we use initialization that differs from the actual parameters only 10%, this method has the highest NRMSE as shown in Fig. 4.14. From this, it can be concluded that initialization using the Sum of Square convexification technique as proposed in [54] does not guarantee the optimal solution for this problem. The identified system failed to reconstruct the signal as shown Fig. 4.15.

- Convex Similarity Matrix Technique (cSM)

The size of the matrices M and N are (36×16) and (36×1), respectively. We construct 6 sets of M and N to identify the 5 unknown parameters. The solution is reached within 52 iterations during 0.8438 s. The detailed iteration process is shown in Fig. 4.16; the top plot presents the unregulated objective function, the middle plot shows the regularization component, and the bottom plot displays the convergence of the parameters. The parameters of this technique are shown in Table. 4.2. As a result, the NRMSE, Fig. 4.14, is also low and acceptable. The identified model can produce the original signals with high quality as shown in Fig. 4.15.

- Convex Ho-Kalman method (cHK)

With the assumption of the measuring accessibility of all the four states, we employ the impulse response that is shown in Fig. 4.17 for the identification process with the sampling time 0.003 s. Total 116 data points are used with the number of block rows and columns are respectively $v = 10$ and $h = 106$. The solution is reached in 43 iterations during 115.6250 s; the solution details are shown in Fig. 4.18. The unregularized objective function is shown in the top plot, the objective function penalty is shown in the middle plot, the convergence of the parameters is shown in the bottom plot. The parameter error and NRMSE are

extremely low as shown in Table. 4.2 and Fig. 4.14, respectively. The identified parameters can perfectly reconstruct the signal as shown Fig. 4.15.

Table 4.2: Wind power plant analytical model parameters.

Parameter	Actual	PEM	SM	cSM	cHK
θ_1	20	19.7658	21.1501	20.0046	20.0056
θ_2	1	1.0110	2.5096	1.0046	1.0020
θ_3	10	10.0621	10.4607	9.9732	9.9994
θ_4	20	19.8421	21.3188	20.0478	20.041
θ_5	20	19.8950	21.6989	19.97	19.9993
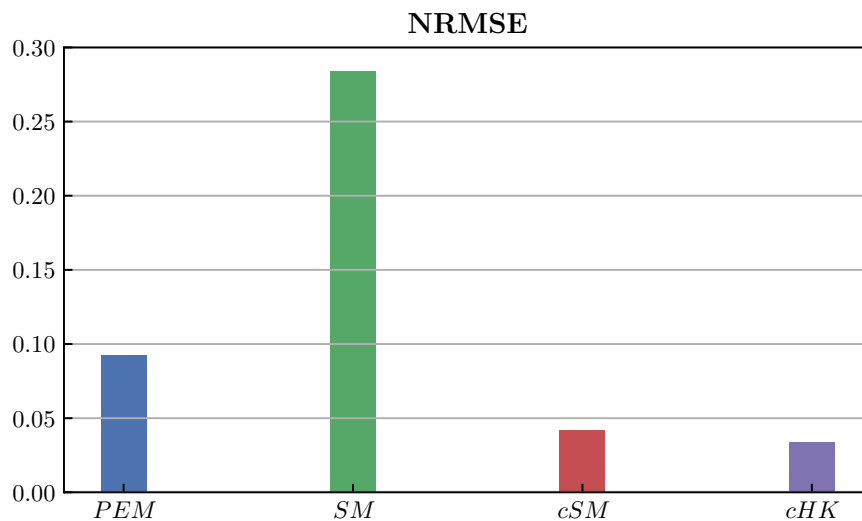
Figure 4.14: PV-mode IBR case: NRMSE.

4.5.3 Computational Analysis

To examine the performance of the techniques, we use off-the-shelf solvers.

- Nonlinear techniques: PEM and SM

Even with the recent advances in approaching nonlinear problems, the solution most likely diverges or settles in a local point that does not reflect the actual system parameters. Both PEM and SM are nonlinear with different structures. While nonlinear solvers are based on nonlinear algorithms, each algorithm is compatible with certain nonlinear structures. The
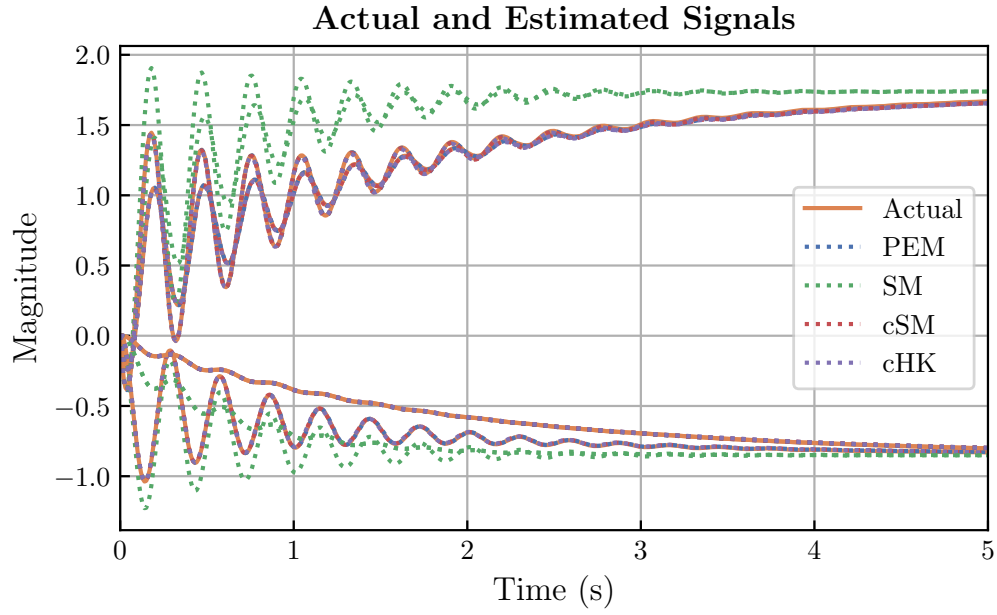
Figure 4.15: PV-mode IBR case: comparing the identified signals with the original.
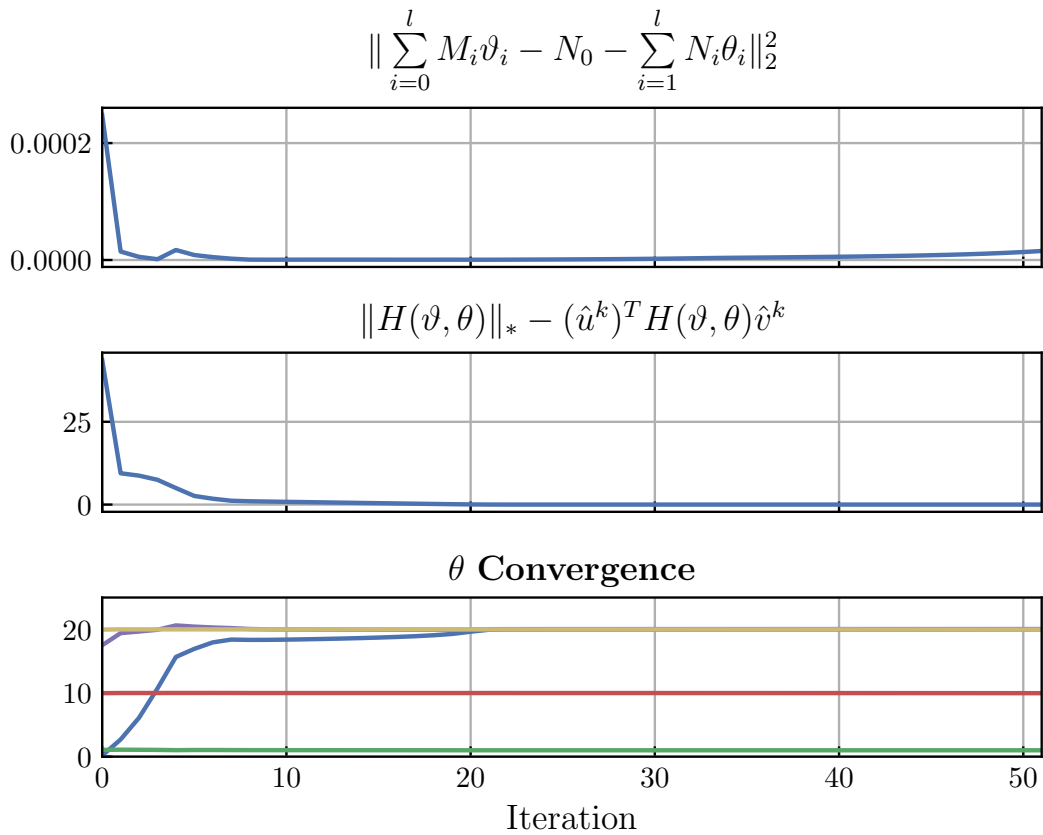
Figure 4.16: PV-mode IBR case: cSM iteration solution.
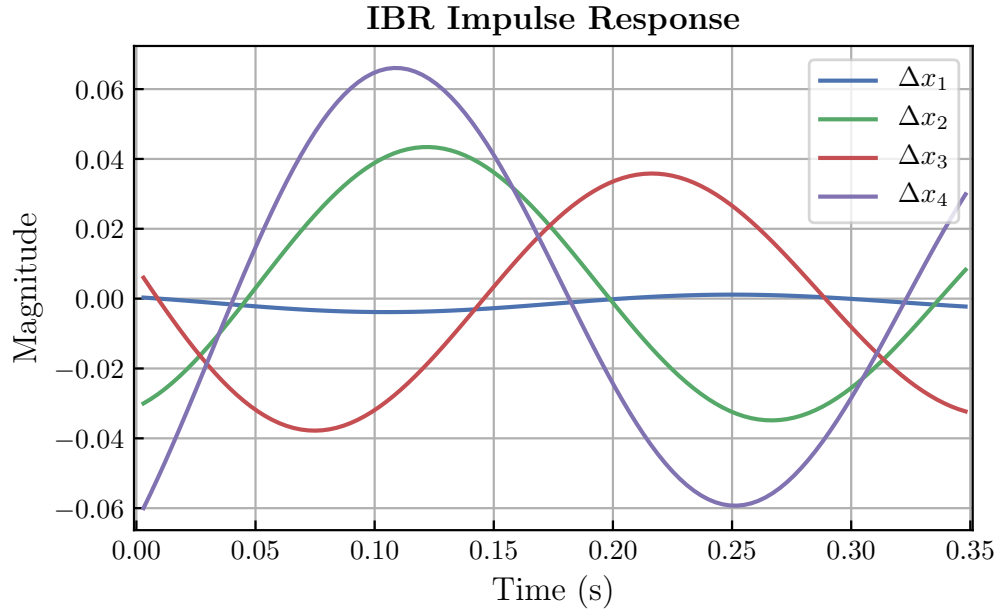
Figure 4.17: PV-mode IBR case: impulse response.
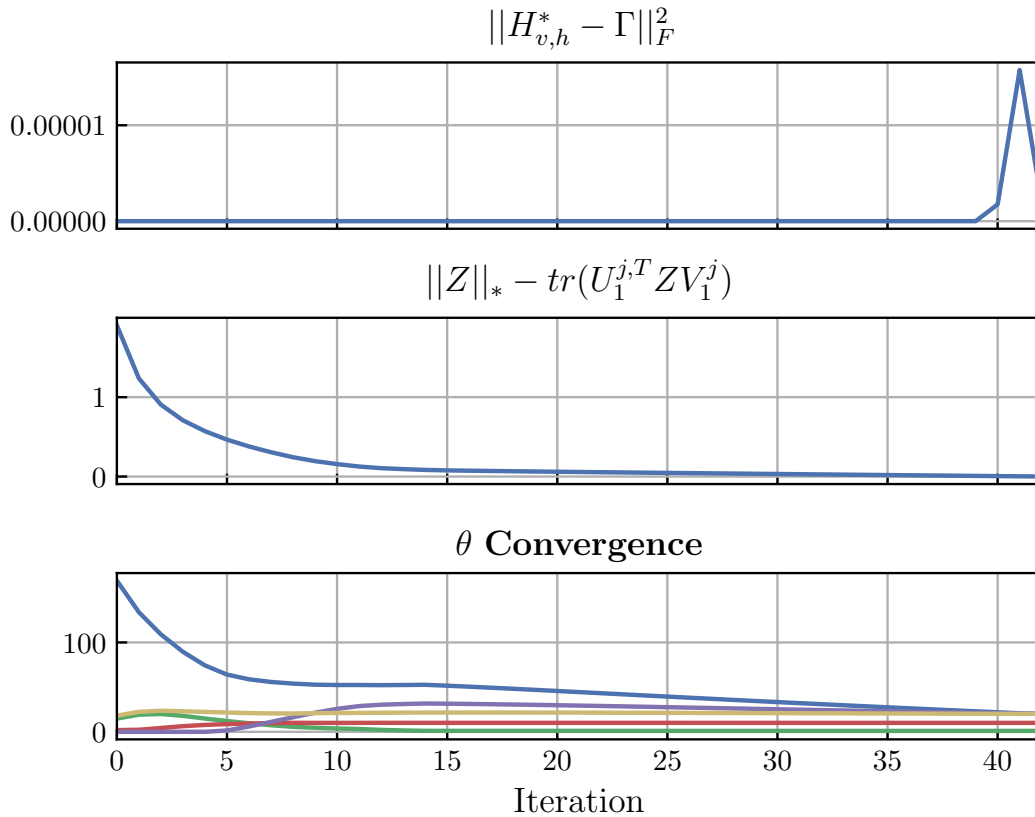
Figure 4.18: PV-mode IBR case: cHK iteration solution.

default algorithm for fmincon is the interior-point and for IPOPT is the primal-dual interior point.

For PEM, IPOPT is way more efficient and accurate than fmincon. In fact, as shown in the IBR case study, the NRMSE of the fmincon is high that reconstructing the system signal does not match the original. As a result, the user is exposed to be misguided. For SM, on the other hand, fmincon can reach a solution with an error while IPOPT cannot. The fmincon solution is highly sensitive to initialization.

- Convex techniques: cSM and cHK

In the SMIB case study, the parameter identification error of cSM is insignificant that the identified system can accurately reconstruct the signals of the actual parameters. Another criterion to evaluate the identification is the NRMSE, which is below 0.01 for this method. With a larger system, as in IBR case study, cSM has small NRMSE and excellent signal reconstruction.

cHK exactly identifies the parameters of the SMIB case study, and it has the lowest NRMSE in identifying the IBR case. For this method, the error can be further reduced by including more impulse data; however, it dramatically adds a severely computational burden. While the accuracy of cHK outperforms the other methods, it is computationally expensive, especially with many parameters.

Chapter 5: Conclusion and Future Work

This chapter concludes the contributions of this dissertation and plans future work.

5.1   Conclusion

Chapter 2 delves into the dynamic mode decomposition algorithm and considers it in power system applications. Besides its high accuracy in identifying a model, DMD has the capability to decompose spatial and temporal modes. The first case study presents the DMD ability to identify the RLC circuit modes from a few measurement samples. DMD is found to be as accurate as ERA. Then, we add noise to the RLC measurements to examine both methods, and it is noticed that the DMD's eigenvalues remain unchanged as in the base case. The second case study applies DMD on PMU power measurement data of an unknown system. The solution is found comparable to the ERA method. The third case study conducts DMD on a data-set of voltage measurement that is distorted due to disturbance; DMD is capable of identifying all the measurement component details. This case shows that the DMD can recognize the dominance of each mode; this is the FFT's feature.

Chapter 3 considers DMD in real-world oscillation event analysis to identify the oscillation modes and distinct their nature. We improve the DMD algorithm for modal analysis of power grids in two aspects: enhanced accuracy and reduced computing cost. Enhanced accuracy is achieved by the use of the data shift-stacking technique, which results in a data matrix with a much larger size. To reduce computing cost, a randomized linear algebra technique creates a new data matrix with much less row dimension while having data information preserved. The resulting randomized DMD is implemented on oscillation analysis. Three real-world

oscillation event data have been used for case studies to demonstrate the excellent modal identification capability of randomized DMD.

Chapter 4 explores the gray-box model identification, which is a challenging task since the formulated optimization problems are nonlinear programming problems. Advancements have been made in this area by exploiting the low-rank characteristics of the data and adopting difference of convex programming. Our research implements the most recent research results of gray-box model identification in synchronous generator parameter identification and IBR parameter identification. Two case studies are used to demonstrate the problem formulation and solving for parameter identification. The results show that the convexified techniques outperform the classical nonlinear methods. Also, with the presented new techniques, the user can bypass problem initialization that could lead to incorrect parameters.

5.2 Future Work

In our work, we provide an efficient way to distinct the oscillation type whether it is local or inter-area. This fastens tracking the disturbance location. The inter-area oscillation is more harmful as it spreads in the whole network, as in the case of the 1996 event. The main causes of inter-area oscillations: low-inertia, generator clustering, and high inter-area power transfer. I plan to investigate detailed cases and try to mitigate the inter-area oscillation spread in the network. This step completely relies on control theory. In the literature, inter-area oscillations have been suppressed by different devices such as power system stabilizers, FACTS, and other controllers. Reference [55] goes further to damping the inter-area oscillations with a doubly-fed induction generator wind farm turbine.

As my focus is on data-driven implementations, certain steps must be considered before applying the above-mentioned strategies. First, we must investigate the available data. This is a critical step to handle real-world applications. As we have seen in Chapter 3, it is possible to characterize the oscillation type from the data and recognize whether it is local or inter-area by examining the direction of the identified system eigenvectors. This can be achieved

by taking the PMU phase angle measurements. PMU voltage measurements are available, however, they do not lead to the same conclusion. In my future study, I will analyze more of the available data to understand the physical relations that highly help control inter-area oscillations.

Second, I will inspect the controllability of the system. In general, the majority of the power system is controlled by closed-loop feedback, the system input actuation is based on the output observation. The physical relationship of the power system applications is coupled, so it should be sought after determining the optimal actuators that have higher control authority with the least cost. In the analysis of Chapter 3, we consider PMUs of generation and transmission substations in general; in future work, detailed analysis should be considered that breaks down the components of each substation to evaluate the most controllable substations or devices.

To do so, parameter identification methods help a lot in estimating the unknown components of the system. As it is part of this dissertation, Chapter 4 presents four identification methods identifying synchronous generators and inverter-based resources. In future work, these methods are going to be used to identify substation components to find the optimal actuator to control the system.

References

[1] Wind explained: where wind power is harnessed. https://www.eia.gov/ energyexplained/wind/where-wind-power-is-harnessed.php. Accessed: 2020-10-19.

[2] NERC. Interconnection oscillation analysis reliability assessment , july 2019. https://www.nerc.com/comm/PC/SMSResourcesDocuments/Interconnection‗ Oscillation‗Analysis.pdf,

[3] Dmitry N Kosterev, Carson W Taylor, and William A Mittelstadt. Model validation for the august 10, 1996 wscc system outage. *IEEE transactions on power systems*, 14(3):967–979, 1999.

[4] Lingling Fan. Data fusion-based distributed prony analysis. *Electric Power Systems Research*, 143:634–642, 2017.

[5] John F Hauer, CJ Demeure, and LL Scharf. Initial results in prony analysis of power system response signals. *IEEE Transactions on power systems*, 5(1):80–89, 1990.

[6] Yingbo Hua and Tapan K Sarkar. Matrix pencil method for estimating parameters of exponentially damped/undamped sinusoids in noise. *IEEE Transactions on Acoustics, Speech, and Signal Processing*, 38(5):814–824, 1990.

[7] Lisa L Grant and Mariesa L Crow. Comparison of matrix pencil and prony methods for power system modal analysis of noisy signals. In *2011 North American Power Symposium*, pages 1–7. IEEE, 2011.

[8] JJ Sanchez-Gasca. Computation of turbine-generator subsynchronous torsional modes from measured data using the eigensystem realization algorithm. In *2001 IEEE Power Engineering Society Winter Meeting. Conference Proceedings (Cat. No. 01CH37194)*, volume 3, pages 1272–1276. IEEE, 2001.

[9] Yoshihiko Susuki and Igor Mezić. Nonlinear koopman modes and power system stability assessment without models. *IEEE Transactions on Power Systems*, 29(2):899–907, 2013.

[10] Alexander R Borden and Bernard C Lesieutre. Variable projection method for power system modal identification. *IEEE Transactions on Power Systems*, 29(6):2613–2620, 2014.

[11] M Crow, M Gibbard, A Messina, J Pierre, J Sanchez-Gasca, D Trudnowski, and D Vowles. Identification of electromechanical modes in power systems. *IEEE Task Force Report, Special Publication TP462*, 2012.

[12] Anas Almunif, Lingling Fan, and Zhixin Miao. A tutorial on data-driven eigenvalue identification: Prony analysis, matrix pencil, and eigensystem realization algorithm. *International Transactions on Electrical Energy Systems*, 30(4):e12283, 2020.

[13] Slava Maslennikov, Bin Wang, Qiang Zhang, Eugene Litvinov, et al. A test cases library for methods locating the sources of sustained oscillations. In *2016 IEEE Power and Energy Society General Meeting (PESGM)*, pages 1–5. IEEE, 2016.

[14] Peter J Schmid. Dynamic mode decomposition of numerical and experimental data. *Journal of fluid mechanics*, 656:5–28, 2010.

[15] J Nathan Kutz, Steven L Brunton, Bingni W Brunton, and Joshua L Proctor. *Dynamic mode decomposition: data-driven modeling of complex systems*. SIAM, 2016.

[16] Jonathan H Tu, Clarence W Rowley, Dirk M Luchtenburg, Steven L Brunton, and J Nathan Kutz. On dynamic mode decomposition: theory and applications. *arXiv preprint arXiv:1312.0041*, 2013.

[17] Emilio Barocio, Bikash C Pal, Nina F Thornhill, and Arturo Roman Messina. A dynamic mode decomposition framework for global power system oscillation analysis. *IEEE Transactions on Power Systems*, 30(6):2902–2912, 2015.

[18] Saurav Mohapatra and Thomas J Overbye. Fast modal identification, monitoring, and visualization for large-scale power systems using dynamic mode decomposition. In *2016 Power Systems Computation Conference (PSCC)*, pages 1–7. IEEE, 2016.

[19] J Jorge Ramos and J Nathan Kutz. Dynamic mode decomposition and sparse measurements for characterization and monitoring of power system disturbances. *arXiv preprint arXiv:1906.03544*, 2019.

[20] AE Saldaña, E Barocio, AR Messina, JJ Ramos, R Juan Segundo, and GA Tinajero. Monitoring harmonic distortion in microgrids using dynamic mode decomposition. In *2017 IEEE Power & Energy Society General Meeting*, pages 1–5. IEEE, 2017.

[21] Pranav Sharma, Bowen Huang, Venkatramana Ajjarapu, and Umesh Vaidya. Data-driven identification and prediction of power system dynamics using linear operators. In *2019 IEEE Power & Energy Society General Meeting (PESGM)*, pages 1–5. IEEE, 2019.

[22] A. Alassaf and L. Fan. Dynamic mode decomposition in various power system applications. In *2019 North American Power Symposium (NAPS)*, pages 1–6, 2019.

[23] Lingling Fan. *Control and dynamics in power systems and microgrids*. CRC Press, 2017.

[24] Peter W Sauer, Mangalore A Pai, and Joe H Chow. *Power system dynamics and stability: with synchrophasor measurement and power system toolbox.* John Wiley & Sons, 2017.

[25] Amirnaser Yazdani and Reza Iravani. *Voltage-sourced converters in power systems*, volume 34. Wiley Online Library, 2010.

[26] N Benjamin Erichson, Lionel Mathelin, J Nathan Kutz, and Steven L Brunton. Randomized dynamic mode decomposition. *SIAM Journal on Applied Dynamical Systems*, 18(4):1867–1891, 2019.

[27] Abdullah Alassaf and Lingling Fan. Randomized dynamic mode decomposition for oscillation modal analysis. *IEEE Transactions on Power Systems*, 36(2):1399–1408, 2020.

[28] Nathan Halko, Per-Gunnar Martinsson, and Joel A Tropp. Finding structure with randomness: Probabilistic algorithms for constructing approximate matrix decompositions. *SIAM review*, 53(2):217–288, 2011.

[29] Graham Rogers. *Power system oscillations.* Springer Science & Business Media, 2012.

[30] Joe H Chow and Kwok W Cheung. A toolbox for power system dynamics and control engineering education and research. *IEEE transactions on Power Systems*, 7(4):1559–1564, 1992.

[31] Test cases library of power system sustained oscillations. http://web.eecs.utk.edu/~kaisun/Oscillation/actualcases.html, note = July 2019.

[32] P Pourbeik, A Ellis, J Sanchez-Gasca, Y Kazachkov, E Muljadi, J Senthil, and D Davies. Generic stability models for type 3 & 4 wind turbine generators for wecc. In *2013 IEEE Power & Energy Society General Meeting*, pages 1–5. IEEE, 2013.

[33] P Pourbeik, JJ Sánchez-Gasca, J Senthil, J Weber, A Ellis, S Williams, S Seman, K Bolton, N Miller, RJ Nelson, et al. Value and limitations of the positive sequence generic models of renewable energy systems. *This is a brief white-paper prepared by an Ad hoc group within the WECC Renewable Energy Modeling Task Force*, 2015.

[34] Valery Knyazkin, Claudio A Canizares, and Lennart H Soder. On the parameter estimation and modeling of aggregate power system loads. *IEEE Transactions on Power Systems*, 19(2):1023–1031, 2004.

[35] Mehdi Karrari and OP Malik. Identification of physical parameters of a synchronous generator from online measurements. *IEEE transactions on energy conversion*, 19(2):407–415, 2004.

[36] H Bora Karayaka, Ali Keyhani, Gerald Thomas Heydt, Baj L Agrawal, and Douglas A Selin. Synchronous generator model identification and parameter estimation from operating data. *IEEE transactions on energy conversion*, 18(1):121–126, 2003.

[37] Song Guo, Sean Norris, and Janusz Bialek. Adaptive parameter estimation of power system dynamic model using modal information. *IEEE Transactions on Power Systems*, 29(6):2854–2861, 2014.

[38] Andrey Gorbunov, Anatoly Dymarsky, and Janusz Bialek. Estimation of parameters of a dynamic generator model from modal pmu measurements. *IEEE Transactions on Power Systems*, 35(1):53–62, 2019.

[39] MA Mohd Ariff, BC Pal, and Abhinav Kumar Singh. Estimating dynamic model parameters for adaptive protection and control in power system. *IEEE Transactions on Power Systems*, 30(2):829–839, 2014.

[40] Zhengyu Wang, Lingling Fan, and Zhixin Miao. Data-driven dynamic model identification for synchronous generators. In *2019 North American Power Symposium (NAPS)*, pages 1–6. IEEE, 2019.

[41] Lennart Ljung. System identification. *Wiley encyclopedia of electrical and electronics engineering*, pages 1–19, 1999.

[42] Guillaume Mercère, Olivier Prot, and José A Ramos. Identification of parameterized gray-box state-space systems: From a black-box linear time-invariant representation to a structured one. *IEEE Transactions on Automatic Control*, 59(11):2873–2885, 2014.

[43] Chengpu Yu, Michel Verhaegen, Shahar Kovalsky, and Ronen Basri. Identification of structured lti mimo state-space models. In *2015 54th IEEE Conference on Decision and Control (CDC)*, pages 2737–2742. IEEE, 2015.

[44] Chengpu Yu, Lennart Ljung, and Michel Verhaegen. Identification of structured state-space models. *Automatica*, 90:54–61, 2018.

[45] BL Ho and Rudolf E Kálmán. Effective construction of linear state-variable models from input/output functions. *at-Automatisierungstechnik*, 14(1-12):545–548, 1966.

[46] Pablo A Parrilo and Lennart Ljung. Initialization of physical parameter estimates. *IFAC Proceedings Volumes*, 36(16):1483–1488, 2003.

[47] Michel Verhaegen and Vincent Verdult. *Filtering and system identification: a least squares approach*. Cambridge university press, 2007.

[48] J. Löfberg. Yalmip : A toolbox for modeling and optimization in matlab. In *In Proceedings of the CACSD Conference*, Taipei, Taiwan, 2004.

[49] Andreas Wächter and Lorenz T Biegler. On the implementation of an interior-point filter line-search algorithm for large-scale nonlinear programming. *Mathematical programming*, 106(1):25–57, 2006.

[50] Michael Grant and Stephen Boyd. CVX: Matlab software for disciplined convex programming, version 2.1. http://cvxr.com/cvx, March 2014.

[51] Joe H Chow and Juan J Sanchez-Gasca. *Power System Modeling, Computation, and Control.* John Wiley & Sons, 2020.

[52] Lingling Fan and Zhixin Miao. An explanation of oscillations due to wind power plants weak grid interconnection. *IEEE Transactions on Sustainable Energy*, 9(1):488–490, 2017.

[53] Shun-Hsien Huang, John Schmall, Jose Conto, John Adams, Yang Zhang, and Cathey Carter. Voltage control challenges on weak grids with high penetration of wind generation: Ercot experience. In *2012 IEEE Power and Energy Society General Meeting*, pages 1–7. IEEE, 2012.

[54] Pablo A Parrilo and Lennart Ljung. Initialization of physical parameter estimates. *IFAC Proceedings Volumes*, 36(16):1483–1488, 2003.

[55] Lingling Fan, Haiping Yin, and Zhixin Miao. On active/reactive power modulation of dfig-based wind generation for interarea oscillation damping. *IEEE Transactions on Energy Conversion*, 26(2):513–521, 2010.

Appendix A: Reuse Permissions of Published Papers

The permission below is for the reproduction of material in Chapter 2.

CCC
RightsLink®

Home | Help ⌄ | Email Support | Sign in | Create Account

Dynamic Mode Decomposition in Various Power System Applications

Conference Proceedings: 2019 North American Power Symposium (NAPS)

Author: Abdullah Alassaf

Publisher: IEEE

Date: Oct. 2019

Copyright © 2019, IEEE

IEEE
Requesting permission to reuse content from an IEEE publication

---

Thesis / Dissertation Reuse

The IEEE does not require individuals working on a thesis to obtain a formal reuse license, however, you may print out this statement to be used as a permission grant:

Requirements to be followed when using any portion (e.g., figure, graph, table, or textual material) of an IEEE copyrighted paper in a thesis:

1) In the case of textual material (e.g., using short quotes or referring to the work within these papers) users must give full credit to the original source (author, paper, publication) followed by the IEEE copyright line © 2011 IEEE.
2) In the case of illustrations or tabular material, we require that the copyright line © [Year of original publication] IEEE appear prominently with each reprinted figure and/or table.
3) If a substantial portion of the original paper is to be used, and if you are not the senior author, also obtain the senior author's approval.

Requirements to be followed when using an entire IEEE copyrighted paper in a thesis:

1) The following IEEE copyright/ credit notice should be placed prominently in the references: © [year of original publication] IEEE. Reprinted, with permission, from [author names, paper title, IEEE publication title, and month/year of publication]
2) Only the accepted version of an IEEE copyrighted paper can be used when posting the paper or your thesis on-line.
3) In placing the thesis on the author's university website, please display the following message in a prominent place on the website: In reference to IEEE copyrighted material which is used with permission in this thesis, the IEEE does not endorse any of [university/educational entity's name goes here]'s products or services. Internal or personal use of this material is permitted. If interested in reprinting/republishing IEEE copyrighted material for advertising or promotional purposes or for creating new collective works for resale or redistribution, please go to http://www.ieee.org/publications_standards/publications/rights/rights_link.html to learn how to obtain a License from RightsLink.

If applicable, University Microfilms and/or ProQuest Library, or the Archives of Canada may supply single copies of the dissertation.

BACK   CLOSE WINDOW

The permission below is for the reproduction of material in Chapter 3.

CCC
RightsLink®

Home   Help ∨   Email Support   Sign in   Create Account

Randomized Dynamic Mode Decomposition for Oscillation Modal Analysis

Author: Abdullah Alassaf

Publication: IEEE Transactions on Power Systems

Publisher: IEEE

Date: March 2021

Copyright © 2021, IEEE

About the Author

Abdullah Alassaf was born in September 05, 1990. He received BSc from the University of Hail, Hail, Saudi Arabia in 2013. In 2017, he received MSc from the University of South Florida, Tampa, USA. where he is currently working towards his PhD since 2017. Abdullah worked as a teaching assistant University of Hail.